Hf-W chronology of CR chondrites: Implications for the timescales of chondrule formation and the distribution of ^{26}Al in the solar nebula

Gerrit Budde[a,*], Thomas S. Kruijer[a,b], Thorsten Kleine[a]

[a]Institut für Planetologie, University of Münster, Wilhelm-Klemm-Straße 10, 48149 Münster, Germany

[b]Nuclear and Chemical Sciences Division, Lawrence Livermore National Laboratory, Livermore, CA 94550, USA

*corresponding author: gerrit.budde@uni-muenster.de

Keywords: Hf-W chronometry; chondrules; Mo isotopes; ^{26}Al; Renazzo; accretion; complementarity

accepted for publication in
Geochimica et Cosmochimica Acta
https://doi.org/10.1016/j.gca.2017.10.014

Abstract

Renazzo-type carbonaceous (CR) chondrites are distinct from most other chondrites in having younger chondrule ^{26}Al-^{26}Mg ages, but the significance of these ages and whether they reflect true formation times or spatial variations of the ^{26}Al/^{27}Al ratio within the solar protoplanetary disk are a matter of debate. To address these issues and to determine the timescales of metal-silicate fractionation and chondrule formation in CR chondrites, we applied the short-lived ^{182}Hf-^{182}W chronometer to metal, silicate, and chondrule separates from four CR chondrites. We also obtained Mo isotope data for the same samples to assess potential genetic links among the components of CR chondrites, and between these components and bulk chondrites.

All investigated samples plot on a single Hf-W isochron and constrain the time of metal-silicate fractionation in CR chondrites to 3.6±0.6 million years (Ma) after the formation of Ca-Al-rich inclusions (CAIs). This age is indistinguishable from a ~3.7 Ma Al-Mg age for CR chondrules, suggesting not only that metal-silicate fractionation and chondrule formation were coeval, but also that these two processes were linked to each other. The good agreement of the Hf-W and Al-Mg ages, combined with concordant Hf-W and Al-Mg ages for angrites and CV chondrules, provides strong evidence for a disk-wide, homogeneous distribution of ^{26}Al in the early solar system. As such, the young Al-Mg ages for CR chondrules do not reflect spatial ^{26}Al/^{27}Al heterogeneities but indicate that CR chondrules formed ~1–2 Ma later than chondrules from most other chondrite groups.

Metal and silicate in CR chondrites exhibit distinct nucleosynthetic Mo and W isotope anomalies, which are caused by the heterogeneous distribution of the same presolar *s*-process carrier. These data suggest that the major components of CR chondrites are genetically linked and therefore formed from a single reservoir of nebular dust, most likely by localized melting events within the solar protoplanetary disk. Taken together, the chemical, isotopic, and chronological data for components of CR chondrites imply a close temporal link between chondrule formation and chondrite accretion, indicating that the CR chondrite parent body is one of the youngest meteorite parent bodies. The relatively late accretion of the CR parent body is consistent with its isotopic composition (for instance the elevated ^{15}N/^{14}N) that suggests a formation at a larger heliocentric distance, probably beyond the orbit of Jupiter. As such, the accretion age of the CR chondrite parent body of ~3.6 Ma after CAI formation provides the earliest possible time at which Jupiter's growth could have led to scattering of carbonaceous meteorite parent bodies from beyond its orbit into the inner solar system.

1. Introduction

The formation of chondrules, millimeter-sized igneous spherules that dominate most chondrites, might have been a critical step towards the accumulation of dust into planetesimals (e.g., Alexander et al., 2008). Consequently, understanding the origin of chondrules and constraining the timescales of their formation can provide important insights into the processes affecting solid material in the solar nebula, ultimately leading to the formation of planetesimals and larger planets. Of the different classes of chondrites, Renazzo-type carbonaceous (CR) chondrites are particularly important, because available Pb-Pb and Al-Mg data imply that CR chondrules are ~1–2 million years (Ma) younger than chondrules from most other chondrite groups (e.g., Amelin et al., 2002; Schrader et al., 2017). Assuming that chondrule formation closely approximates the time of chondrite parent body accretion (e.g., Alexander et al., 2008; Budde et al., 2016b), this would make the CR chondrite parent body one of the youngest meteorite parent bodies and, as such, its accretion age would provide a lower limit for the time over which primitive planetesimals formed in the early solar system. However, the chronological data for CR chondrites are restricted to Pb-Pb and Al-Mg ages obtained for a small number of chondrules, and the relevance of these ages remains debated. For instance, the Al-Mg data might have no chronological significance if ^{26}Al was heterogeneously distributed in the early solar system, meaning that the low initial ^{26}Al/^{27}Al of CR chondrules may reflect formation in a ^{26}Al-poor region of the disk rather than a late formation (Olsen et al., 2016; Van Kooten et al., 2016). Thus, independent age constraints are needed to firmly establish the formation time of CR chondrules.

Such age constraints can be obtained from the short-lived ^{182}Hf-^{182}W chronometer ($t_{1/2}$ ≈ 8.9 Ma). Compared to the Al-Mg and Pb-Pb systems, this system is far more robust against disturbance by parent body processes (e.g., Kleine et al., 2008), and, unlike for ^{26}Al, it is well established that ^{182}Hf was homogeneously distributed throughout the solar protoplanetary disk (e.g., Burkhardt et al., 2008; Kleine et al., 2009; Burkhardt et al., 2012a; Kruijer et al., 2014a). Instead of dating the crystallization of individual chondrules, the Hf-W system provides the timing of large-scale Hf-W fractionation among chondrite components, which itself is controlled by metal-silicate separation (e.g., Budde et al., 2016b). As CR chondrites are characterized by abundant Fe-Ni metal (5–8 vol.%; Weisberg et al., 1993), this event can readily be dated through Hf-W isochrons defined by distinct metal and silicate fractions. In case of primitive meteorites such as CR chondrites, such internal Hf-W isochrons are expected to provide the age of chondrules, since chondrule formation was accompanied by metal-silicate separation and thus significant Hf-W fractionation (e.g., Palme et al., 2014).

In addition to radiogenic variations from ^{182}Hf decay, W isotope anomalies can also be of nucleosynthetic origin, caused by the heterogeneous distribution of isotopically anomalous presolar matter derived from diverse nucleosynthetic sources (e.g., Burkhardt and Schönbächler, 2015). Such nucleosynthetic W isotope variations have been identified in different components of carbonaceous chondrites, including chondrules and matrix from the CV3 chondrite Allende (Budde et al., 2016b). As demonstrated for these chondrule and matrix samples, nucleosynthetic W isotope anomalies are useful tracers of genetic links among chondrite components, especially when combined with the measurements of nucleosynthetic Mo isotope anomalies (Burkhardt et al., 2012b; Budde et al., 2016a). For instance, on the basis of Mo isotope data for Allende chondrules and matrix, Budde et al. (2016a) showed that these samples contain a ubiquitous enrichment in *r*-process material. This same enrichment is seen for other bulk carbonaceous chondrites, as well as for some iron meteorites. On this basis, Budde et al. (2016a) distinguished between carbonaceous and non-carbonaceous meteorites and argued that two genetically distinct reservoirs co-existed in the solar protoplanetary disk. As such, CR chondrites play a key role in determining for how long these reservoirs co-existed, provided that CR chondrites formed as late as suggested by their Al-Mg chondrule ages and that their components are genetically linked to the carbonaceous group of meteorites.

To address these issues and to determine the timescales of metal-silicate fractionation and chondrule formation in CR chondrites, we obtained high-precision Hf-W isotope data for bulk samples, magnetic separates, and individual components (metal, chondrules) from four CR chondrites. For some of these samples, we also obtained Mo isotope data, to establish genetic links among the different components of CR chondrites, and between these components and the carbonaceous group of meteorites. In addition to providing constraints on the origin and age of chondrules and metal in CR chondrites, the Hf-W data have important implications for assessing the distribution of ^{26}Al in the solar protoplanetary disk and, hence, the chronological significance of Al-Mg data. Moreover, the combined W and Mo isotope data also have some broader implications for understanding the early evolution of the solar system, including the formation of Jupiter.

2. Samples and analytical methods

2.1. Sample preparation

The CR chondrites investigated in the present study include three finds from hot deserts (NWA 801, Acfer 097, NWA 1180) and one from Antarctica (GRA 06100). Of

these, Acfer 097 is paired with eight other Acfer meteorites (e.g., Acfer 059) as well as El Djouf 001 (Bischoff et al., 1993). NWA 801 is characterized by moderate to extensive weathering, whereas the other samples show only moderate weathering (weathering grade W2). Although all investigated CR chondrites are of petrologic type 2, the degree of aqueous alteration varies significantly among the samples. Based on their oxygen isotope compositions and petrographic properties (Schrader et al., 2011; Harju et al., 2014), NWA 801 and Acfer 097 are only weakly altered (subtype 2.8), while GRA 06100 (subtype 2.5) has been affected by significant aqueous alteration (there is no data available for NWA 1180). In contrast to most CR chondrites, GRA 06100 has also undergone substantial thermal metamorphism, most likely as a consequence of shock-heating during an impact event (see supplementary material for details).

Pieces of the CR2 chondrites (~6–9 g for each sample) were carefully cleaned by polishing with SiC and sonication in acetone. Each sample was then gradually crushed in an agate mortar and sieved using polyamide meshes. During this grinding process, chondrules (i.e., chondrule fragments and intact chondrules) as well as metal grains (>125 μm) were removed by hand-picking. The remaining material was ground to 40–125 μm, cleaned from adhering dust by washing with a mixture of ultrapure water and ethanol, and separated into several fractions according to their magnetic susceptibility using hand-magnets. They were labeled 'MS-*n*' (*n* = 1, 2, 3, 4, 5), where MS-1 denotes the most-magnetic and MS-5 the least/non-magnetic fraction for each chondrite. These magnetic separates consist of variable proportions of metal as well as chondrule and matrix material, and are thus also referred to as 'mixed fractions'.

The metal separates (denoted 'M') were cleaned by sonication in ethanol and grinding in an agate mortar under ethanol, followed by additional hand-picking and use of hand-magnets. This resulted in efficient removal of any silicate material attached to or intergrown with the metals. For NWA 801 sufficient metal was obtained to further separate it into fine (125–500 μm) and coarse (>500 μm) fractions. Also, metal from GRA 06100 was further divided into three different grain-size fractions (125–500 μm, 500–1000 μm, >1000 μm). Note that the relative amount (by mass) of metal (>125 μm) extracted from each meteorite is variable and increases in the order GRA 06100 (2.1%) < NWA 1180 (4.2%) < Acfer 097 (4.8%) < NWA 801 (6.3%); as such, the metal content seems to be inversely correlated with the degree of aqueous alteration of each sample.

The chondrule separates (~0.7 g per meteorite), each consisting of several hundred chondrule fragments and intact chondrules in the size range of 500–1600 μm, were carefully purified by hand-picking under a stereo microscope and, after sonication in acetone, ground to a fine powder in an agate mortar. During this process all visible

metal grains were separated by hand-picking and using hand-magnets. About 30–80 mg of this chondrule metal (denoted 'C-M') was obtained for each CR chondrite, which was further purified in a similar manner as the other metal fractions (see above). The remaining material was further separated using hand-magnets and only the least/non-magnetic material (0.4–0.5 g) was analyzed, representing the silicate-dominated portion of the chondrules (denoted 'C-S').

2.2. Chemical separation and isotope measurements

Whole-rock powders and most silicate fractions (0.4–0.5 g) were digested in Savillex® beakers on a hotplate using HF–HNO_3–$HClO_4$ (2:1:0.01) at 180–200 °C (5 days), followed by 'inverse' aqua regia (2:1 HNO_3–HCl) at 130–150 °C (2 days). To minimize potential W contamination from the digestion vials, chondrule separates (C-S) and the least-magnetic (MS-5) fractions were digested at lower temperatures, using HF-HNO_3 (2:1) at 130 °C (3 days) and inverse aqua regia at 110 °C (1 day). Metal separates (0.03–0.3 g; including chondrule metal) were dissolved using inverse aqua regia (+ trace HF) at 110–130 °C (2 days). After digestion, all samples were processed through the same analytical protocol as described in Budde et al. (2016b) and Budde et al. (2016a), which will be briefly summarized below (see supplementary material for details).

After complete dissolution, small aliquots were taken to determine Hf and W concentrations by isotope dilution (ID). The separation of W from the unspiked aliquot for isotope composition analyses (IC) was performed using a two-stage anion exchange chromatography, where the yield was typically ~70% and the total procedural blanks were negligible for all samples. The W isotope measurements were performed on the Thermo Scientific® Neptune *Plus* MC-ICP-MS in the Institut für Planetologie at the University of Münster. Instrumental mass bias was corrected by internal normalization to $^{186}W/^{184}W$ = 0.92767 (denoted '6/4') or $^{186}W/^{183}W$ = 1.98590 (denoted '6/3') using the exponential law. The W isotope data are reported as *ε*-unit deviations (i.e., 0.01%) relative to the bracketing Alfa Aesar® solution standards. For samples analyzed several times, the reported values represent the mean of pooled solution replicates. The accuracy and precision of the W isotope measurements were assessed by repeated analyses of terrestrial rock (BHVO-2) and metal (NIST 129c) standards (Tables S1 and S2), which define an external reproducibility (2 s.d.) of ~0.1 ε-units for all W isotope ratios. Note that normalizations involving ^{183}W show a small mass-independent effect (on the order of ~0.1ε), which has also been observed in several previous studies (e.g., Willbold et al., 2011; Kruijer et al., 2012). This artifact on W isotope ratios involving ^{183}W is consistent with the nuclear field shift effect (Cook and

Schönbächler, 2016) and was most likely induced during incomplete dissolution of chemically purified W in Savillex® beakers. For all samples, W isotope ratios involving ^{183}W were therefore corrected using the mean ε^{i}W values obtained for the terrestrial standards analyzed in the present study, using the method described in Kruijer et al. (2014a). The associated uncertainties induced through this correction were propagated into the uncertainties reported in Table 1 (see supplementary material for details).

Molybdenum was separated from column washes collected during the anion exchange chemistry used for the separation of W. After the combination of these washes, small aliquots were taken to determine Mo concentrations using a Thermo Scientific® XSeries 2 quadrupole ICP-MS in Münster. The purification of Mo for isotope composition analyses was performed using a two-stage ion exchange chromatography, where the yield was typically ~75% and the total procedural blanks were negligible for all samples. The Mo isotope measurements were also performed on the Thermo Scientific® Neptune *Plus* MC-ICP-MS in Münster. Isobaric interferences of Zr and Ru on Mo masses were corrected by monitoring ^{91}Zr and ^{99}Ru. Instrumental mass bias was corrected by internal normalization to ^{98}Mo/^{96}Mo = 1.453173 using the exponential law. The Mo isotope data are reported as ε^{i}Mo values relative to the mean of bracketing runs of the Alfa Aesar® solution standard, where $\varepsilon^{i}\mathrm{Mo} = [(^{i}\mathrm{Mo}/^{96}\mathrm{Mo})_{\mathrm{sample}} / (^{i}\mathrm{Mo}/^{96}\mathrm{Mo})_{\mathrm{standard}} - 1] \times 10^{4}$ (i = 92, 94, 95, 97, 100). For samples analyzed several times, reported values represent the mean of pooled solution replicates. The accuracy and precision of the Mo isotope measurements were assessed by repeated analyses of the BHVO-2 and NIST 129c standards (Tables S3 and S4), which define an external reproducibility (2 s.d.) of ~0.2–0.4 ε-units for the different Mo isotope ratios.

3. Results

3.1. Hf-W systematics

The Hf-W concentration and isotope data obtained for the CR chondrite samples are provided in Table 1. All metal fractions, including non-chondrule (M) and chondrule metal (C-M), contain <10 ppb Hf and typically have W concentrations of ~500 ppb, resulting in ^{180}Hf/^{184}W <0.03 and indicating that pure metal separates were obtained. For NWA 801 different metal fractions have significantly different W concentrations of up to 1109 ppb for the chondrule metal, while the coarse and fine (non-chondrule) metal fractions contain 468 and 568 ppb W, respectively. This is consistent with results of a prior study, which reported an inverse correlation of siderophile element concentrations and grain sizes of CR metal (Kong et al., 1999). The analyzed bulk CR chondrite samples contain ~175 ppb Hf and ~150 ppb W, where the average ^{180}Hf/^{184}W

of ~1.4 is within the range typically observed for carbonaceous chondrites (Kleine et al., 2004).

For the magnetic separates (MS-*n*) the Hf and W contents vary with the magnetic susceptibility of the separates (Fig. S1). Compared to bulk CR chondrites, the most-magnetic separates (MS-1) are typically depleted in Hf (~100 ppb) and enriched in W (~260 ppb), whereas the least-magnetic fractions (MS-5) are enriched in Hf (~220 ppb) and depleted in W (~50 ppb). These elemental variations are attributable to the decreasing abundance of W-rich metal and increasing abundance of Hf-rich silicate with decreasing magnetic susceptibility (Section 5.1), leading to variable ^{180}Hf/^{184}W of up to ~6.7 in the least-magnetic fractions. The silicate-dominated fractions of the chondrule separates (C-S) display the highest Hf concentrations (~230 ppb) among all samples, which is consistent with the general observation that chondrules from carbonaceous chondrites are enriched in refractory lithophile elements (e.g., Palme et al., 2014). Nevertheless, for each meteorite the ^{180}Hf/^{184}W of the C-S fractions (~3.0–4.4) are lower than those of the least-magnetic fractions (MS-5), reflecting the higher W concentrations in the C-S fractions (~70 ppb). These elevated W concentrations are most likely attributable to the presence of tiny metal inclusions in the silicates that were not removed during the magnetic separation.

An important feature of the new W isotope data is that the CR chondrite samples exhibit variable ε^{183}W excesses (Fig. 1), which for the metal fractions are smaller than for the bulk samples and magnetic separates. For instance, the bulk CR chondrites have a mean ε^{183}W = 0.38±0.19 (2 s.d., n=3), whereas the metal separates (excluding GRA 06100 metal; see below) are characterized by a uniform ε^{183}W excess of 0.14±0.06 [95% confidence interval (95% CI), n=7]. Most of the magnetic separates as well as the silicate-dominated portions of the chondrule separates (C-S) have ε^{183}W values of ~0.6, which are slightly higher than, albeit not resolved from those of the bulk CR chondrites.

In addition, the investigated CR samples exhibit variable ε^{182}W compositions, as expected for samples having variable Hf/W. However, for each sample the ε^{182}W values are distinct for the ^{186}W/^{183}W- and ^{186}W/^{184}W-normalizations (Fig. S2) and only the ε^{182}W (6/3) are well correlated with ^{180}Hf/^{184}W. Moreover, the difference between the ε^{182}W (6/3) and ε^{182}W (6/4) values scales with the magnitude of the anomaly in ε^{183}W, which is characteristic for samples having nucleosynthetic anomalies (see Section 4.1). The measured ε^{182}W (6/3) range from about –3.3 to +2.6, where all metal fractions have indistinguishable ε^{182}W with an average value of about –3.2. Most separates with higher magnetic susceptibility (MS-1, MS-2) also show sub-chondritic ε^{182}W ranging between about –2.8 and –2.3. The bulk CR chondrites exhibit the typical

value of carbonaceous chondrites (ε^{182}W ≈ –1.9; e.g., Kleine et al., 2004), whereas separates with lower magnetic susceptibility (MS-4, MS-5) as well as the silicate-dominated chondrule fractions (C-S) generally display super-chondritic ε^{182}W with excesses up to ~2.6. Compared to ε^{182}W (6/3), the ε^{182}W (6/4) for each sample are generally (up to ~1.5ε) higher.

Of the CR chondrites investigated in the present study, GRA 06100 stands out by having systematically distinct elemental and isotopic signatures. For instance, the separates with higher magnetic susceptibility have lower, whereas those with lower magnetic susceptibility have higher W concentrations, resulting in a much smaller variability in ^{180}Hf/^{184}W compared to magnetic separates of the other CR chondrites. This probably reflects the higher degree of parent body alteration for GRA 06100, resulting in the progressive oxidation of metal and hampering an efficient separation of high- (silicate) and low-Hf/W (metal) phases using hand-magnets. Moreover, GRA 06100 shows the largest variability in ε^{183}W (Fig. 1). Compared to samples from the other three CR chondrites, most samples from GRA 06100 show elevated ε^{183}W anomalies of up to ~1, whereas one sample (MS-3) is characterized by a small ε^{183}W deficit of about –0.2 (see supplementary material for details).

3.2. Mo isotopes

The Mo concentration and isotope data obtained for the CR chondrite samples are provided in Table 2. Molybdenum concentrations range from ~0.4 ppm for the least-magnetic separates (MS-5) to ~4–5 ppm for most metal fractions, and are well correlated with the W concentrations (Fig. S1). Most samples are characterized by Mo/W ≈ 8.6, which is the Mo/W typically observed for CR chondrites and other carbonaceous chondrites (e.g., Kong et al., 1999).

All investigated samples display well-resolved Mo isotope anomalies, the magnitude of which decrease in the order ε^{92}Mo > ε^{94}Mo > ε^{95}Mo > ε^{100}Mo > ε^{97}Mo (Fig. 2). Moreover, the ε^{i}Mo are broadly correlated with ε^{183}W (Fig. 3), and as for ε^{183}W, the metal fractions (non-chondrule and chondrule metal) show a uniform ε^{92}Mo excess of 1.85±0.14 (95% CI, n=5), which is significantly smaller than the ε^{92}Mo anomaly of ~3.9 observed for bulk CR chondrites. The magnetic separates and the analyzed C-S fraction have variable ε^{92}Mo excesses that typically range from ~2.5 to ~10.6. Overall, the Mo isotope anomalies are broadly correlated with Mo concentrations (Fig. S4), suggesting that the variable isotope signatures in the analyzed samples reflect different proportions of metal with a smaller ε^{92}Mo anomaly compared to CR silicate.

As for the Hf-W systematics, GRA 06100 is distinct from the other CR chondrites, because it shows more variable Mo/W (~4–17; Fig. S1) and a larger range of Mo

isotope anomalies (ε^{92}Mo of about –2.1 to 10.7), including one sample (MS-3) with a negative ε^{92}Mo anomaly that is consistent with its ε^{183}W deficit. These variations most likely result from some Mo and/or W mobilization during parent body processes (see supplementary material for details).

4. Nucleosynthetic isotope heterogeneity in CR chondrites

4.1. Nucleosynthetic W and Mo isotope anomalies

As noted above (Section 3.1), the presence of ε^{183}W variations and the correlation of ε^{183}W with the disparity of ε^{182}W (6/3) and ε^{182}W (6/4) values is characteristic for samples having nucleosynthetic W isotope anomalies, where the observed ε^{183}W excesses are attributable to a deficit in *s*- or an excess in *r*-process W nuclides. Similar systematics have previously been observed for components and acid leachates of primitive chondrites (Burkhardt et al., 2012a; Kruijer et al., 2014a; Budde et al., 2016b). These studies have shown that nucleosynthetic W isotope variations typically result in correlated ε^{182}W and ε^{183}W anomalies. Consequently, assessing whether or not such a correlation is also observed for the CR chondrite data is important for verifying that the observed ε^{183}W variations are nucleosynthetic in origin.

Addressing this issue requires the differentiation of radiogenic and nucleosynthetic contributions to the observed ε^{182}W variations. We, therefore, corrected the measured ε^{182}W for radiogenic contributions from ^{182}Hf decay using the measured ^{180}Hf/^{184}W of each sample and the initial ^{182}Hf/^{180}Hf of CR chondrites. The latter is not known *a priori* but can be approximated using the ^{186}W/^{183}W-normalized ε^{182}W values, because the effects of nucleosynthetic variations on ε^{182}W (6/3) are small. This is because nucleosynthetic W isotope variations predominantly affect ^{184}W, which has a larger contribution from the *s*-process than the other W isotopes (e.g., Burkhardt et al., 2012a). For instance, the ε^{182}W (6/3) versus ε^{184}W (6/3) slope for the heterogeneous distribution of *s*- and *r*-process W nuclides is between +0.12 (Budde et al., 2016b) and –0.12 (Burkhardt and Schönbächler, 2015). Using either of these slopes and the measured ε^{184}W (6/3) values shows that for the CR samples investigated in the present study, nucleosynthetic effects on ε^{182}W (6/3) are <0.08ε and, hence, smaller than the analytical precision of ±0.15 ε-units. Thus, an accurate estimate of the initial ^{182}Hf/^{180}Hf of CR chondrites can already be obtained from the isochron regression of the measured ε^{182}W (6/3) values, which can then be used to calculate ^{182}Hf decay corrected $\varepsilon^{182}W_i$ (6/4) values. The $\varepsilon^{182}W_i$ (6/4) values thus obtained are correlated with ε^{183}W and all samples plot along a line with a slope of 1.38±0.15 (see Fig. S3 for details). This slope is in good agreement with slopes of 1.25±0.06 obtained for Allende

(CV3) chondrules and matrix (Budde et al., 2016b), as well as 1.41±0.05 obtained for CAIs (Kruijer et al., 2014a) and acid leachates from carbonaceous chondrites (Burkhardt et al., 2012a; Burkhardt and Schönbächler, 2015). Thus, the observed variations in $\varepsilon^{182}W_i$ and $\varepsilon^{183}W$ among components of CR chondrites are consistent with the heterogeneous distribution of *s*- or *r*-process W nuclides.

Whereas the W isotope data do not allow distinguishing between the heterogeneous distribution of an *s*- or *r*-process carrier, such a distinction can be made using Mo isotopes (Burkhardt et al., 2011). The investigated CR samples also have positive Mo isotope anomalies and exhibit the characteristic *w*-shaped Mo isotope pattern that is indicative of a deficit in *s*-process Mo nuclides (Dauphas et al., 2002; Burkhardt et al., 2011) (Fig. 2). Moreover, in diagrams of $\varepsilon^{i}Mo$ versus $\varepsilon^{92}Mo$ (Fig. 4), all analyzed samples plot on single, well-defined correlation lines, the slopes of which are consistent with those obtained for mixing lines between terrestrial Mo and a presumed component enriched in *s*-process Mo. Thus, the Mo isotope anomalies in the CR samples predominantly reflect variable deficits in *s*-process Mo nuclides. As the nucleosynthetic Mo and W isotope anomalies in the CR samples are broadly correlated (Fig. 3), these anomalies probably have a common origin and, hence, most likely reflect the heterogeneous distribution of the same presolar *s*-process carrier. Such correlated nucleosynthetic Mo and W isotope anomalies have previously been observed for Murchison (CM2) leachates as well as Allende chondrules and matrix (Burkhardt et al., 2012b; Budde et al., 2016a).

Although the Mo isotope variations among the investigated CR samples predominantly reflect the heterogeneous distribution of an *s*-process carrier, all CR samples also exhibit a small *r*-process excess. This is evident from a diagram of $\varepsilon^{95}Mo$ versus $\varepsilon^{94}Mo$ (Fig. 5), in which the CR chondrite samples plot on a single correlation line with a slope of 0.602±0.014 and a well resolved positive $\varepsilon^{95}Mo$ intercept of 0.22±0.05 (at $\varepsilon^{94}Mo = 0$). Whereas the Mo isotope variations along this correlation line are consistent with the heterogeneous distribution of an *s*-process carrier, the displacement of the correlation line from the origin is not. Such a positive $\varepsilon^{95}Mo$ intercept has previously been observed for a correlation line defined by data for carbonaceous chondrites, including chondrule and matrix separates, acid leachates, as well as bulk meteorites (see Budde et al., 2016a, for details). These samples define a linear correlation with $\varepsilon^{95}Mo = (0.596\pm0.006) \times \varepsilon^{94}Mo + (0.29\pm0.03)$, which was termed 'CC-line' by Budde et al. (2016a) to distinguish it from a subparallel $\varepsilon^{95}Mo$–$\varepsilon^{94}Mo$ correlation line defined by non-carbonaceous (NC) meteorites (i.e., enstatite and ordinary chondrites, most iron meteorites). The difference between the CC- and NC-lines has been attributed to the addition of *r*-process material to the solar nebula region

from which the carbonaceous (CC) meteorites derive. As the CC- and NC-lines are nearly parallel to each other, this *r*-process material must be homogeneously distributed within the CC reservoir (Budde et al., 2016a). It is noteworthy that all the CR components investigated in the present study plot on the CC-line, providing further evidence for the homogeneous distribution of this *r*-process material in the CC reservoir, in spite of the variable deficits in *s*-process matter observed among bulk samples and components of carbonaceous chondrites. We will further discuss the significance of this observation below (Section 7).

4.2. Effect of sample digestion on measured isotope anomalies

CR chondrites contain abundant (up to ~200 ppm) presolar grains (e.g., silicates, oxides, SiC) that occur in the interchondrule matrix and in fine-grained chondrule rims (e.g., Leitner et al., 2016). Since presolar grains can be extremely acid-resistant, incomplete digestion of such grains can lead to measured isotopic compositions that mirror that of the incompletely dissolved presolar component (Brandon et al., 2005; Yokoyama et al., 2007). For example, presolar SiC grains are strongly enriched in *s*-process nuclides (Hoppe and Ott, 1997), and so the *s*-deficits measured for bulk and silicate samples of the CR chondrites could in principle reflect the incomplete digestion of SiC (or other acid-resistant presolar grains enriched in *s*-process nuclides). If this were the case, then the Mo and W isotope compositions measured for CR metal would reflect those of bulk CR chondrites, because the metal does not contain presolar grains. However, Burkhardt et al. (2011) reported ε^{92}Mo = 3.58±0.64 for a bulk sample of the CR chondrite NWA 801, which is distinct from ε^{92}Mo = 1.85±0.14 (95% CI, n=5) obtained for CR metal (including NWA 801) in the present study. As the bulk NWA 801 sample investigated in Burkhardt et al. (2011) was completely melted by laser fusion prior to acid digestion, all presolar and refractory components should have been completely dissolved. Therefore, the higher ε^{92}Mo of the bulk NWA 801 sample compared to that of CR metal cannot reflect the incomplete digestion of presolar grains. Moreover, the Mo isotope composition of the acid-digested bulk sample of GRA 06100 from the present study is indistinguishable from that of the laser-fused bulk NWA 801, indicating that a potential incomplete dissolution of presolar grains during acid-digestion has no resolvable effect on the measured Mo isotope compositions, at least for bulk CR chondrite samples.

These observations taken together indicate that CR metal exhibits a smaller deficit in *s*-process Mo nuclides than bulk CR chondrites. This in turn requires the presence of at least one component in the bulk sample with a larger *s*-deficit to counterbalance the isotopic composition of the metal. Consequently, non-metal components in CR

chondrites should have a larger *s*-process deficit than the bulk sample. This is consistent with the large deficits in *s*-process Mo isotopes (ε^{92}Mo of up to ~10; Fig. S4) measured for some of the metal-poor samples (i.e., NWA 801 MS-4 and MS-5; Acfer 097 MS-5; NWA 1180 MS-4; GRA 06100 MS-5), which probably most closely represent the composition of CR silicate (Fig. 2). Note that we cannot exclude that some of these large anomalies reflect the incomplete digestion of presolar grains, but we emphasize that the Mo isotope difference between CR metal and the completely digested bulk sample imply the presence of a non-metal component in CR chondrites that is characterized by a larger *s*-process deficit compared to the bulk sample (and the metal), as is observed for the aforementioned metal-poor samples.

The potential effects of incomplete dissolution on the measured W isotope anomalies are more difficult to assess, because of the much smaller anomalies and relatively large uncertainties (Fig. 1). Moreover, no data exist for bulk chondrite samples for which full digestion has been demonstrated, because unlike for the common acid-digestion techniques, other digestion methods (e.g., alkaline fusion) typically result in high W blanks and are therefore avoided. The three bulk CR chondrite samples analyzed in the present study show well-resolved ε^{183}W excesses of ~0.3–0.5; of all bulk meteorites analyzed so far only the IIC iron meteorites have similarly large ε^{183}W excesses (Kruijer et al., 2017). As for Mo isotopes, the bulk ε^{183}W is larger than the ε^{183}W = 0.14±0.06 (95% CI, n=7) measured for the CR metal. Although it cannot be excluded that this difference reflects the incomplete dissolution of an *s*-process carrier in the bulk samples, this is unlikely because the nucleosynthetic W and Mo isotope anomalies are correlated and therefore probably reflect the heterogeneous distribution of the same carrier phase. Thus, because the Mo isotope anomalies are not due to incomplete digestion, there is no reason to assume that the measured W isotope variations would reflect such incomplete digestion. Consequently, both the Mo and W isotope variations measured for bulk samples and separates of CR chondrites are most likely genuine features of these samples.

4.3. Genetic link between silicate and metal in CR chondrites

Despite all samples displaying deficits in *s*-process Mo and W nuclides, metal and silicate in CR chondrites have distinct nucleosynthetic W and Mo isotope anomalies (Figs. 1 and 2). The Mo and W isotope data reveal that, relative to bulk CR chondrites, the metal is enriched and the silicate is depleted in a presolar *s*-process carrier. Thus, these isotope anomalies most likely result from the heterogeneous distribution of the very same carrier. A similar observation has been made for chondrules and matrix from the CV3 chondrite Allende, which exhibit complementarity W and Mo isotope

anomalies that are caused by the depletion and enrichment of a single presolar *s*-process carrier (Budde et al., 2016a; Budde et al., 2016b). Note that 'complementarity' is strictly defined as complementary compositions of two components relative to an *a priori* reference composition for the bulk that shows little or no variations among different meteorites (e.g., Hezel and Palme, 2008). Such an isotopic complementarity *sensu stricto* is only observed for the ε^{183}W compositions of chondrules and matrix from Allende. These samples show ε^{183}W excesses (chondrules) and deficits (matrix) relative to bulk Allende, other bulk meteorites, and inner solar system planets (Earth, Moon, Mars), which are all characterized by $\varepsilon^{183}W \approx 0$ (Budde et al., 2016b). By contrast, for CR chondrites the prerequisite of a well-defined bulk composition is not met, because bulk CR chondrites themselves exhibit nucleosynthetic W (and Mo) isotope anomalies relative to other meteorites and Earth. Thus, the W and Mo isotope anomalies in CR silicate and metal are not complementary relative to a common bulk composition, but they nevertheless reflect the complementary depletion and enrichment of a single *s*-process carrier.

The nature of the *s*-process carrier that is unevenly distributed between CR metal and silicate is difficult to assess, but Budde et al. (2016a) have shown that the complementary W and Mo isotope anomalies of Allende chondrules and matrix most likely result from the preferential incorporation of a metallic presolar *s*-process carrier into the matrix over chondrules. These authors argued for a metallic carrier because the complementary isotope anomalies are only present for siderophile (Mo, W) but not for lithophile (Ba, Ti) elements (Budde et al., 2016a; Gerber et al., 2017), and because the Mo and W isotope anomalies of the Allende chondrules are inversely correlated with the magnetic susceptibility and, hence, initial metal content of the chondrules. Since metal in CR chondrites is enriched in *s*-process nuclides over silicate, it seems likely that the isotopic heterogeneity between CR metal and silicate also reflects the enrichment and depletion of a metallic *s*-process carrier. However, other types of carriers cannot be excluded at this stage.

Regardless of the exact nature of this carrier, an origin of the isotopic anomalies in CR metal and silicate through the enrichment and depletion of a single *s*-process carrier implies that both components derive from the same reservoir of precursor dust. This is because if CR metal and silicate would have formed independently of each other, then there would be no reason why they should be characterized by the enrichment and depletion of the same *s*-process carrier. The isotopic heterogeneity between CR metal and silicate is, therefore, most easily accounted for by the contemporaneous formation of both components from a single reservoir. Such a strong genetic link between CR metal and silicate has also been deduced from the

complementary chemical compositions of chondrules, metal, and matrix from CR chondrites (Kong and Palme, 1999; Kong et al., 1999), and is consistent with the idea that CR metal formed or was reprocessed during formation of CR chondrules (e.g., Kong and Palme, 1999; Connolly et al., 2001; Jacquet et al., 2013).

The formation of CR metal during chondrule formation raises the question of how the distinct nucleosynthetic isotope compositions of CR metal and silicate have been preserved (or formed) during this process. As CR metal also occurs inside chondrules and appears to have equilibrated chemically with the silicates inside the chondrules (e.g., Kong et al., 1999), the distinct isotopic compositions of the CR metal and silicate probably do not reflect the fractionation of metal and silicate grains prior to chondrule formation. Instead this fractionation more likely occurred during chondrule formation itself. As is evident from the preservation of presolar grains in the matrix of CR chondrites, some material escaped thermal processing during chondrule formation, and consequently not all presolar grains present in chondrule precursors were necessarily consumed and homogenized during the melting that produced the chondrules. One possibility therefore is that the chondrule precursors contained presolar metal grains enriched in *s*-process Mo and W and that these grains were not completely destroyed during chondrule formation. It is then conceivable that these metal grains were preferentially incorporated into the metal droplets that had formed during chondrule formation and ultimately coalesced to form the final CR metal. Preserving the distinct nucleosynthetic isotope signatures requires that the presolar grains that were incorporated into the metal droplets did not isotopically equilibrate with the surrounding silicates. This is conceivable if the melting and metal-silicate fractionation process occurred rapidly (as would likely be the case during chondrule formation) and/or if the presolar metal grains themselves did not melt. Of note, the presence of chemically distinct metal grains in CR chondrites (Jacquet et al., 2013) indicates that chemical heterogeneities among metal grains have been preserved in CR chondrites.

In summary, the formation of nucleosynthetic W and Mo isotope anomalies in CR metal and silicate by the enrichment and depletion of a single presolar *s*-process carrier, combined with the chemical complementary of chondrules, matrix, and metal in CR chondrites, indicate that the major components of CR chondrites are genetically linked. As such, they most likely formed together from one common reservoir of solar nebula dust. This and the presence of the nucleosynthetic isotope heterogeneity among CR components indicates that CR chondrules (like most other chondrules) formed by localized melting events of dust aggregates within the solar protoplanetary disk (e.g., Desch et al., 2005; Morris et al., 2012).

5. Hf-W chronology of CR chondrites

5.1. Hf-W isochron ages

Before the Hf-W data can be used to construct isochrons, it is important to assess the effect of nucleosynthetic W isotope anomalies on the measured ε^{182}W values. As noted above, nucleosynthetic anomalies result in correlated variations of ε^{182}W and ε^{183}W, and so the magnitude of nucleosynthetic effects on ε^{182}W can be quantified using the measured ε^{183}W (or ε^{184}W) values for each sample and the slopes of the ε^{182}W–ε^{183}W (or ε^{182}W–ε^{184}W) correlation lines (e.g., Kruijer et al., 2014a). In previous studies on chondrule and matrix separates from the Allende CV3 chondrite (Budde et al., 2016b) and bulk CAIs (Kruijer et al., 2014a), both the initial ^{182}Hf/^{180}Hf and the ε^{182}W–ε^{183}W and ε^{182}W–ε^{184}W slopes were determined iteratively. However, for the CR chondrites this approach cannot be used, because the variation in ε^{183}W among these samples is too small.

Nevertheless, for the chronological interpretation of the Hf-W data this is inconsequential in case of the CR chondrites, because for the ^{186}W/^{183}W-normalized data the correction is smaller than the analytical uncertainty of the W isotope measurements. More specifically, whereas the correction for the ε^{182}W (6/4) values is >1ε for some samples, the correction of the ε^{182}W (6/3) values is typically ~0.04ε and is always <0.08ε, which is smaller than the analytical precision of ±0.15ε for ε^{182}W (6/3). Here, we corrected the measured ε^{182}W (6/3) values for nucleosynthetic anomalies using the ε^{182}W–ε^{184}W slope of +0.12±0.07 previously obtained for Allende chondrules and matrix (Budde et al., 2016b). However, using a different ε^{182}W–ε^{184}W slope of –0.11±0.05, as determined for W isotope data for bulk CAIs (Kruijer et al., 2014a) and leachates from primitive carbonaceous chondrites (Burkhardt and Schönbächler, 2015), does not affect the results and would change the final Hf-W age by only 0.14 Ma, which is negligible compared to the uncertainty of ±0.62 Ma for the final Hf-W age (see below). Note that after correction for nucleosynthetic anomalies, the ε^{182}W (6/3) and ε^{182}W (6/4) values are consistent with each other (Fig. S2).

For each of the CR chondrites, all analyzed samples plot on a single, well-defined correlation line in diagrams of ε^{182}W versus ^{180}Hf/^{184}W (Fig. 6). Since most fractions were obtained mainly based on their magnetic susceptibility, such correlation lines could in principle represent mixing lines between W-rich metal and virtually W-free silicates with different initial ε^{182}W, and may in this case have no chronological significance. However, at least three independent components are required to explain the observed elemental variations in the different CR chondrite samples (Fig. S1). These components are (*i*) Hf-free and W-rich metal, (*ii*) Hf-poor and W-poor silicates

(e.g., olivine, low-Ca pyroxene), and (*iii*) Hf-rich and W-poor silicates (e.g., high-Ca pyroxene) (Kleine et al., 2008). Thus, the observed variations in Hf/W do not only reflect varying abundances of metal, but also different proportions of Hf-rich and Hf-poor silicates. This is also evident from diagrams of ε^{182}W versus 1/W (Fig. S5), in which, for example, all samples combined do not plot on a single mixing line (MSWD = 5.2), whereas they do plot on a single line in an isochron diagram (MSWD = 1.16 for the combined isochron; see below). Thus, the Hf-W data for the CR samples define isochrons and are not mixing lines.

The isochron regressions were calculated using the 'Model 1 fit' of *Isoplot* (version 3.76), which is a York regression weighting the data-points proportional to the inverse square of their assigned errors (Ludwig, 2012), and the results are shown in Fig. 6 [uncertainties are 95% confidence intervals (95% CI)]. Relative to the $(^{182}Hf/^{180}Hf)_i$ = (1.018±0.043)×10^{-4} of CV CAIs (Kruijer et al., 2014a) and using λ^{182}Hf = 0.0778±0.0015 Ma^{-1} (Vockenhuber et al., 2004), the initial $^{182}Hf/^{180}Hf$ obtained for each CR chondrite yield Hf-W ages between 2.9±1.0 Ma (GRA 06100) and 4.3±0.9 Ma (NWA 1180) after CAI formation. Moreover, the $(^{182}Hf/^{180}Hf)_i$ obtained from the individual isochrons are indistinguishable within their uncertainties and all samples combined define a single precise isochron with an initial $^{182}Hf/^{180}Hf$ = (7.68±0.17)×10^{-5} (MSWD=1.16, n=38), corresponding to an Hf-W age of 3.63±0.62 Ma (2σ) after CAI formation (Fig. 7a).

5.2. Significance of Hf-W ages

Although CR chondrites are some of the least altered chondrites, they have been modified by parent body processes, raising the question of whether these processes had any effect on the Hf-W systematics. CR chondrites typically underwent only mild if any thermal metamorphism with temperatures of less than ~200 °C (e.g., Briani et al., 2013), but most CR chondrites were affected to some degree by aqueous alteration on the parent body (e.g., Krot et al., 2002). Although this alteration resulted in the exchange of some fluid-mobile elements between chondrules and matrix (Bland et al., 2005), such effects have only been observed for strongly altered CR chondrites (of petrologic types 2.3 and 2.4). However, even in these samples no significant redistribution of elements other than Sr and U between the different components was observed, making it quite unlikely that Hf and W would have been affected. Moreover, all CR chondrites investigated here are less strongly altered, corresponding to petrologic type 2.5 to 2.8 (Section 2.1).

Of the four investigated CR chondrites, GRA 06100 is the most strongly altered sample, and this sample also shows evidence for some redistribution of W (see

supplementary material for details). GRA 06100 has undergone substantial metamorphism, most likely as a consequence of shock-heating during an impact event, where peak metamorphic temperatures might have reached ~600 °C (Abreu and Bullock, 2013). However, even this temperature is lower than the Hf-W closure temperature of ~800–900 °C (Kleine et al., 2008), indicating that any effects of diffusional exchange of Hf and W during thermal metamorphism were likely small. This is consistent with the observation that the Hf-W age of GRA 06100 is in good agreement with those of the other CR chondrites. In spite of the different degrees of aqueous alteration and thermal metamorphism, all samples yield consistent Hf-W isochrons with no evidence for excess scatter (MSWD between 0.59 and 1.5). A regression of all samples, but excluding GRA 06100, yields $(^{182}Hf/^{180}Hf)_i$ = $(7.61\pm0.18)\times10^{-5}$, indistinguishable from the value obtained from the regression including all samples (Section 5.1). Thus, in spite of the more intense parent body processes evident for GRA 06100, the Hf-W systematics in this sample are not disturbed and there is, therefore, no evidence that parent body processes affected the Hf-W system in the investigated CR chondrites.

The major process fractionating Hf and W in CR chondrites is metal-silicate separation and the Hf-W age, therefore, provides the time of the last metal-silicate equilibration in CR chondrites. As most CR metal is located inside chondrules and, hence, was formed or reprocessed during chondrule formation (Kong et al., 1999), the Hf-W age of metal-silicate separation should also closely approximate the time of chondrule formation. Two observations indicate that this is the case. First, an isochron regression including only chondrule metal and chondrule silicate fractions yields an initial $^{182}Hf/^{180}Hf$ = $(7.62\pm0.36)\times10^{-5}$ (MSWD=0.93, n=8; Fig. 7b), which is in excellent agreement with the $(^{182}Hf/^{180}Hf)_i$ obtained from the combined isochron (Fig. 7a). Second, as will be shown in more detail below (Section 5.3), the Hf-W age of CR chondrites of 3.6±0.6 Ma is in excellent agreement with the Al-Mg age of CR chondrules of ~3.7 Ma after CAIs (Schrader et al., 2017). Thus, metal-silicate fractionation (as dated by Hf-W) and chondrule formation (as dated by Al-Mg) were coeval in CR chondrites. This is consistent with the chemical complementarity and nucleosynthetic isotope heterogeneity among chondrules, matrix, and metal in CR chondrites, which indicates that these components are co-genetic and, hence, formed together from a single reservoir of solar nebula dust (Section 4.3).

A final important question related to the significance of the Hf-W ages is as to whether the presence of nucleosynthetic W isotope variations among CR components would imply the lack of W isotope equilibration among these components. However, the presolar grains that cause the nucleosynthetic isotope heterogeneity contain only a

negligible amount of the bulk W present in CR metal and silicate, meaning that the heterogeneous distribution of presolar grains has no effect on the chemical fractionation and equilibration of Hf and W between silicate and metal. In other words, the nucleosynthetic W isotope anomalies simply reflect the complementary depletion and enrichment of presolar grains between two components that otherwise were in isotopic equilibrium. Moreover, as noted above, the effect of nucleosynthetic W isotope anomalies are very small for the ε^{182}W values normalized to ^{186}W/^{183}W. Thus, using these data in the isochron regression makes it possible to assess whether there had been any primordial W isotope heterogeneity unrelated to the nucleosynthetic W isotope variations. Of note, the ε^{182}W (6/3) data provide precise isochrons for CR metal and silicate, demonstrating that there was no initial W isotope heterogeneity (other than the nucleosynthetic variations) among the components used to define the isochrons.

5.3. Comparison to Al-Mg ages for CR chondrules

Nagashima et al. (2014) and Schrader et al. (2017) reported Al-Mg isotope data for individual chondrules from nine different CR2 chondrites, one of which (El Djouf 001) is paired with Acfer 097 that was analyzed in the present study (Bischoff et al., 1993). The majority of the analyzed chondrules display no resolved ^{26}Mg excesses, where the upper limit of $(^{26}Al/^{27}Al)_i$ of ~3×10^{-6} translates into Al-Mg ages of >3 Ma after CAI formation for these chondrules. Seven of the 22 investigated chondrules, however, show resolved ^{26}Mg excesses, corresponding to initial ^{26}Al/^{27}Al of between 1.0×10^{-6} and 6.3×10^{-6}. These translate into Al-Mg ages of 2.2−4.0 Ma after CAI formation, relative to the $(^{26}Al/^{27}Al)_i = (5.23\pm0.13)\times10^{-5}$ of Allende CAIs (Jacobsen et al., 2008). Schrader et al. (2017) observed that there is no relationship between oxygen isotope composition, Fe#, and $(^{26}Al/^{27}Al)_i$ and, on this basis, argued that aqueous alteration on the CR chondrite parent body did not result in disturbance of the Al-Mg systematics in the chondrules. The Al-Mg ages should, therefore, record the time of CR chondrule formation. Schrader et al. (2017) used the weighted mean of the initial ^{26}Al/^{27}Al obtained from the internal isochron slopes of 21 CR chondrules (excluding one chondrule with an anomalously high $(^{26}Al/^{27}Al)_i$ that corresponds to an Al-Mg age of ~2.2 Ma) to determine a preferred Al-Mg age of 3.75±0.24 Ma after CAIs for the formation of CR chondrules.

One problem with the interpretation of the Al-Mg data for CR chondrules is that many of them do not show resolved radiogenic ^{26}Mg excesses. For these chondrules, the Al-Mg data, therefore, only provide maximum ages, making it difficult to assess as to whether the majority of CR chondrules formed in a narrow time interval at 3.75±0.24 Ma or over a longer period of time. Likewise, as the Hf-W ages were not obtained on

single chondrules but on fractions consisting of large amounts of chondrules and chondrule fragments, a potential age range of individual chondrules would be averaged out and the Hf-W age would then only provide a mean age of chondrule formation. However, the good agreement of the Al-Mg age of 3.75±0.24 Ma with the Hf-W age of 3.63±0.62 Ma indicates that CR chondrules formed within a narrow time interval. This is because if there were chondrules with formation ages significantly younger than ~4 Ma, then there should also be chondrules with formation ages significantly older than ~3 Ma; this would be necessary to maintain an average chondrule formation age of ~3.6 Ma. However, the Al-Mg data show that 21 out of 22 CR chondrules have Al-Mg ages >3 Ma, precluding the possibility that there are many CR chondrules with formation ages significantly younger than ~4 Ma. Thus, as already noted by Schrader et al. (2017), the unresolved ^{26}Mg excesses in some CR chondrules are most likely attributable to their formation at the end of the effective lifetime of ^{26}Al, when any ^{26}Mg excess becomes small and, hence, difficult to resolve with current analytical techniques.

5.4. Comparison to Pb-Pb ages for CR chondrules

Amelin et al. (2002) reported a ^{207}Pb-^{206}Pb age of 4564.7±0.6 Ma for a set of six chondrules from the CR chondrite Acfer 059, which is paired with Acfer 097 that was analyzed in this study (Bischoff et al., 1993). However, this age was calculated using an assumed ^{238}U/^{235}U = 137.88, which has since been shown to be incorrect for most solar system objects (e.g., Goldmann et al., 2015). Schrader et al. (2017) determined a ^{238}U/^{235}U of 137.779±0.009 for bulk CR chondrites, which is consistent with the ^{238}U/^{235}U of 137.786±0.016 directly measured for pooled chondrule separates from Allende (Brennecka et al., 2015), and translates into a U-corrected age of 4563.6±0.6 Ma for the pooled Acfer 059 chondrules. Using the Pb-Pb age of CV CAIs of 4567.30±0.16 Ma (Connelly et al., 2012), the Pb-Pb age of Acfer 059 chondrules translates into a time difference of 3.66±0.63 Ma between the formation of CAIs and CR chondrules. This age for CR chondrule formation is in very good agreement with the Hf-W and Al-Mg ages of 3.63±0.62 Ma and 3.75±0.24 Ma, respectively. Thus, three independent chronometers provide concordant ages for the formation of CR chondrules (Fig. 8).

However, matters become more complicated when Pb-Pb ages for individual chondrules are also considered. Bollard et al. (2017) reported Pb-Pb ages for seven individual CR chondrules from two different CR2 chondrites with an apparent age range of ~4 Ma. Whereas four of the CR chondrules have Pb-Pb ages that agree within uncertainty with the Pb-Pb age for the multi-chondrule fraction and the Al-Mg and Hf-W

ages for CR chondrules (see above), three chondrules have older Pb-Pb ages, where one chondrule apparently formed as early as CAIs. On this basis, Bollard et al. (2017) argued that CR chondrules formed continuously over a period of ~4 Ma. However, such an extended period of CR chondrule formation is inconsistent with several other observations. First, the inferred ~4 Ma range of chondrule formation ages is not apparent in the Al-Mg ages for CR chondrules. The vast majority (21 out of 22) of CR chondrules has Al-Mg ages of >3 Ma (Schrader et al., 2017), whereas one single CR chondrule has a reported Al-Mg age of 2.2±0.2 Ma (Nagashima et al., 2014). As noted above, the weighted average Al-Mg age of CR chondrules is 3.75±0.24 Ma after CAI formation. By contrast, the average Pb-Pb age of the seven CR chondrules reported in Bollard et al. (2017) is 2.0±1.3 Ma (95% CI) after CAI formation. Thus, the Al-Mg ages are inconsistent with the range of Pb-Pb ages, and are on average also ~1.5 Ma younger. Bollard et al. (2017) argued that this mismatch reflects a reduced initial ^{26}Al abundance in the precursor material of CR chondrites. However, this possibility is ruled out by the good agreement of the Al-Mg, Hf-W, and Pb-Pb ages obtained for pooled CR chondrule separates (Fig. 8), and also by the good agreement between Al-Mg and Hf-W ages for several other meteorites (Section 6). The mismatch between the Pb-Pb and Al-Mg ages also cannot reflect a heterogeneous distribution of ^{26}Al at the scale of individual chondrules, because this would result in a larger and not smaller apparent range in the Al-Mg ages.

Second, regardless of the duration of CR chondrule formation, the average age of CR chondrules is ~3.6 Ma (Fig. 8). Consequently, if there were a significant fraction of CR chondrules that formed within ~1 Ma of CAI formation, then there must also be a large number of chondrules that formed significantly later than ~4 Ma after CAIs. This would be necessary to counterbalance the very old chondrule ages to result in an average age of ~3.6 Ma after CAIs. However, there are no CR chondrules with reported ages younger than ~4 Ma after CAIs. Moreover, ^{53}Mn-^{53}Cr ages for carbonates from CR chondrites show that aqueous alteration and carbonate formation started at ~4-5 Ma after CAIs (Jilly-Rehak et al., 2017). As chondrule formation obviously must predate aqueous alteration on the parent body, the Mn-Cr carbonate ages rule out that CR chondrules could have formed as late as 4–5 Ma after CAIs. Moreover, to facilitate heating and formation of aqueous fluids that ultimately lead to alteration, there must be a time gap between chondrule formation (and hence chondrite accretion) and parent body alteration. This is consistent with results of Sugiura and Fujiya (2014), who inferred an accretion age for the CR parent body of 3.5±0.5 Ma after CAIs, using model calculations of the initial ^{26}Al/^{27}Al based on peak metamorphic temperatures of CR chondrites. Thus, these data combined indicate that there should

be no CR chondrules that formed later than ~4 Ma after CAIs. As this age limit is very close to the average age of CR chondrules of ~3.6 Ma, there is not much room for CR chondrule ages significantly younger than ~3.6 Ma. A corollary of this is that the majority of CR chondrules most likely formed in a narrow time interval of about ±0.3 Ma, as given by the uncertainty of the Al-Mg age and the scatter of the Hf-W isochron (note that the uncertainty on the $(^{182}Hf/^{180}Hf)_i$ obtained from the combined CR chondrite isochron corresponds to an age uncertainty of ±0.3 Ma).

In summary, the variable Pb-Pb ages reported for individual CR chondrules are difficult to reconcile with other chronological constraints for the formation of components in CR chondrites, including the Al-Mg ages for CR chondrules, the Hf-W age for metal-silicate fractionation, as well as independent constraints on the time of CR parent body accretion. Although the reason for this discrepancy is unclear at present, all data combined reveal that the range of Pb-Pb ages and, in particular, Pb-Pb ages for CR chondrules that are as old as CAIs cannot be representative for the entire suite of CR chondrules.

5.5. Link between chondrule formation and parent body accretion

The chronological data summarized above suggest strongly that CR chondrules formed within a narrow time interval at ~3.6 Ma after CAI formation. This and the close agreement of this age with independent constraints on the timing of CR parent body accretion derived from thermal modeling (3.5±0.5 Ma; Sugiura and Fujiya, 2014) and Mn-Cr ages for CR carbonates (Jilly-Rehak et al., 2017) indicate a strong temporal link between the formation of CR chondrules and accretion of the CR chondrite parent body. Such a link is also consistent with complementary patterns of moderately volatile elements in chondrule and matrix fractions from CR chondrites, which suggest that CR parent body accretion occurred very shortly after chondrule formation (Kong and Palme, 1999; Kong et al., 1999), and with the nucleosynthetic isotope heterogeneity between CR silicate and metal observed in the present study (Section 4.3).

A close temporal link between chondrule formation and chondrite accretion has previously also been inferred for other groups of chondrites, based on the chemical (e.g., Bland et al., 2005; Hezel and Palme, 2008; Palme et al., 2015; Ebel et al., 2016) and isotopic complementarity of chondrules and matrix in CV chondrites (Budde et al., 2016b), as well as the distinct chemical and physical properties of chondrules from a given chondrite group (e.g., Alexander et al., 2008). This is because maintaining these distinct features in a turbulent solar nebula is best accounted for by a rapid accretion of chondrules to their parent body (e.g., Alexander et al., 2008; Budde et al., 2016b). Goldberg et al. (2015) argued that the complementarity of chondrite components does

not necessarily imply immediate accretion to a parent body, provided that solids and gas are tightly coupled to each other. Under these conditions, distinct dust populations could in principle have been preserved over an extended period of time. However, these models provide no precise estimate on the possible time gap between chondrule formation and chondrite accretion (Goldberg et al., 2015). By contrast, the chronological data for CR chondrites indicate a rapid accretion of CR components after chondrule formation.

6. Distribution of ^{26}Al in the early solar system

In addition to providing constraints on the timescales of metal-silicate fractionation and chondrule formation in CR chondrites, the Hf-W data have important implications for assessing the degree to which ^{26}Al was homogeneously distributed within the solar protoplanetary disk. This is important because the interpretation of variable initial ^{26}Al/^{27}Al as age differences relies on the assumption that ^{26}Al was homogeneously distributed in the early solar system. However, as to whether this was the case remains debated (e.g., Villeneuve et al., 2009; Larsen et al., 2011; Krot et al., 2012; Kruijer et al., 2014a; Schiller et al., 2015). It is generally accepted that ^{26}Al was heterogeneously distributed (at least on a small scale) at the very beginning of the solar system, as is evident from ^{26}Al-poor (and ^{26}Al-rich) refractory objects such as platy hibonite crystals (PLACs), corundum grains, and FUN CAIs in primitive meteorites (e.g., Wasserburg et al., 1977; Makide et al., 2011; Liu et al., 2012; Park et al., 2017). In contrast, most CAIs from CV chondrites formed with a homogeneous initial ^{26}Al/^{27}Al of ~5.2×10^{-5} (e.g., Jacobsen et al., 2008; MacPherson et al., 2012), and it is generally assumed that this 'canonical' ^{26}Al/^{27}Al is representative for most bulk solar system materials at the beginning of solar system history. However, this assumption has been repeatedly questioned, and both Larsen et al. (2011) and Schiller et al. (2015) argued that at the time of CAI formation most inner solar system materials were characterized by much lower ^{26}Al/^{27}Al than CAIs themselves. Evidence for this inferred heterogeneous distribution of ^{26}Al (at the bulk meteorite scale) is derived from the observation of correlated ^{26}Mg and ^{54}Cr variations in bulk meteorites and individual chondrules (Larsen et al., 2011; Van Kooten et al., 2016; Olsen et al., 2016), as well as disparate Al-Mg and Pb-Pb ages for some angrites (Schiller et al., 2015). Other studies, however, found a good agreement between Al-Mg and Pb-Pb ages for the ungrouped achondrite NWA 2976 (Bouvier et al., 2011) and between Al-Mg and Hf-W ages for CAIs and angrites (Kruijer et al., 2014a), both arguing for a homogeneous distribution of ^{26}Al.

The Hf-W data for CR chondrites obtained in the present study provide critical new information regarding the issue of the distribution of ^{26}Al in the early solar system. There are now four different groups of meteorite samples for which both Al-Mg and Hf-W data exist (Table 3): Bulk CV CAIs, the angrites D'Orbigny and Sahara 99555, as well as chondrules from CV and CR chondrites. Collectively, these samples formed over nearly the entire effective lifetime of ^{26}Al, which covers the first ~5 Ma of solar system history (Fig. S6). As these samples not only formed at different times but also derive from different reservoirs within the solar protoplanetary disk, they are well suited to assess the concordance of the Al-Mg and Hf-W chronometers.

Nyquist et al. (2009) have shown that for assessing the concordance of ages obtained from short-lived chronometers, it is useful to plot the natural logarithms of the initial abundance ratios against each other. This is because in a diagram of $\ln(^{26}Al/^{27}Al_i)$ versus $\ln(^{182}Hf/^{180}Hf_i)$ samples with concordant Al-Mg and Hf-W ages will plot on a single correlation line whose slope is equivalent to the ratio of the ^{26}Al and ^{182}Hf decay constants. Using $\lambda^{26}Al = 0.979\pm0.024$ Ma^{-1} (Nishiizumi, 2004) and $\lambda^{182}Hf = 0.0778\pm0.0015$ Ma^{-1} (Vockenhuber et al., 2004), the calculated $(\lambda^{26}Al)/(\lambda^{182}Hf)$ is 12.6±0.4. Figure 9 shows the initial $^{26}Al/^{27}Al$ and $^{182}Hf/^{180}Hf$ for bulk CAIs, angrites, as well as CV and CR chondrules plotted against each other. As it is unclear to what extent the Al-Mg system in CV chondrules was modified during thermal metamorphism and aqueous alteration on the parent body (e.g., Alexander and Ebel, 2012), we here only used Al-Mg data for chondrules from Kaba, which is one of the least metamorphosed CV chondrites (Nagashima et al., 2017, and references therein). Chondrules from Kaba are characterized by uniform initial $^{26}Al/^{27}Al$, with a mean $(^{26}Al/^{27}Al)_i$ of $(4.84\pm0.88)\times10^{-6}$ (95% CI; Nagashima et al., 2017). For CR chondrites we used the weighted mean $(^{26}Al/^{27}Al)_i$ of $(1.33\pm0.29)\times10^{-6}$ for CR chondrules as given in Schrader et al. (2017) (see Section 5.3 for details). For angrites we used an initial $^{26}Al/^{27}Al$ of $(3.99\pm0.19)\times10^{-7}$, as obtained from a combined isochron regression of Al-Mg data for D'Orbigny and Sahara 99555 from three studies (Spivak-Birndorf et al., 2009; Schiller et al., 2010; Schiller et al., 2015). Further data sources are provided in Table 3.

As shown in Fig. 9, using these data results in a well-defined linear correlation in a plot of $\ln(^{26}Al/^{27}Al_i)$ versus $\ln(^{182}Hf/^{180}Hf_i)$. The slope of this ^{26}Al–^{182}Hf correlation line is 12.9±1.4 and is in very good agreement with the slope of 12.6±0.4 expected from the ratio of the ^{26}Al and ^{182}Hf decay constants. Thus, for four groups of samples (CAIs, angrites, CV and CR chondrules) the Al-Mg and Hf-W systems are concordant and indicate a closed system evolution from a reservoir with common initial $^{26}Al/^{27}Al$ and $^{182}Hf/^{180}Hf$ as defined by CV CAIs. Taken together, the linearity of the data combined

with the good agreement between the observed and predicted slopes provides strong evidence for a homogeneous distribution of ^{26}Al at the scale of bulk CAIs and bulk meteorites.

Although the Al-Mg and Hf-W ages are concordant, it is useful to quantify the degree of ^{26}Al heterogeneity that would still be permitted. This is important because owing to the much shorter half-life of ^{26}Al compared to ^{182}Hf, small ^{26}Al heterogeneities may still exist that could not be resolved using the Hf-W system. A conservative approach is to use the 95% CI error envelope of the ^{26}Al–^{182}Hf regression (as shown in Fig. 9), in which case the permissible heterogeneity in ^{26}Al/^{27}Al would range from about ±20% at the time of angrite and CR chondrule formation (i.e., ~4–5 Ma after CAIs) to $^{+61\%}/_{-36\%}$ at the time of CAI formation (see Fig. 10 for details). However, this approach ignores the fact that there is essentially no scatter on the ^{26}Al–^{182}Hf correlation line, as is evident from the very low MSWD of 0.11 and a correlation coefficient of the regression that is close to unity (R^2 = 0.999). Thus, the observed scatter of the data points from the regression line is much smaller than the expected scatter from the assigned errors. In other words, the uncertainty on the ^{26}Al–^{182}Hf regression is mainly dominated by analytical errors and not by non-analytical scatter (Ludwig, 2012). This is important, because only the latter scatter would be indicative of a potential ^{26}Al heterogeneity. Thus, to assess the permissible degree of ^{26}Al heterogeneity it is more appropriate to use the 'observed scatter' of the regression, which is independent of the assigned (i.e., analytical) errors (Ludwig, 2012). Using this approach, the highest possible degree of ^{26}Al heterogeneity is below about ±10% at any point in time after ~1.6 Ma and about ±15% at the time of CAI formation (Fig. 10). It should be emphasized, however, that these values only provide maximum estimates and by no means indicate or require an actual heterogeneity in the distribution of ^{26}Al. The data instead indicate and are fully consistent with a homogeneous distribution of ^{26}Al in the early solar system.

This result is inconsistent with the high level of ^{26}Al heterogeneity proposed in some previous studies (Larsen et al., 2011; Schiller et al., 2015; Olsen et al., 2016). These studies inferred ^{26}Al/^{27}Al for different chondrite and achondrite parent bodies as well as individual (CV and CR) chondrules that at the time of CAI formation were 46–97% lower than the ratio measured in CAIs (Fig. 10). However, such high levels of ^{26}Al/^{27}Al heterogeneity can be ruled out based on the well-defined ^{26}Al–^{182}Hf correlation (regardless of which error estimate is used for this correlation), indicating that (at any given point in time) the formation regions of CV CAIs, CV chondrules, CR chondrules, and angrites were characterized by uniform ^{26}Al/^{27}Al to within better than about ±10%. Given that these samples represent material that formed at different times and derive from distinct reservoirs within the solar protoplanetary disk, the concordance of Al-Mg

and Hf-W ages provides strong evidence for a disk-wide homogeneous distribution of ^{26}Al in the early solar system, at least at the scale of bulk meteorites.

7. Implications for planetary accretion in the early solar system

The chronological and isotopic data for CR chondrites and their components presented here have some broader implications for processes of planetary accretion and the early evolution of the solar system. For instance, CR chondrites seem to have formed later and at greater heliocentric distance than most other chondrites. The formation of CR chondrules at ~3.6 Ma after CAIs indicates that these chondrules are ~1–2 Ma younger than chondrules from all other chondrite groups investigated to date, including ordinary and carbonaceous chondrites (e.g., L, LL, CO, CV) that typically have ages of ~2 Ma after CAI formation (e.g., Rudraswami and Goswami, 2007; Kurahashi et al., 2008; Hutcheon et al., 2009; Villeneuve et al., 2009; Ushikubo et al., 2013; Budde et al., 2016b; Nagashima et al., 2017). The only exception are chondrules from CB chondrites, which probably formed at ~5 Ma after CAIs (Krot et al., 2005; Kleine et al., 2005; Bollard et al., 2015) and thus are still younger than the CR chondrules. The CB chondrites testify to a unique formation mechanism, however, involving condensation from an impact-generated vapor plume (e.g., Krot et al., 2005). As such, the origin of CB chondrules is different from that of other, 'normal' chondrules, which most likely formed by transient melting of dust aggregates in the solar nebula. Consequently, of these normal chondrules, CR chondrules are the youngest, indicating that chondrule formation in the solar nebula occurred over a period of several million years, although chondrules from a given chondrite group most likely formed within a narrow time interval (Section 5.4).

Moreover, bulk CR chondrites are characterized by a significant ε^{183}W excess of ~0.4 that is accompanied by very large nucleosynthetic Mo isotope anomalies (ε^{92}Mo ≈ 3.9). This distinguishes them from most bulk meteorites analyzed to date, which show only small (i.e., ~0.1) if any ε^{183}W anomalies (e.g., Qin et al., 2008; Budde et al., 2016b). Only IIC iron meteorites display a similarly high ε^{183}W excess (Kruijer et al., 2017). It is noteworthy that both IIC irons and CR chondrites are also characterized by elevated δ^{15}N of ~150‰ (Prombo and Clayton, 1993, and references therein). The enrichment of heavy nitrogen in IIC irons and CR chondrites is thought to reflect an incorporation of ^{15}N-rich components produced in the cold, outer regions of the protoplanetary disk, implying that their parent bodies formed at greater heliocentric distance than those of most other meteorites (Füri and Marty, 2015; Van Kooten et al., 2016). Formation of CR chondrites at a relatively great heliocentric distance, combined

with the 'late' accretion of the CR chondrite parent body at ~3.6 Ma after CAI formation, indicates that planetesimal accretion rates decreased with increasing heliocentric distance, consistent with theoretical predictions of some planetesimal formation models (e.g., Bottke et al., 2006).

The evidence for the formation of CR chondrites at a greater heliocentric distance, and the inferred genetic link between CR chondrites and IIC irons is consistent with the Mo isotope signatures of both meteorites (this study; Kruijer et al., 2017), which link them to the carbonaceous (CC) group of meteorites (Budde et al., 2016a). As both the carbonaceous and non-carbonaceous (NC) reservoirs contain iron meteorites and chondrites that formed over several million years, these data require that these two reservoirs co-existed and remained spatially separated for several million years (Budde et al., 2016a; Kruijer et al., 2017). This efficient separation of two reservoirs probably reflects the early formation of Jupiter, which cleared the protoplanetary disk between the inner and outer solar system regions parental to the NC and CC meteorites, respectively (Budde et al., 2016a). Based on Hf-W chronometry of iron meteorites (Kruijer et al., 2014b; Kruijer et al., 2017), this gap was established early, most likely within <1 Ma after CAI formation (Budde et al., 2016a; Kruijer et al., 2017). The data presented here demonstrate that the two reservoirs remained isolated from each other at least until the CR chondrite parent body accreted. This is because all CR chondrite components plot on the 'CC-line' in ^{95}Mo–^{94}Mo space (Fig. 5), indicating that they all have the same and uniform *r*-process enrichment that is characteristic for carbonaceous meteorites in general (Section 4.1; Budde et al., 2016a). Thus, until at least the time the CR components formed, there had been no mixing between the CC and NC reservoirs, meaning that both reservoirs were still isolated from each other. Consequently, the young formation age of CR components requires that the two reservoirs remained separated until at least ~3.6 Ma after CAIs.

Mixing between the CC and NC reservoirs probably occurred through scattering of bodies from beyond Jupiter's orbit, either related to an inward-then-outward migration of Jupiter (Walsh et al., 2011) or due to runaway gas accretion of Jupiter on a fixed orbit (Kretke et al., 2016). The chronological data for CR chondrites, therefore, indicates that this process can have started no earlier than ~3.6 Ma after CAI formation. As runaway gas accretion and migration started when Jupiter reached ~50 Earth's masses, these data constrain this part of Jupiter's accretion history to later than ~3.6 Ma after CAI formation. This is consistent with evidence from CB chondrites, which have been used to argue that migration of Jupiter occurred at ~5 Ma after CAIs (Johnson et al., 2016).

8. Conclusions

The Hf-W and Mo isotope systematics of metal, silicate, and chondrule separates from four different CR chondrites were investigated to place new constraints on their age and formation process. Metal and silicate components of CR chondrites have distinct nucleosynthetic W and Mo isotope anomalies that are caused by the enrichment of a presolar *s*-process carrier in the metal, and the depletion of the same carrier in the silicate. This finding is consistent with the isotopic complementarity of chondrules and matrix from the CV chondrite Allende (Budde et al., 2016a; Budde et al., 2016b). Collectively, these data indicate that the major components of a given chondrite are genetically linked and as such formed together from a single reservoir, most likely by localized melting of dust aggregated in the solar nebula.

The obtained Hf-W age for metal-silicate fractionation in CR chondrites of 3.6±0.6 Ma after CAI formation is indistinguishable from the ~3.7 Ma Al-Mg age for the formation of CR chondrules (Schrader et al., 2017). This is consistent not only with the idea that metal in CR chondrites formed during chondrule formation, but also with the genetic link between CR metal and silicate deduced from their nucleosynthetic isotope anomalies. The various chronological data for CR chondrites, combined with the evidence from the nucleosynthetic isotope heterogeneity and complementary chemical compositions among CR components, indicate that CR chondrules formed in a narrow interval of time and that chondrule formation and chondrite accretion were closely linked. This makes the CR chondrite parent body one of the youngest meteorite parent bodies, which accreted ~1–2 Ma later than the parent bodies of ordinary, CV, and CO chondrites.

Given that the nucleosynthetic Mo isotope anomalies in CR metal and silicate show no evidence for mixing between the non-carbonaceous and carbonaceous meteorite reservoirs, the ~3.6 Ma accretion age of the CR chondrite parent body provides the earliest possible time at which the growth of Jupiter can have led to the scattering of carbonaceous meteorite-type bodies from the outer into the inner solar system. Finally, the concordance of the Hf-W and Al-Mg ages for CR chondrules, combined with concordant Hf-W and Al-Mg ages for CV chondrules and angrites, provides strong evidence for a disk-wide, homogeneous distribution of ^{26}Al in the early solar system, demonstrating that different initial ^{26}Al/^{27}Al in bulk meteorites and (most) meteoritic components have chronological significance.

Acknowledgments

We gratefully acknowledge the Meteorite Working Group (NASA) for providing the Antarctic meteorite sample (GRA 06100) analyzed in this study. We thank two anonymous reviewers for their constructive comments and N. Dauphas for his editorial efforts. Finally, we are also grateful to C. Burkhardt, K. Metzler, A. Bischoff, and Erik Scherer for discussions. This study was supported by the Deutsche Forschungsgemeinschaft (DFG) as part of the Priority Program SPP 1385 (grant KL 1857/3) and the Collaborative Research Centre SFB-TRR 170. These sources of funding are gratefully acknowledged. This is TRR 170 publication no.14.

References

Abreu N. M. and Bullock E. S. (2013) Opaque assemblages in CR2 Graves Nunataks (GRA) 06100 as indicators of shock-driven hydrothermal alteration in the CR chondrite parent body. *Meteorit. Planet. Sci.* **48,** 2406-2429.

Alexander C. M. O. D., Grossman J. N., Ebel D. S. and Ciesla F. J. (2008) The Formation Conditions of Chondrules and Chondrites. *Science* **320,** 1617-1619.

Alexander C. M. O. D. and Ebel D. S. (2012) Questions, questions: Can the contradictions between the petrologic, isotopic, thermodynamic, and astrophysical constraints on chondrule formation be resolved? *Meteorit. Planet. Sci.* **47,** 1157-1175.

Amelin Y., Krot A. N., Hutcheon I. D. and Ulyanov A. A. (2002) Lead Isotopic Ages of Chondrules and Calcium-Aluminum–Rich Inclusions. *Science* **297,** 1678-1683.

Bischoff A., Palme H., Ash R. D., Clayton R. N., Schultz L., Herpers U., Stöffler D., Grady M. M., Pillinger C. T., Spettel B., Weber H., Grund T., Endreβ M. and Weber D. (1993) Paired Renazzo-type (CR) carbonaceous chondrites from the Sahara. *Geochim. Cosmochim. Acta* **57,** 1587-1603.

Bland P. A., Alard O., Benedix G. K., Kearsley A. T., Menzies O. N., Watt L. E. and Rogers N. W. (2005) Volatile fractionation in the early solar system and chondrule/matrix complementarity. *Proc. Natl. Acad. Sci. USA* **102,** 13755-13760.

Bollard J., Connelly J. N. and Bizzarro M. (2015) Pb-Pb dating of individual chondrules from the CB_a chondrite Gujba: Assessment of the impact plume formation model. *Meteorit. Planet. Sci.* **50,** 1197-1216.

Bollard J., Connelly J. N., Whitehouse M. J., Pringle E. A., Bonal L., Jørgensen J. K., Nordlund Å, Moynier F. and Bizzarro M. (2017) Early formation of planetary building blocks inferred from Pb isotopic ages of chondrules. *Sci. Adv.* **3,** e1700407.

Bottke W. F., Nesvorný D., Grimm R. E., Morbidelli A. and O'Brien D. P. (2006) Iron meteorites as remnants of planetesimals formed in the terrestrial planet region. *Nature* **439,** 821-824.

Bouvier A., Spivak-Birndorf L. J., Brennecka G. A. and Wadhwa M. (2011) New constraints on early Solar System chronology from Al–Mg and U–Pb isotope systematics in the unique basaltic achondrite Northwest Africa 2976. *Geochim. Cosmochim. Acta* **75,** 5310-5323.

Brandon A. D., Humayun M., Puchtel I. S., Leya I. and Zolensky M. (2005) Osmium Isotope Evidence for an s-Process Carrier in Primitive Chondrites. *Science* **309,** 1233-1236.

Brennecka G. A., Budde G. and Kleine T. (2015) Uranium isotopic composition and absolute ages of Allende chondrules. *Meteorit. Planet. Sci.* **50,** 1995-2002.

Briani G., Quirico E., Gounelle M., Paulhiac-Pison M., Montagnac G., Beck P., Orthous-Daunay F. R., Bonal L., Jacquet E., Kearsley A. and Russell S. S. (2013) Short duration thermal metamorphism in CR chondrites. *Geochim. Cosmochim. Acta* **122,** 267-279.

Budde G., Burkhardt C., Brennecka G. A., Fischer-Gödde M., Kruijer T. S. and Kleine T. (2016a) Molybdenum isotopic evidence for the origin of chondrules and a distinct genetic heritage of carbonaceous and non-carbonaceous meteorites. *Earth Planet. Sci. Lett.* **454,** 293-303.

Budde G., Kleine T., Kruijer T. S., Burkhardt C. and Metzler K. (2016b) Tungsten isotopic constraints on the age and origin of chondrules. *Proc. Natl. Acad. Sci. USA* **113,** 2886-2891.

Burkhardt C., Kleine T., Bourdon B., Palme H., Zipfel J., Friedrich J. M. and Ebel D. S. (2008) Hf–W mineral isochron for Ca,Al-rich inclusions: Age of the solar system and the timing of core formation in planetesimals. *Geochim. Cosmochim. Acta* **72,** 6177-6197.

Burkhardt C., Kleine T., Oberli F., Pack A., Bourdon B. and Wieler R. (2011) Molybdenum isotope anomalies in meteorites: Constraints on solar nebula evolution and origin of the Earth. *Earth Planet. Sci. Lett.* **312,** 390-400.

Burkhardt C., Kleine T., Dauphas N. and Wieler R. (2012a) Nucleosynthetic tungsten isotope anomalies in acid leachates of the Murchison chondrite: Implications for hafnium-tungsten chronometry. *Astrophys. J.* **753,** L6.

Burkhardt C., Kleine T., Dauphas N. and Wieler R. (2012b) Origin of isotopic heterogeneity in the solar nebula by thermal processing and mixing of nebular dust. *Earth Planet. Sci. Lett.* **357-358,** 298-307.

Burkhardt C. and Schönbächler M. (2015) Intrinsic W nucleosynthetic isotope variations in carbonaceous chondrites: Implications for W nucleosynthesis and nebular vs. parent body processing of presolar materials. *Geochim. Cosmochim. Acta* **165,** 361-375.

Connelly J. N., Bizzarro M., Krot A. N., Nordlund Å, Wielandt D. and Ivanova M. A. (2012) The Absolute Chronology and Thermal Processing of Solids in the Solar Protoplanetary Disk. *Science* **338,** 651-655.

Connolly H. C.,Jr., Huss G. R. and Wasserburg G. J. (2001) On the formation of Fe-Ni metal in Renazzo-like carbonaceous chondrites. *Geochim. Cosmochim. Acta* **65,** 4567-4588.

Cook D. L. and Schönbächler M. (2016) High-precision measurement of W isotopes in Fe–Ni alloy and the effects from the nuclear field shift. *J. Anal. At. Spectrom.* **31,** 1400-1405.

Dauphas N., Marty B. and Reisberg L. (2002) Molybdenum Evidence for Inherited Planetary Scale Isotope Heterogeneity of the Protosolar Nebula. *Astrophys. J.* **565,** 640-644.

Desch S. J., Ciesla F. J., Hood L. L. and Nakamoto T. (2005) Heating of Chondritic Materials in Solar Nebula Shocks. In *Chondrites and the Protoplanetary Disk* (eds. A. N. Krot, E. R. D. Scott and B. Reipurth). Astronomical Society of the Pacific, San Francisco. pp. 849-872.

Ebel D. S., Brunner C., Konrad K., Leftwich K., Erb I., Lu M., Rodriguez H., Crapster-Pregont E. J., Friedrich J. M. and Weisberg M. K. (2016) Abundance, major element composition and size of components and matrix in CV, CO and Acfer 094 chondrites. *Geochim. Cosmochim. Acta* **172,** 322-356.

Füri E. and Marty B. (2015) Nitrogen isotope variations in the Solar System. *Nat. Geosci.* **8,** 515-522.

Gerber S., Burkhardt C., Budde G., Metzler K. and Kleine T. (2017) Mixing and Transport of Dust in the Early Solar Nebula as Inferred from Titanium Isotope Variations among Chondrules. *Astrophys. J.* **841,** L17.

Goldberg A. Z., Owen J. E. and Jacquet E. (2015) Chondrule transport in protoplanetary discs. *Mon. Not. R. Astron. Soc.* **452,** 4054-4069.

Goldmann A., Brennecka G., Noordmann J., Weyer S. and Wadhwa M. (2015) The uranium isotopic composition of the Earth and the Solar System. *Geochim. Cosmochim. Acta* **148,** 145-158.

Harju E. R., Rubin A. E., Ahn I., Choi B. G., Ziegler K. and Wasson J. T. (2014) Progressive aqueous alteration of CR carbonaceous chondrites. *Geochim. Cosmochim. Acta* **139,** 267-292.

Hezel D. C. and Palme H. (2008) Constraints for chondrule formation from Ca–Al distribution in carbonaceous chondrites. *Earth Planet. Sci. Lett.* **265,** 716-725.

Hoppe P. and Ott U. (1997) Mainstream silicon carbide grains from meteorites. *AIP Conf. Proc.* **402,** 27-58.

Hutcheon I. D., Marhas K. K., Krot A. N., Goswami J. N. and Jones R. H. (2009) ^{26}Al in plagioclase-rich chondrules in carbonaceous chondrites: Evidence for an extended duration of chondrule formation. *Geochim. Cosmochim. Acta* **73,** 5080-5099.

Jacobsen B., Yin Q. Z., Moynier F., Amelin Y., Krot A. N., Nagashima K., Hutcheon I. D. and Palme H. (2008) ^{26}Al–^{26}Mg and ^{207}Pb–^{206}Pb systematics of Allende CAIs: Canonical solar initial ^{26}Al/^{27}Al ratio reinstated. *Earth Planet. Sci. Lett.* **272,** 353-364.

Jacquet E., Paulhiac-Pison M., Alard O., Kearsley A. T. and Gounelle M. (2013) Trace element geochemistry of CR chondrite metal. *Meteorit. Planet. Sci.* **48,** 1981-1999.

Jilly-Rehak C. E., Huss G. R. and Nagashima K. (2017) ^{53}Mn–^{53}Cr radiometric dating of secondary carbonates in CR chondrites: Timescales for parent body aqueous alteration. *Geochim. Cosmochim. Acta* **201,** 224-244.

Johnson B. C., Walsh K. J., Minton D. A., Krot A. N. and Levison H. F. (2016) Timing of the formation and migration of giant planets as constrained by CB chondrites. *Sci. Adv.* **2,** e1601658.

Kleine T., Mezger K., Münker C., Palme H. and Bischoff A. (2004) ^{182}Hf-^{182}W isotope systematics of chondrites, eucrites, and martian meteorites: Chronology of core formation and early mantle differentiation in Vesta and Mars. *Geochim. Cosmochim. Acta* **68,** 2935-2946.

Kleine T., Mezger K., Palme H., Scherer E. and Münker C. (2005) Early core formation in asteroids and late accretion of chondrite parent bodies: Evidence from ^{182}Hf-^{182}W in CAIs, metal-rich chondrites, and iron meteorites. *Geochim. Cosmochim. Acta* **69,** 5805-5818.

Kleine T., Touboul M., Van Orman J. A., Bourdon B., Maden C., Mezger K. and Halliday A. N. (2008) Hf–W thermochronometry: Closure temperature and constraints on the accretion and cooling history of the H chondrite parent body. *Earth Planet. Sci. Lett.* **270,** 106-118.

Kleine T., Touboul M., Bourdon B., Nimmo F., Mezger K., Palme H., Jacobsen S. B., Yin Q. Z. and Halliday A. N. (2009) Hf–W chronology of the accretion and early evolution of asteroids and terrestrial planets. *Geochim. Cosmochim. Acta* **73,** 5150-5188.

Kleine T., Hans U., Irving A. J. and Bourdon B. (2012) Chronology of the angrite parent body and implications for core formation in protoplanets. *Geochim. Cosmochim. Acta* **84,** 186-203.

Kong P., Ebihara M. and Palme H. (1999) Distribution of siderophile elements in CR chondrites: Evidence for evaporation and recondensation during chondrule formation. *Geochim. Cosmochim. Acta* **63,** 2637-2652.

Kong P. and Palme H. (1999) Compositional and genetic relationship between chondrules, chondrule rims, metal, and matrix in the Renazzo chondrite. *Geochim. Cosmochim. Acta* **63,** 3673-3682.

Kretke K. A., Levison H. F. and Bottke W. (2016) Exploring How Giant Planet Formation Affected the Asteroid Belt. *Am. Astron. Soc. DPS Meet.* #518.03 (abstr.).

Krot A. N., Meibom A., Weisberg M. K. and Keil K. (2002) The CR chondrite clan: Implications for early solar system processes. *Meteorit. Planet. Sci.* **37,** 1451-1490.

Krot A. N., Amelin Y., Cassen P. and Meibom A. (2005) Young chondrules in CB chondrites from a giant impact in the early Solar System. *Nature* **436,** 989-992.

Krot A. N., Makide K., Nagashima K., Huss G. R., Ogliore R. C., Ciesla F. J., Yang L., Hellebrand E. and Gaidos E. (2012) Heterogeneous distribution of ^{26}Al at the birth of the solar system: Evidence from refractory grains and inclusions. *Meteorit. Planet. Sci.* **47,** 1948-1979.

Kruijer T. S., Sprung P., Kleine T., Leya I., Burkhardt C. and Wieler R. (2012) Hf–W chronometry of core formation in planetesimals inferred from weakly irradiated iron meteorites. *Geochim. Cosmochim. Acta* **99,** 287-304.

Kruijer T. S., Kleine T., Fischer-Gödde M., Burkhardt C. and Wieler R. (2014a) Nucleosynthetic W isotope anomalies and the Hf–W chronometry of Ca–Al-rich inclusions. *Earth Planet. Sci. Lett.* **403,** 317-327.

Kruijer T. S., Touboul M., Fischer-Gödde M., Bermingham K. R., Walker R. J. and Kleine T. (2014b) Protracted core formation and rapid accretion of protoplanets. *Science* **344,** 1150-1154.

Kruijer T. S., Burkhardt C., Budde G. and Kleine T. (2017) Age of Jupiter inferred from the distinct genetics and formation times of meteorites. *Proc. Natl. Acad. Sci. USA* **114,** 6712-6716.

Kurahashi E., Kita N. T., Nagahara H. and Morishita Y. (2008) ^{26}Al–^{26}Mg systematics of chondrules in a primitive CO chondrite. *Geochim. Cosmochim. Acta* **72,** 3865-3882.

Larsen K. K., Trinquier A., Paton C., Schiller M., Wielandt D., Ivanova M. A., Connelly J. N., Nordlund Å, Krot A. N. and Bizzarro M. (2011) Evidence For Magnesium Isotope Heterogeneity In The Solar Protoplanetary Disk. *Astrophys. J.* **735,** L37.

Leitner J., Vollmer C., Floss C., Zipfel J. and Hoppe P. (2016) Ancient stardust in fine-grained chondrule dust rims from carbonaceous chondrites. *Earth Planet. Sci. Lett.* **434,** 117-128.

Liu M. C., Chaussidon M., Göpel C. and Lee T. (2012) A heterogeneous solar nebula as sampled by CM hibonite grains. *Earth Planet. Sci. Lett.* **327-328,** 75-83.

Ludwig K. R. (2012) *User's Manual for Isoplot – A Geochronological Toolkit for Microsoft Excel.* Berkeley Geochronology Center, Special Publication No. 5.

MacPherson G. J., Kita N. T., Ushikubo T., Bullock E. S. and Davis A. M. (2012) Well-resolved variations in the formation ages for Ca–Al-rich inclusions in the early Solar System. *Earth Planet. Sci. Lett.* **331-332,** 43-54.

Makide K., Nagashima K., Krot A. N., Huss G. R., Ciesla F. J., Hellebrand E., Gaidos E. and Yang L. (2011) Heterogeneous distribution of ^{26}Al at the birth of the solar system. *Astrophys. J.* **733,** L31.

Morris M. A., Boley A. C., Desch S. J. and Athanassiadou T. (2012) Chondrule formation in bow shocks around eccentric planetary embryos. *Astrophys. J.* **752,** 27.

Nagashima K., Krot A. N. and Huss G. R. (2014) ^{26}Al in chondrules from CR2 chondrites. *Geochem. J.* **48,** 561-570.

Nagashima K., Krot A. N. and Komatsu M. (2017) ^{26}Al–^{26}Mg systematics in chondrules from Kaba and Yamato 980145 CV3 carbonaceous chondrites. *Geochim. Cosmochim. Acta* **201,** 303-319.

Nicolussi G. K., Pellin M. J., Lewis R. S., Davis A. M., Amari S. and Clayton R. N. (1998) Molybdenum isotopic composition of individual presolar silicon carbide grains from the Murchison meteorite. *Geochim. Cosmochim. Acta* **62,** 1093-1104.

Nishiizumi K. (2004) Preparation of ^{26}Al AMS standards. *Nucl. Instrum. Methods* **223-224,** 388-392.

Nyquist L. E., Kleine T., Shih C. Y. and Reese Y. D. (2009) The distribution of short-lived radioisotopes in the early solar system and the chronology of asteroid accretion, differentiation, and secondary mineralization. *Geochim. Cosmochim. Acta* **73,** 5115-5136.

Olsen M. B., Wielandt D., Schiller M., Van Kooten E. M. M. E. and Bizzarro M. (2016) Magnesium and ^{54}Cr isotope compositions of carbonaceous chondrite chondrules – Insights into early disk processes. *Geochim. Cosmochim. Acta* **191,** 118-138.

Palme H., Spettel B. and Hezel D. (2014) Siderophile elements in chondrules of CV chondrites. *Chem. Erde* **74,** 507-516.

Palme H., Hezel D. C. and Ebel D. S. (2015) The origin of chondrules: Constraints from matrix composition and matrix-chondrule complementarity. *Earth Planet. Sci. Lett.* **411,** 11-19.

Park C., Nagashima K., Krot A. N., Huss G. R., Davis A. M. and Bizzarro M. (2017) Calcium-aluminum-rich inclusions with fractionation and unidentified nuclear effects (FUN CAIs): II. Heterogeneities of magnesium isotopes and 26Al in the early Solar System inferred from in situ high-precision magnesium-isotope measurements. *Geochim. Cosmochim. Acta* **201,** 6-24.

Prombo C. A. and Clayton R. N. (1993) Nitrogen isotopic compositions of iron meteorites. *Geochim. Cosmochim. Acta* **57,** 3749-3761.

Qin L., Dauphas N., Wadhwa M., Markowski A., Gallino R., Janney P. E. and Bouman C. (2008) Tungsten Nuclear Anomalies in Planetesimal Cores. *Astrophys. J.* **674,** 1234-1241.

Rudraswami N. G. and Goswami J. N. (2007) ^{26}Al in chondrules from unequilibrated L chondrites: Onset and duration of chondrule formation in the early solar system. *Earth Planet. Sci. Lett.* **257,** 231-244.

Schiller M., Baker J. A. and Bizzarro M. (2010) ^{26}Al–^{26}Mg dating of asteroidal magmatism in the young Solar System. *Geochim. Cosmochim. Acta* **74,** 4844-4864.

Schiller M., Connelly J. N., Glad A. C., Mikouchi T. and Bizzarro M. (2015) Early accretion of protoplanets inferred from a reduced inner solar system ^{26}Al inventory. *Earth Planet. Sci. Lett.* **420,** 45-54.

Schrader D. L., Franchi I. A., Connolly H. C.,Jr., Greenwood R. C., Lauretta D. S. and Gibson J. M. (2011) The formation and alteration of the Renazzo-like carbonaceous chondrites I: Implications of bulk-oxygen isotopic composition. *Geochim. Cosmochim. Acta* **75,** 308-325.

Schrader D. L., Nagashima K., Krot A. N., Ogliore R. C., Yin Q. Z., Amelin Y., Stirling C. H. and Kaltenbach A. (2017) Distribution of ^{26}Al in the CR chondrite chondrule-forming region of the protoplanetary disk. *Geochim. Cosmochim. Acta* **201,** 275-302.

Spivak-Birndorf L., Wadhwa M. and Janney P. (2009) ^{26}Al–26Mg systematics in D'Orbigny and Sahara 99555 angrites: Implications for high-resolution chronology using extinct chronometers. *Geochim. Cosmochim. Acta* **73,** 5202-5211.

Sugiura N. and Fujiya W. (2014) Correlated accretion ages and ε^{54}Cr of meteorite parent bodies and the evolution of the solar nebula. *Meteorit. Planet. Sci.* **49,** 772-787.

Ushikubo T., Nagashima K., Kimura M., Tenner T. J. and Kita N. T. (2013) Contemporaneous formation of chondrules in distinct oxygen isotope reservoirs. *Geochim. Cosmochim. Acta* **109,** 280-295.

Van Kooten E. M. M. E., Wielandt D., Schiller M., Nagashima K., Thomen A., Larsen K. K., Olsen M. B., Nordlund Å, Krot A. N. and Bizzarro M. (2016) Isotopic evidence for primordial molecular cloud material in metal-rich carbonaceous chondrites. *Proc. Natl. Acad. Sci. USA* **113,** 2011-2016.

Villeneuve J., Chaussidon M. and Liboure G. (2009) Homogeneous Distribution of ^{26}Al in the Solar System from the Mg Isotopic Composition of Chondrules. *Science* **325,** 985-988.

Vockenhuber C., Oberli F., Bichler M., Ahmad I., Quitté G., Meier M., Halliday A. N., Lee D. C., Kutschera W., Steier P., Gehrke R. J. and Helmer R. G. (2004) New Half-Life Measurement of ^{182}Hf: Improved Chronometer for the Early Solar System. *Phys. Rev. Lett.* **93,** 172501.

Walsh K. J., Morbidelli A., Raymond S. N., O'Brien D. P. and Mandell A. M. (2011) A low mass for Mars from Jupiter's early gas-driven migration. *Nature* **475,** 206-209.

Wasserburg G. J., Lee T. and Papanastassiou D. A. (1977) Correlated O and Mg isotopic anomalies in Allende Inclusions: II. Magnesium. *Geophys. Res. Lett.* **4,** 299-302.

Weisberg M. K., Prinz M., Clayton R. N. and Mayeda T. K. (1993) The CR (Renazzo-type) carbonaceous chondrite group and its implications. *Geochim. Cosmochim. Acta* **57,** 1567-1586.

Willbold M., Elliott T. and Moorbath S. (2011) The tungsten isotopic composition of the Earth's mantle before the terminal bombardment. *Nature* **477,** 195-198.

Yokoyama T., Rai V. K., Alexander C. M. O. D., Lewis R. S., Carlson R. W., Shirey S. B., Thiemens M. H. and Walker R. J. (2007) Osmium isotope evidence for uniform distribution of s- and r-process components in the early solar system. *Earth Planet. Sci. Lett.* **259,** 567-580.

Figures captions and Tables

Fig. 1. The analyzed CR chondrite samples show variable excesses in ε^{183}W, which are consistent with a deficit in *s*-process (or an excess in *r*-process) W nuclides. The 'mixed' fractions (magnetic separates) are ordered by their W concentrations. Vertical lines represent the mean value (± 2 s.d.) of each sample type. Open symbols are GRA 06100 samples (these were mostly excluded from calculation of the mean values).

Fig. 2. Molybdenum isotope patterns of selected CR chondrite samples. CR metal shows a smaller *s*-deficit than bulk CR chondrites, whereas the silicate has a much larger *s*-deficit. Shown here are only the least-magnetic fractions (MS-4, MS-5), which most closely represent the composition of CR silicate. The gray area represents the external reproducibility (2 s.d.) of the Mo isotope measurements, defined by repeated analyses of BHVO-2 (Table S3).

Fig. 3. Diagram of ε^{183}W versus ε^{92}Mo demonstrating that nucleosynthetic W and Mo isotope anomalies in CR chondrite samples are broadly correlated. Therefore, these anomalies probably have a common origin and, hence, most likely reflect the heterogeneous distribution of the same presolar *s*-process carrier (Section 4.1).

Fig. 4. Diagrams of ε^{i}Mo versus ε^{92}Mo for the CR chondrite samples (normalized to ^{98}Mo/^{96}Mo). Note that Mo isotope data for bulk NWA 801 (larger error bars) are from Burkhardt et al. (2011). Dashed lines are mixing lines between terrestrial Mo and *s*- or *r*-process Mo, calculated using the *s*-process composition as measured in mainstream SiC grains (Nicolussi et al., 1998) and corresponding *r*-process residuals. Solid lines indicate the regressions calculated by *Isoplot* for the CR samples, where the uncertainties on the slopes and intercepts are 95% confidence intervals (95% CI). Note that the obtained CR correlation lines are in excellent agreement with those defined by carbonaceous chondrite data, including chondrule and matrix separates, acid leachates, as well as bulk meteorites (see Budde et al., 2016a, for details).

Fig. 5. Diagram of ε^{95}Mo versus ε^{94}Mo. All CR chondrite samples plot on a well-defined correlation line, whose slope is consistent with the predicted slope for *s*-process variability. Moreover, the regression of the CR chondrite data yields a non-terrestrial intercept that is in agreement with Mo isotope data obtained for other carbonaceous chondrites. This *s*-mixing line defined by carbonaceous chondrite samples was termed the 'CC-line', where ε^{95}Mo = (0.596±0.006) × ε^{94}Mo + (0.29±0.03). Note that all CR components plot exactly on this CC-line (see Fig. 4 and Budde et al., 2016a, for details).

Fig. 6. Isochron diagrams for the investigated CR chondrites, where the individual isochrons are indistinguishable within their uncertainties. The ε^{182}W values are normalized to ^{186}W/^{183}W ('6/3') and corrected for a small effect of nucleosynthetic anomalies (see Section 5.1 and supplementary material for details). Uncertainties on

$^{182}Hf/^{180}Hf_i$ and $\varepsilon^{182}W_i$ are 95% confidence intervals (95% CI). i = initial, Δt_{CAI} = age relative to CAI formation, MSWD = mean square of weighted deviates, n = number of samples included in isochron regression.

Fig. 7. (a) Combined CR isochron including all analyzed samples from NWA 801, Acfer 097, NWA 1180, and GRA 06100 (see Fig. 6), defining an age of 3.6±0.6 Ma after CAI formation. (b) Isochron diagram including only chondrule metal and chondrule silicate fractions from the investigated CR chondrites. This isochron regression is in excellent agreement with that of the combined isochron, showing that the latter dates chondrule formation.

Fig. 8. Comparison of Pb-Pb, Al-Mg, and Hf-W ages for CR chondrules, which are in excellent agreement. The Al-Mg age represents the preferred chondrule age determined by Schrader et al. (2017) and is based on the weighted mean of 21 chondrules (Section 5.3). The Pb-Pb age was obtained for a set of six CR chondrules and U-corrected using $^{238}U/^{235}U$ = 137.779±0.009 (Schrader et al., 2017). The vertical line indicates the weighted average [3.73±0.21 Ma (2σ)] defined by the three ages.

Fig. 9. Initial $^{26}Al/^{27}Al$ versus $^{182}Hf/^{180}Hf$ measured for CV CAIs, CV chondrules, CR chondrules, and angrites (on logarithmic scales), which cover the entire effective lifetime of ^{26}Al. All samples plot on a single, well-defined correlation line, which has a slope that is in very good agreement with the slope expected from the ratio of the ^{26}Al and ^{182}Hf decay constants (12.6±0.4). The regression was calculated using the 'Model 1' fit of *Isoplot*. Given uncertainties and the shown error envelope (in gray) represent 95% confidence intervals (95% CI); uncertainties in parentheses are 2σ ('observed scatter') errors (see Section 6 for details). Data sources and values are provided in Table 3.

Fig. 10. Maximum heterogeneity of initial $^{26}Al/^{27}Al$ as function of time. Curved lines represent the *y*-axis difference between the ^{26}Al–^{182}Hf correlation line and the (95% CI or 2σ) error envelope at a given point in time (Fig. 9). Values based on 95% confidence intervals (solid black lines) range from about ±20% at the time of angrite and CR chondrule formation (~4–5 Ma) to $^{+61\%}/_{-36\%}$ at the time of CAI formation. Values based on 2σ ('observed scatter') errors (dashed gray lines) are below about ±10% at any point in time after ~1.6 Ma and about ±15% at the time of CAI formation. These results are inconsistent with the range of ^{26}Al deficits (at the time of CAI formation; relative to the 'canonical' $^{26}Al/^{27}Al$) proposed for the precursor material of parent bodies of angrites, ureilites, OC, EC, and CI chondrites (46–79%; red bar) (Larsen et al., 2011; Schiller et al., 2015), and individual CV and CR chondrules (58–97%; orange bar) (Olsen et al., 2016). Data points represent Al-Mg ages of the samples (*x*-axis) and the offset from the best-fit line in Fig. 9 (*y*-axis); vertical error bars represent relative uncertainties on the $(^{26}Al/^{27}Al)_i$ of the respective sample.

Table 1. Hf-W isotope data for CR chondrite samples.

Sample	Grain size (µm)	Weight (mg)	Hf (ng/g)	W (ng/g)	$^{180}Hf/^{184}W$ (± 2σ)	N (W-IC)	$\varepsilon^{182}W_{meas.}$ (± 2σ)	$\varepsilon^{183}W$ (± 2σ)	$\varepsilon^{182}W_i$ (± 2σ)	$\varepsilon^{182}W_{nuc.\ corr.}$ (± 2σ)	$\varepsilon^{182}W_{meas.}$ (± 2σ)	$\varepsilon^{184}W$ (± 2σ)	$\varepsilon^{182}W_i$ (± 2σ)	$\varepsilon^{182}W_{nuc.\ corr.}$ (± 2σ)
							normalized to $^{186}W/^{184}W$ = 0.92767 ('6/4')				normalized to $^{186}W/^{183}W$ = 1.98590 ('6/3')			
NWA 801														
WR	–	556	184	142	1.533 ± 0.011	2	-1.08 ± 0.14	0.49 ± 0.16	-2.44 ± 0.14	-1.69 ± 0.24	-1.74 ± 0.22	-0.32 ± 0.11	-3.10 ± 0.22	-1.70 ± 0.22
M1	>500	317	9.4	468	0.024 ± 0.001	5	-2.98 ± 0.07	0.16 ± 0.13	-3.00 ± 0.07	-3.17 ± 0.18	-3.20 ± 0.20	-0.10 ± 0.09	-3.22 ± 0.20	-3.19 ± 0.20
M2	125-500	227	9.0	568	0.019 ± 0.001	5	-2.91 ± 0.07	0.23 ± 0.13	-2.93 ± 0.07	-3.20 ± 0.18	-3.17 ± 0.18	-0.15 ± 0.08	-3.19 ± 0.18	-3.16 ± 0.18
MS-1	40-125	488	90	286	0.371 ± 0.001	4	-2.05 ± 0.14	0.56 ± 0.17	-2.38 ± 0.14	-2.74 ± 0.25	-2.79 ± 0.27	-0.37 ± 0.11	-3.12 ± 0.27	-2.75 ± 0.27
MS-2	40-125	506	128	195	0.775 ± 0.002	3	-1.41 ± 0.14	0.70 ± 0.16	-2.10 ± 0.14	-2.29 ± 0.25	-2.35 ± 0.22	-0.47 ± 0.11	-3.04 ± 0.22	-2.29 ± 0.22
MS-3	40-125	506	165	116	1.684 ± 0.008	2	-0.20 ± 0.14	1.00 ± 0.16	-1.69 ± 0.14	-1.45 ± 0.25	-1.54 ± 0.22	-0.67 ± 0.11	-3.04 ± 0.22	-1.47 ± 0.23
MS-4	40-125	538	206	71	3.421 ± 0.029	1	1.09 ± 0.14	0.67 ± 0.16	-1.94 ± 0.16	0.26 ± 0.25	0.20 ± 0.22	-0.44 ± 0.11	-2.84 ± 0.23	0.25 ± 0.22
MS-5	40-125	552	241	46	6.113 ± 0.030	1	3.06 ± 0.14	0.55 ± 0.16	-2.37 ± 0.19	2.37 ± 0.24	2.31 ± 0.22	-0.36 ± 0.11	-3.11 ± 0.25	2.36 ± 0.22
C-S	500-1600	543	272	73	4.380 ± 0.020	1	1.14 ± 0.14	0.38 ± 0.16	-2.75 ± 0.17	0.66 ± 0.24	0.63 ± 0.22	-0.25 ± 0.11	-3.26 ± 0.24	0.66 ± 0.22
C-M	>125	41	5.5	1109	0.006 ± 0.002	1	-2.97 ± 0.14	0.10 ± 0.16	-2.98 ± 0.14	-3.10 ± 0.24	-3.11 ± 0.22	-0.07 ± 0.11	-3.11 ± 0.22	-3.10 ± 0.22
Acfer 097														
M	>125	270	6.3	559	0.013 ± 0.001	5	-3.04 ± 0.04	0.13 ± 0.14	-3.06 ± 0.04	-3.21 ± 0.18	-3.21 ± 0.18	-0.09 ± 0.09	-3.22 ± 0.18	-3.20 ± 0.18
MS-1	40-125	502	98	262	0.442 ± 0.002	3	-2.08 ± 0.14	0.57 ± 0.16	-2.48 ± 0.14	-2.79 ± 0.25	-2.83 ± 0.22	-0.38 ± 0.11	-3.22 ± 0.22	-2.79 ± 0.22
MS-2	40-125	486	142	190	0.884 ± 0.002	3	-1.58 ± 0.14	0.56 ± 0.16	-2.37 ± 0.14	-2.29 ± 0.25	-2.35 ± 0.22	-0.37 ± 0.11	-3.13 ± 0.22	-2.31 ± 0.22
MS-3	40-125	503	168	109	1.824 ± 0.006	1	-0.52 ± 0.14	0.65 ± 0.16	-2.14 ± 0.14	-1.33 ± 0.25	-1.39 ± 0.22	-0.43 ± 0.11	-3.01 ± 0.22	-1.34 ± 0.22
MS-4	40-125	396	200	73	3.226 ± 0.024	1	0.31 ± 0.14	0.47 ± 0.16	-2.55 ± 0.16	-0.27 ± 0.24	-0.33 ± 0.22	-0.31 ± 0.11	-3.19 ± 0.23	-0.29 ± 0.22
MS-5	40-125	542	214	38	6.651 ± 0.036	1	3.54 ± 0.14	0.69 ± 0.16	-2.37 ± 0.19	2.67 ± 0.25	2.63 ± 0.22	-0.46 ± 0.11	-3.28 ± 0.26	2.68 ± 0.22
C-S	500-1600	428	214	58	4.363 ± 0.017	1	1.60 ± 0.14	0.70 ± 0.16	-2.28 ± 0.17	0.73 ± 0.25	0.65 ± 0.22	-0.46 ± 0.11	-3.22 ± 0.24	0.71 ± 0.22
C-M	>125	82	9.4	555	0.020 ± 0.004	1	-2.87 ± 0.14	0.18 ± 0.16	-2.89 ± 0.14	-3.09 ± 0.24	-3.08 ± 0.22	-0.12 ± 0.11	-3.09 ± 0.22	-3.06 ± 0.22
NWA 1180														
WR	–	498	147	129	1.339 ± 0.012	1	-1.52 ± 0.14	0.31 ± 0.16	-2.71 ± 0.14	-1.91 ± 0.24	-1.94 ± 0.22	-0.20 ± 0.11	-3.13 ± 0.22	-1.92 ± 0.22
M	>125	308	3.0	577	0.006 ± 0.001	5	-3.00 ± 0.05	0.13 ± 0.13	-3.00 ± 0.05	-3.16 ± 0.16	-3.17 ± 0.18	-0.08 ± 0.08	-3.17 ± 0.18	-3.16 ± 0.18
MS-1	40-125	486	95	247	0.455 ± 0.001	4	-1.82 ± 0.14	0.70 ± 0.16	-2.22 ± 0.14	-2.70 ± 0.25	-2.76 ± 0.23	-0.47 ± 0.11	-3.17 ± 0.23	-2.71 ± 0.23
MS-2	40-125	507	132	155	1.008 ± 0.004	2	-1.47 ± 0.14	0.65 ± 0.16	-2.36 ± 0.14	-2.28 ± 0.25	-2.33 ± 0.22	-0.43 ± 0.11	-3.23 ± 0.22	-2.28 ± 0.22
MS-3	40-125	501	155	115	1.597 ± 0.005	1	-1.00 ± 0.14	0.53 ± 0.16	-2.41 ± 0.14	-1.65 ± 0.24	-1.69 ± 0.22	-0.35 ± 0.11	-3.10 ± 0.22	-1.65 ± 0.22
MS-4	40-125	521	195	84	2.751 ± 0.015	1	-0.14 ± 0.14	0.44 ± 0.16	-2.58 ± 0.15	-0.69 ± 0.24	-0.72 ± 0.22	-0.29 ± 0.11	-3.16 ± 0.23	-0.69 ± 0.22
MS-5	40-125	541	211	50	5.033 ± 0.024	1	1.89 ± 0.14	0.69 ± 0.16	-2.58 ± 0.17	1.03 ± 0.25	0.97 ± 0.22	-0.46 ± 0.11	-3.50 ± 0.24	1.02 ± 0.22
C-S	500-1600	518	218	87	2.951 ± 0.008	1	-0.01 ± 0.14	0.41 ± 0.16	-2.63 ± 0.15	-0.52 ± 0.24	-0.55 ± 0.22	-0.27 ± 0.11	-3.17 ± 0.23	-0.52 ± 0.22
C-M	–	41	4.9	630	0.009 ± 0.004	1	-3.02 ± 0.14	0.03 ± 0.16	-3.03 ± 0.14	-3.06 ± 0.25	-3.06 ± 0.22	-0.02 ± 0.11	-3.07 ± 0.22	-3.06 ± 0.22
GRA 06100														
WR	–	555	194	172	1.331 ± 0.004	3	-1.50 ± 0.14	0.35 ± 0.16	-2.68 ± 0.14	-1.93 ± 0.24	-1.96 ± 0.22	-0.23 ± 0.11	-3.14 ± 0.22	-1.94 ± 0.22
M1	>1000	70	0.7	449	0.002 ± 0.005	1	-2.94 ± 0.14	0.26 ± 0.16	-2.94 ± 0.14	-3.26 ± 0.24	-3.25 ± 0.22	-0.17 ± 0.11	-3.25 ± 0.22	-3.23 ± 0.22
M2	500-1000	53	0.4	431	0.001 ± 0.006	1	-2.87 ± 0.14	0.35 ± 0.16	-2.87 ± 0.14	-3.30 ± 0.25	-3.30 ± 0.22	-0.23 ± 0.11	-3.30 ± 0.22	-3.28 ± 0.22
M3	125-500	58	1.0	409	0.003 ± 0.006	1	-2.68 ± 0.14	0.30 ± 0.17	-2.69 ± 0.14	-3.06 ± 0.26	-3.06 ± 0.22	-0.20 ± 0.12	-3.06 ± 0.22	-3.03 ± 0.22
MS-1	40-125	502	101	192	0.620 ± 0.004	3	-1.54 ± 0.14	0.75 ± 0.16	-2.09 ± 0.14	-2.48 ± 0.25	-2.53 ± 0.22	-0.50 ± 0.11	-3.09 ± 0.22	-2.48 ± 0.22
MS-2	40-125	536	159	135	1.390 ± 0.006	2	-1.05 ± 0.14	0.64 ± 0.16	-2.28 ± 0.14	-1.85 ± 0.25	-1.91 ± 0.22	-0.43 ± 0.11	-3.15 ± 0.22	-1.86 ± 0.22
MS-3	40-125	507	156	140	1.315 ± 0.004	2	-2.44 ± 0.14	-0.26 ± 0.16	-3.61 ± 0.14	-2.12 ± 0.24	-2.09 ± 0.22	0.17 ± 0.11	-3.26 ± 0.22	-2.11 ± 0.22
MS-4	40-125	508	173	132	1.544 ± 0.010	2	-1.58 ± 0.14	0.12 ± 0.16	-2.95 ± 0.14	-1.73 ± 0.24	-1.73 ± 0.22	-0.08 ± 0.11	-3.10 ± 0.22	-1.72 ± 0.22
MS-5	40-125	533	197	67	3.494 ± 0.027	1	1.50 ± 0.14	1.09 ± 0.16	-1.60 ± 0.16	0.14 ± 0.25	0.05 ± 0.22	-0.72 ± 0.11	-3.05 ± 0.23	0.14 ± 0.23
C-S	500-1600	464	230	91	2.991 ± 0.009	1	0.96 ± 0.14	1.13 ± 0.16	-1.69 ± 0.15	-0.45 ± 0.25	-0.55 ± 0.22	-0.75 ± 0.11	-3.21 ± 0.23	-0.47 ± 0.23
C-M	–	30	6.2	413	0.018 ± 0.012	1	-2.71 ± 0.19	0.54 ± 0.22	-2.72 ± 0.19	-3.38 ± 0.33	-3.43 ± 0.25	-0.36 ± 0.14	-3.45 ± 0.25	-3.39 ± 0.26

W isotope ratios involving ^{183}W were corrected for a small mass-independent effect (Section S1). Given uncertainties are based on the external reproducibility (2 s.d.) obtained from repeated analyses of the terrestrial standards (Tables S1 and S2) or the in-run error (2 s.e.), whichever is larger. For samples with N>3, the uncertainties represent 95% confidence intervals (95% CI). Note that the final uncertainties include all propagated uncertainties induced by the correction for a small mass-independent effect on ^{183}W as well as by the correction for ^{182}Hf decay ($\varepsilon^{182}W_i$) using $(^{182}Hf/^{180}Hf)_i = (7.68\pm0.17)\times10^{-5}$ or nucleosynthetic anomalies ($\varepsilon^{182}W_{nuc.\ corr.}$) after Budde et al. (2016b). N: number of analyses. WR: whole rock, M: metal, MS: magnetic separate ('mixed fractions'), C-S: chondrule silicate, C-M: chondrule metal.

Table 2. Mo isotope data for CR chondrite samples.

Sample	Mo [a] (ng/g)	Mo/W	N (Mo-IC)	ε^{92}Mo (± 2σ)	ε^{94}Mo (± 2σ)	ε^{95}Mo (± 2σ)	ε^{97}Mo (± 2σ)	ε^{100}Mo (± 2σ)
NWA 801								
WR [b]	1210	8.5	3	3.58 ± 0.64	2.82 ± 0.38	1.73 ± 0.32	0.87 ± 0.36	1.03 ± 0.11
M1	4148	8.9	–	–	–	–	–	–
M2	5152	9.1	7	1.80 ± 0.23	1.42 ± 0.12	1.07 ± 0.09	0.55 ± 0.04	0.61 ± 0.07
MS-1	2197	7.7	6	2.85 ± 0.26	2.22 ± 0.13	1.52 ± 0.16	0.79 ± 0.07	0.87 ± 0.14
MS-2	1452	7.5	–	–	–	–	–	–
MS-3	–	–	–	–	–	–	–	–
MS-4	599	8.4	2	8.40 ± 0.39	6.73 ± 0.25	4.18 ± 0.16	2.16 ± 0.16	2.87 ± 0.25
MS-5	414	8.9	2	10.55 ± 0.39	8.38 ± 0.25	5.35 ± 0.16	2.76 ± 0.16	3.25 ± 0.25
C-S	641	8.8	3	5.59 ± 0.39	4.37 ± 0.25	2.80 ± 0.16	1.42 ± 0.16	1.61 ± 0.25
C-M	10112	9.1	3	1.94 ± 0.39	1.36 ± 0.25	1.07 ± 0.16	0.52 ± 0.16	0.57 ± 0.25
Acfer 097								
M	4574	8.2	6	1.68 ± 0.14	1.28 ± 0.09	0.94 ± 0.08	0.49 ± 0.09	0.56 ± 0.12
MS-1	2255	8.6	–	–	–	–	–	–
MS-2	1565	8.3	5	2.55 ± 0.28	1.92 ± 0.21	1.36 ± 0.12	0.73 ± 0.06	0.84 ± 0.15
MS-3	–	–	–	–	–	–	–	–
MS-4	567	7.8	–	–	–	–	–	–
MS-5	354	9.3	1	7.79 ± 0.39	6.19 ± 0.25	4.04 ± 0.16	2.10 ± 0.16	2.65 ± 0.25
C-S	575	9.9	2	2.96 ± 0.39	2.40 ± 0.25	1.56 ± 0.16	0.83 ± 0.16	0.80 ± 0.25
C-M	4522	8.2	3	1.95 ± 0.39	1.37 ± 0.25	1.11 ± 0.16	0.55 ± 0.16	0.51 ± 0.25
NWA 1180								
WR	–	–	–	–	–	–	–	–
M	4596	8.0	7	1.85 ± 0.09	1.42 ± 0.09	1.10 ± 0.08	0.55 ± 0.06	0.54 ± 0.10
MS-1	2113	8.5	6	3.65 ± 0.14	2.85 ± 0.12	1.84 ± 0.06	0.90 ± 0.12	0.97 ± 0.13
MS-2	1251	8.1	5	4.43 ± 0.22	3.52 ± 0.12	2.28 ± 0.11	1.16 ± 0.05	1.40 ± 0.09
MS-3	–	–	–	–	–	–	–	–
MS-4	692	8.3	3	9.25 ± 0.39	7.27 ± 0.25	4.59 ± 0.16	2.40 ± 0.16	2.84 ± 0.25
MS-5	423	8.5	–	–	–	–	–	–
C-S	644	7.4	–	–	–	–	–	–
C-M	5580	8.9	–	–	–	–	–	–
GRA 06100								
WR	1437	8.4	5	4.14 ± 0.12	3.11 ± 0.15	2.26 ± 0.04	1.18 ± 0.04	1.40 ± 0.17
M1	4632	10.3	–	–	–	–	–	–
M2	5040	11.7	–	–	–	–	–	–
M3	4971	12.1	–	–	–	–	–	–
MS-1	2378	12.4	–	–	–	–	–	–
MS-2	1129	8.4	–	–	–	–	–	–
MS-3	1063	7.6	4	-2.05 ± 0.18	-1.74 ± 0.23	-0.79 ± 0.04	-0.45 ± 0.01	-0.70 ± 0.08
MS-4	750	5.7	–	–	–	–	–	–
MS-5	293	4.4	1	10.16 ± 0.39	8.11 ± 0.25	5.09 ± 0.16	2.66 ± 0.16	3.33 ± 0.25
C-S	527	5.8	2	10.72 ± 0.39	8.67 ± 0.25	5.38 ± 0.16	2.86 ± 0.16	3.64 ± 0.25
C-M	7159	17.4	–	–	–	–	–	–

Mo isotope ratios are normalized to ^{98}Mo/^{96}Mo = 1.453173. Given uncertainties represent the external reproducibility (2 s.d.) obtained from repeated analyses of BHVO-2 (Table S3) or 95% confidence intervals (95% CI) for samples with N>3. N: number of analyses. WR: whole rock, M: metal, MS: magnetic separate ('mixed fractions'), C-S: chondrule silicate, C-M: chondrule metal.

[a] Mo concentrations as determined by quadrupole ICP-MS, which have an uncertainty of ~5%.

[b] Mo concentration and isotope data for bulk NWA 801 are from Burkhardt et al. (2011).

Table 3. Al-Mg and Hf-W data for different solar system materials.

Sample	$(^{26}Al/^{27}Al)_i$	Al-Mg age (Ma)	$(^{182}Hf/^{180}Hf)_i$	Hf-W age (Ma)	Reference
CV CAIs	$(5.23\pm0.13)\times10^{-5}$	0	$(1.018\pm0.043)\times10^{-4}$	0	1, 2
CV chondrules	$(4.84\pm0.88)\times10^{-6}$	2.43 ± 0.20	$(8.58\pm0.39)\times10^{-5}$	2.20 ± 0.80	3, 4
CR chondrules	$(1.33\pm0.29)\times10^{-6}$	3.75 ± 0.24	$(7.68\pm0.17)\times10^{-5}$	3.63 ± 0.62	5-6, 7
Angrites	$(3.99\pm0.19)\times10^{-7}$	4.98 ± 0.13	$(6.99\pm0.11)\times10^{-5}$	4.83 ± 0.59	8-10, 11

Ages are calculated relative to CV CAIs assuming a homogeneous distribution of ^{26}Al and ^{182}Hf (see also Fig. S6). Uncertainties on initial $^{26}Al/^{27}Al$ and $^{182}Hf/^{180}Hf$ are typically 95% confidence intervals (95% CI); uncertainties on the calculated ages are 2σ errors and include all propagated uncertainties. (1) Jacobsen et al. (2008), (2) Kruijer et al. (2014a), (3) Nagashima et al. (2017), (4) Budde et al. (2016b), (5) Nagashima et al. (2014), (6) Schrader et al. (2017), (7) this study, (8) Spivak-Birndorf et al. (2009), (9) Schiller et al. (2010), (10) Schiller et al. (2015), (11) Kleine et al. (2012). See Section 6 for details.

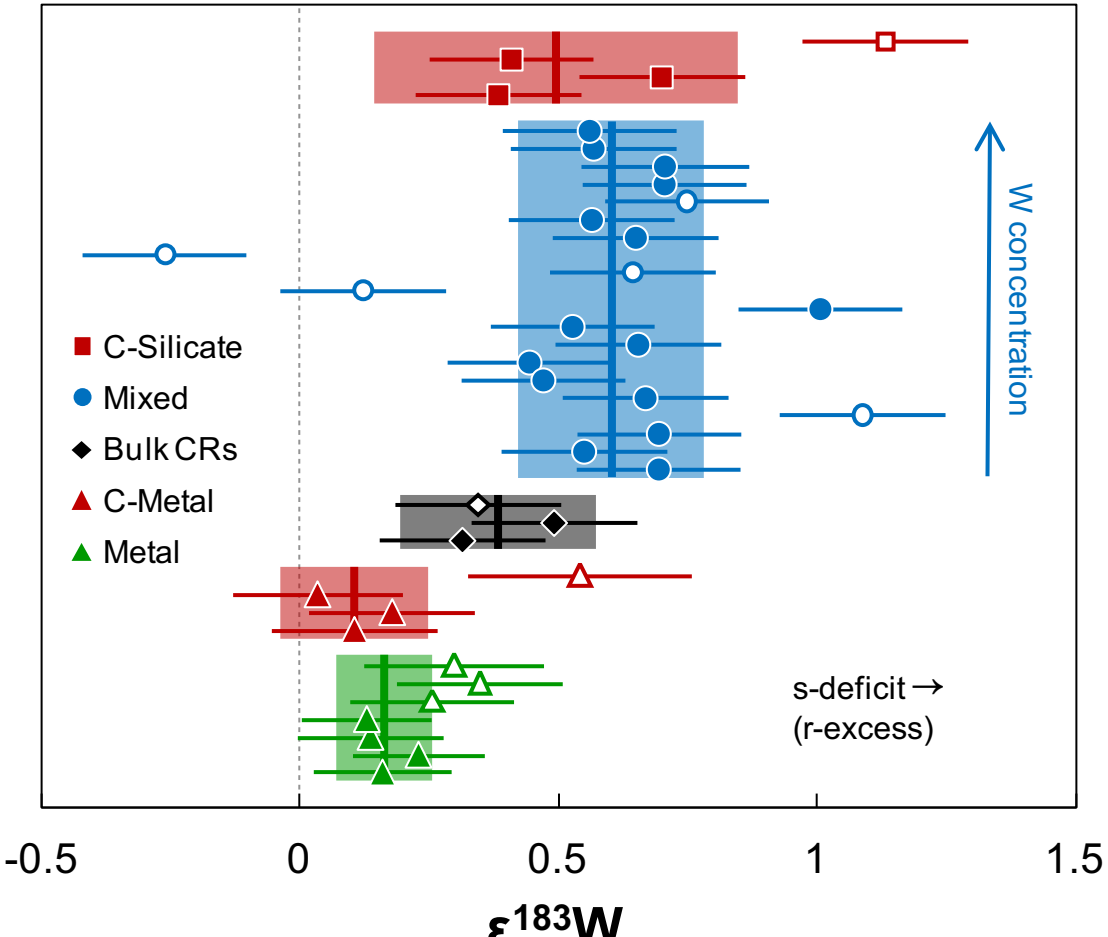
C-Silicate
Mixed
Bulk CRs
C-Metal
Metal
W concentration
s-deficit →
(r-excess)
-0.5
0
0.5
1
1.5
ε183W

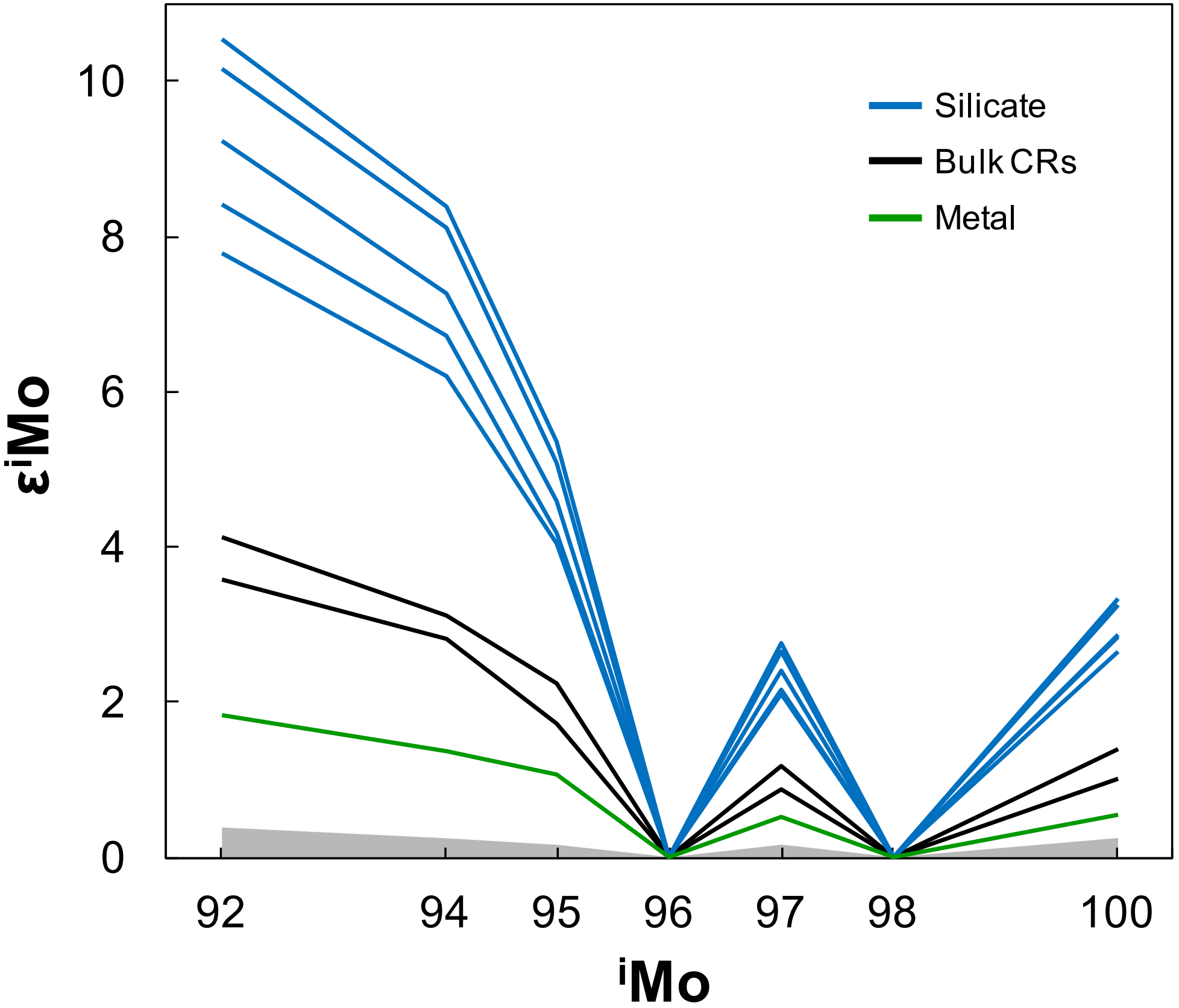
Silicate
Bulk CRs
Metal
10
8
6
4
2
0
ε^{i}Mo
92
94
95
96
97
98
100
^{i}Mo

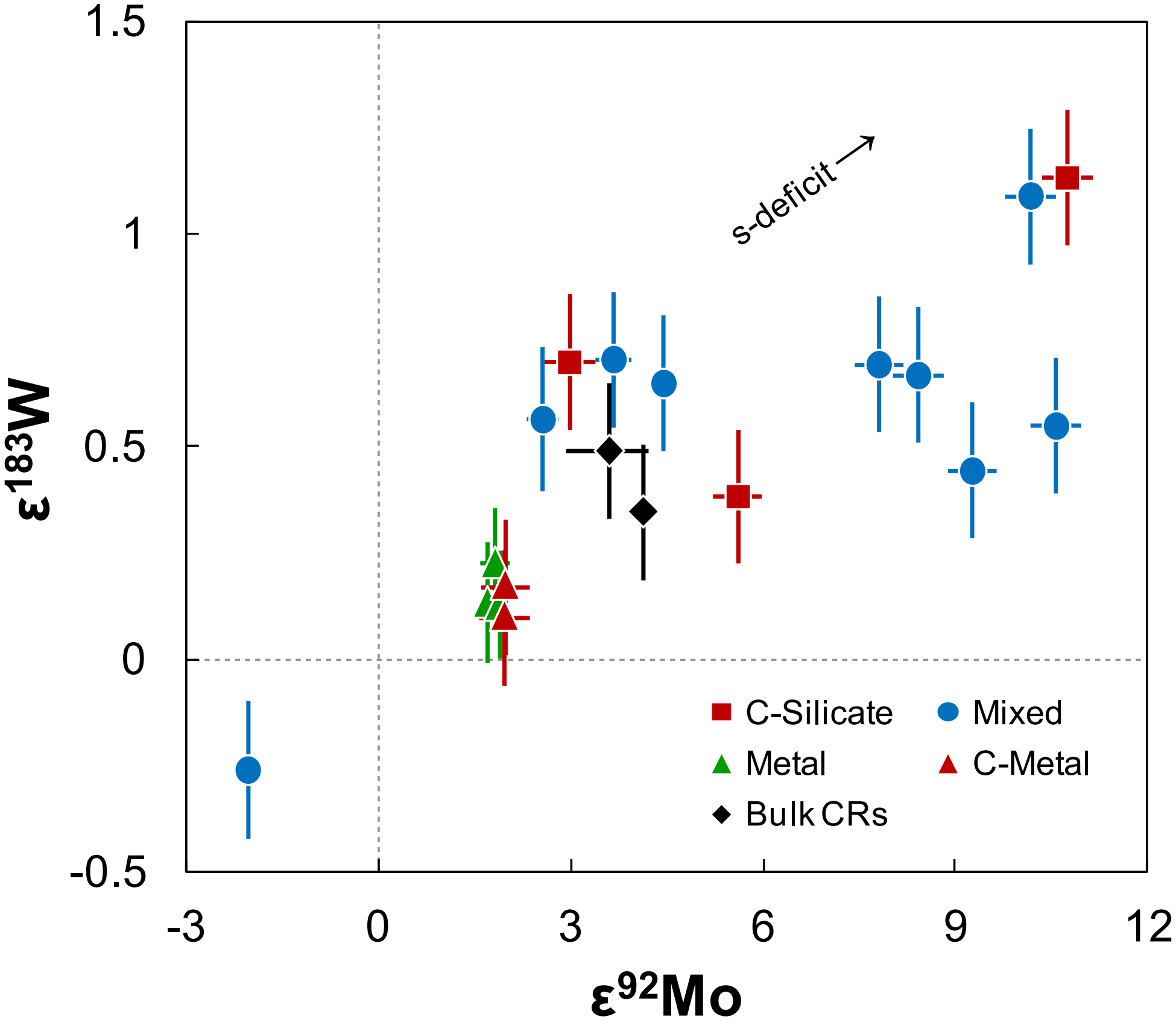
1.5
1
0.5
0
-0.5
-3
0
3
6
9
12
ε183W
ε92Mo
s-deficit
C-Silicate
Mixed
Metal
C-Metal
Bulk CRs

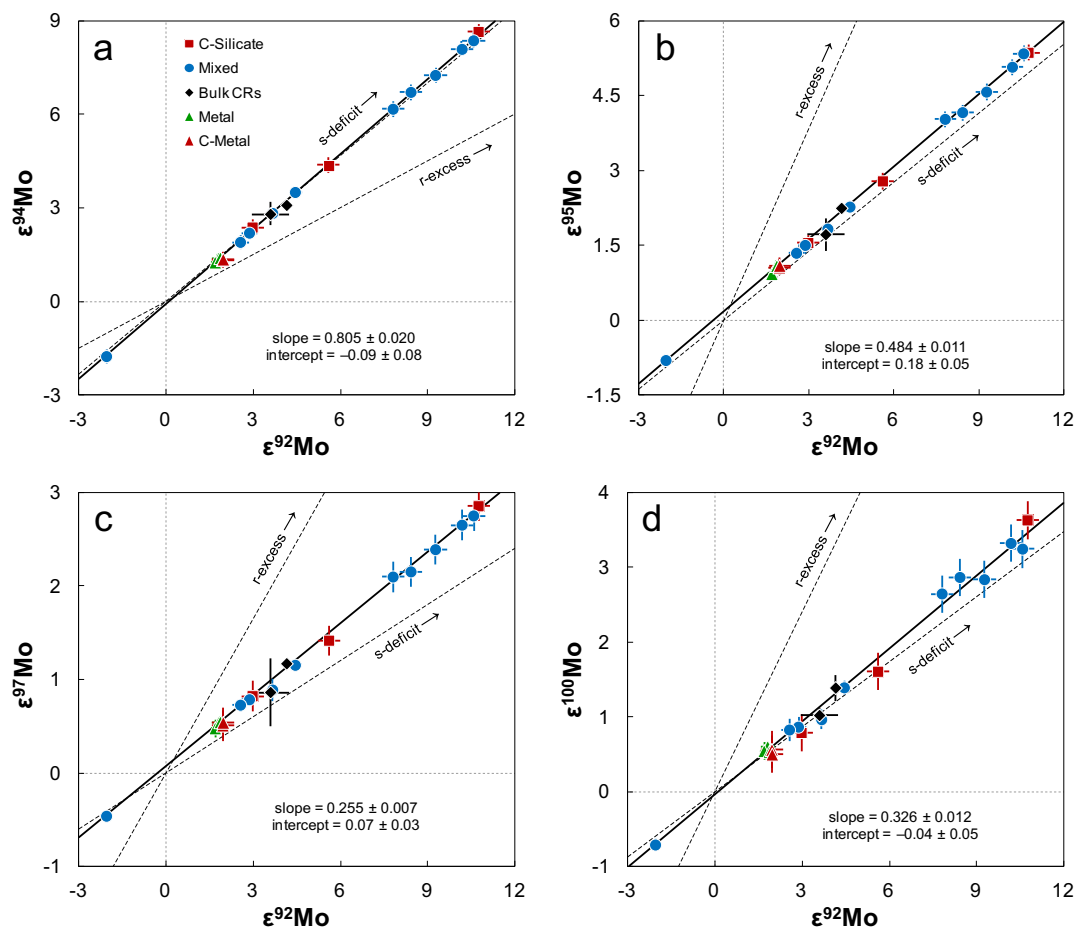
a
C-Silicate
Mixed
Bulk CRs
Metal
C-Metal
s-deficit
r-excess
slope = 0.805 ± 0.020
intercept = –0.09 ± 0.08
ε94Mo
ε92Mo
b
r-excess
s-deficit
slope = 0.484 ± 0.011
intercept = 0.18 ± 0.05
ε95Mo
ε92Mo
c
r-excess
s-deficit
slope = 0.255 ± 0.007
intercept = 0.07 ± 0.03
ε97Mo
ε92Mo
d
r-excess
s-deficit
slope = 0.326 ± 0.012
intercept = –0.04 ± 0.05
ε100Mo
ε92Mo

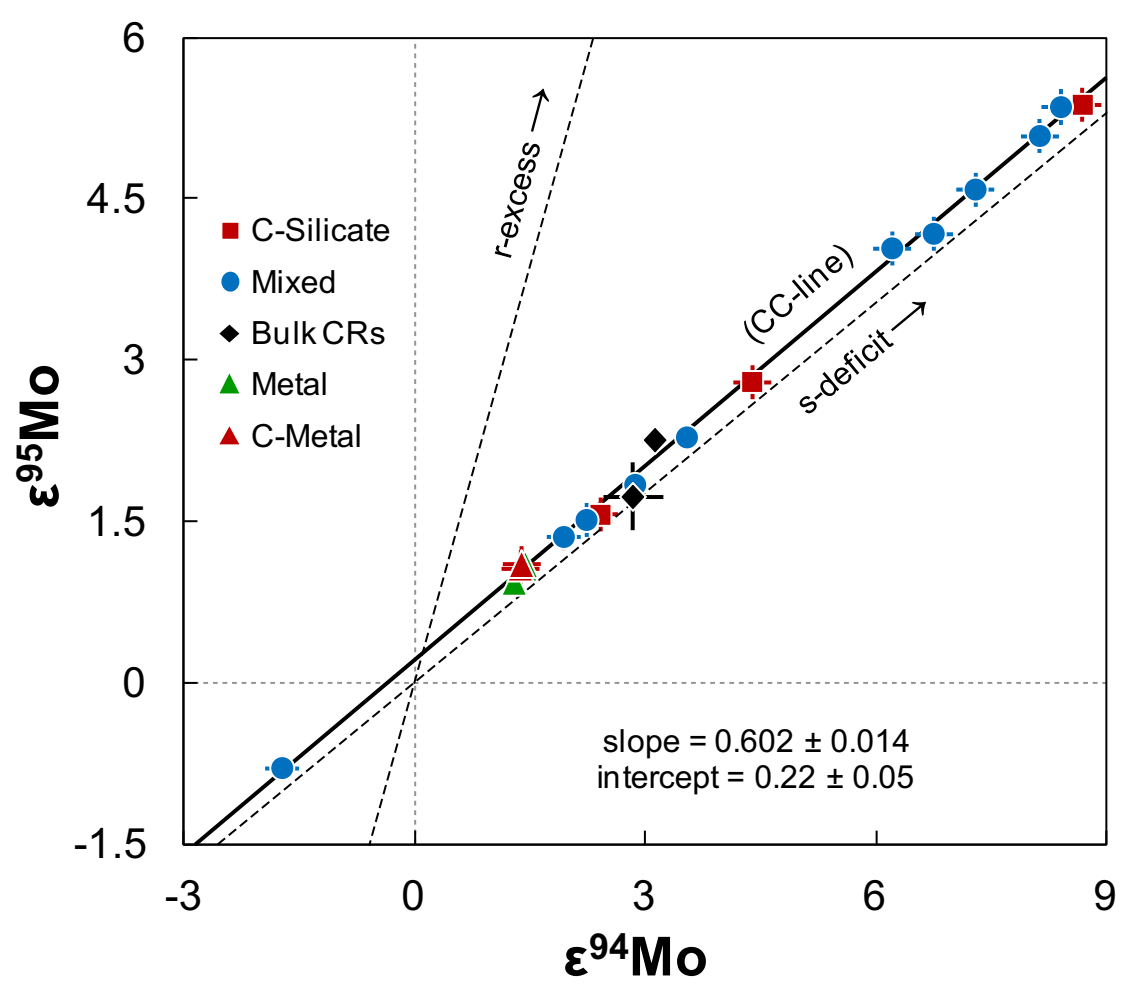
C-Silicate
Mixed
Bulk CRs
Metal
C-Metal
r-excess
(CC-line)
s-deficit
slope = 0.602 ± 0.014
intercept = 0.22 ± 0.05
ε95Mo
ε94Mo
6
4.5
3
1.5
0
-1.5
-3
0
3
6
9

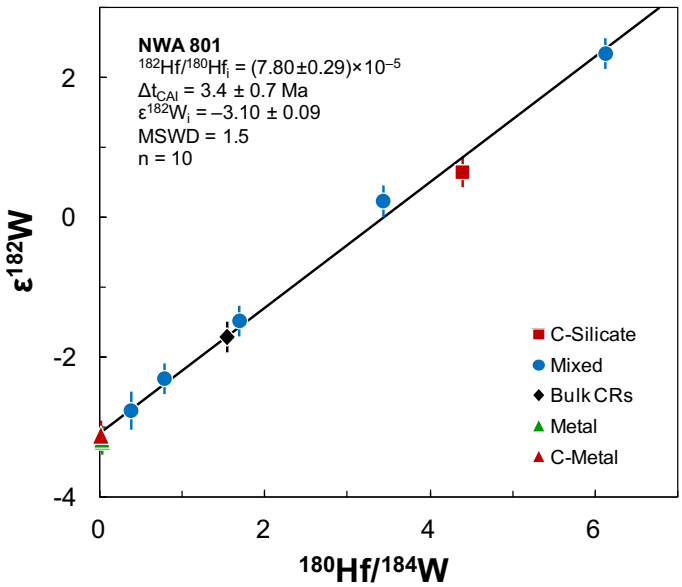
NWA 801
$^{182}Hf/^{180}Hf_i = (7.80 \pm 0.29) \times 10^{-5}$
Δt_{CAI} = 3.4 ± 0.7 Ma
$\varepsilon^{182}W_i$ = –3.10 ± 0.09
MSWD = 1.5
n = 10
C-Silicate
Mixed
Bulk CRs
Metal
C-Metal
$\varepsilon^{182}W$
$^{180}Hf/^{184}W$

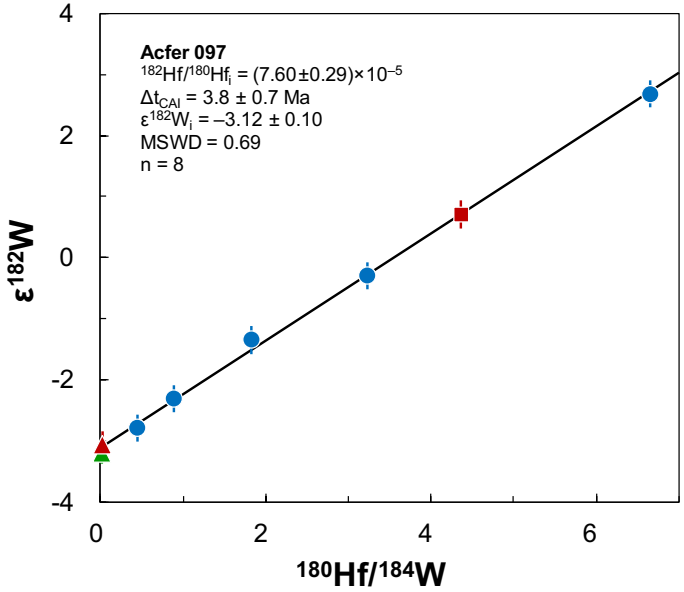
Acfer 097
$^{182}Hf/^{180}Hf_i = (7.60 \pm 0.29) \times 10^{-5}$
Δt_{CAI} = 3.8 ± 0.7 Ma
$\varepsilon^{182}W_i$ = –3.12 ± 0.10
MSWD = 0.69
n = 8
$\varepsilon^{182}W$
$^{180}Hf/^{184}W$

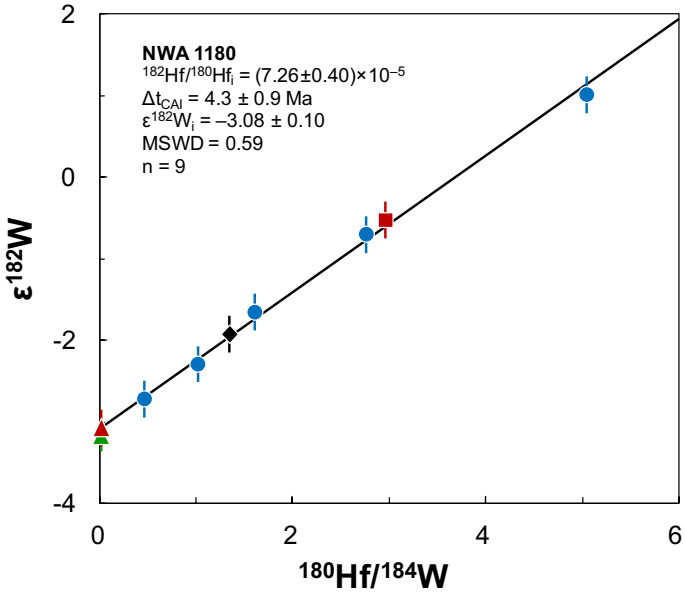
NWA 1180
$^{182}Hf/^{180}Hf_i = (7.26 \pm 0.40) \times 10^{-5}$
Δt_{CAI} = 4.3 ± 0.9 Ma
$\varepsilon^{182}W_i$ = –3.08 ± 0.10
MSWD = 0.59
n = 9
$\varepsilon^{182}W$
$^{180}Hf/^{184}W$

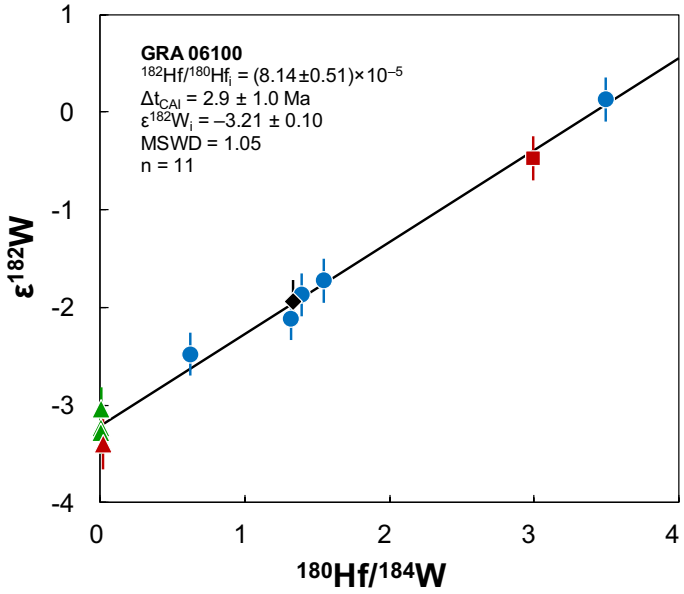
GRA 06100
$^{182}Hf/^{180}Hf_i = (8.14 \pm 0.51) \times 10^{-5}$
Δt_{CAI} = 2.9 ± 1.0 Ma
$\varepsilon^{182}W_i$ = –3.21 ± 0.10
MSWD = 1.05
n = 11
$\varepsilon^{182}W$
$^{180}Hf/^{184}W$

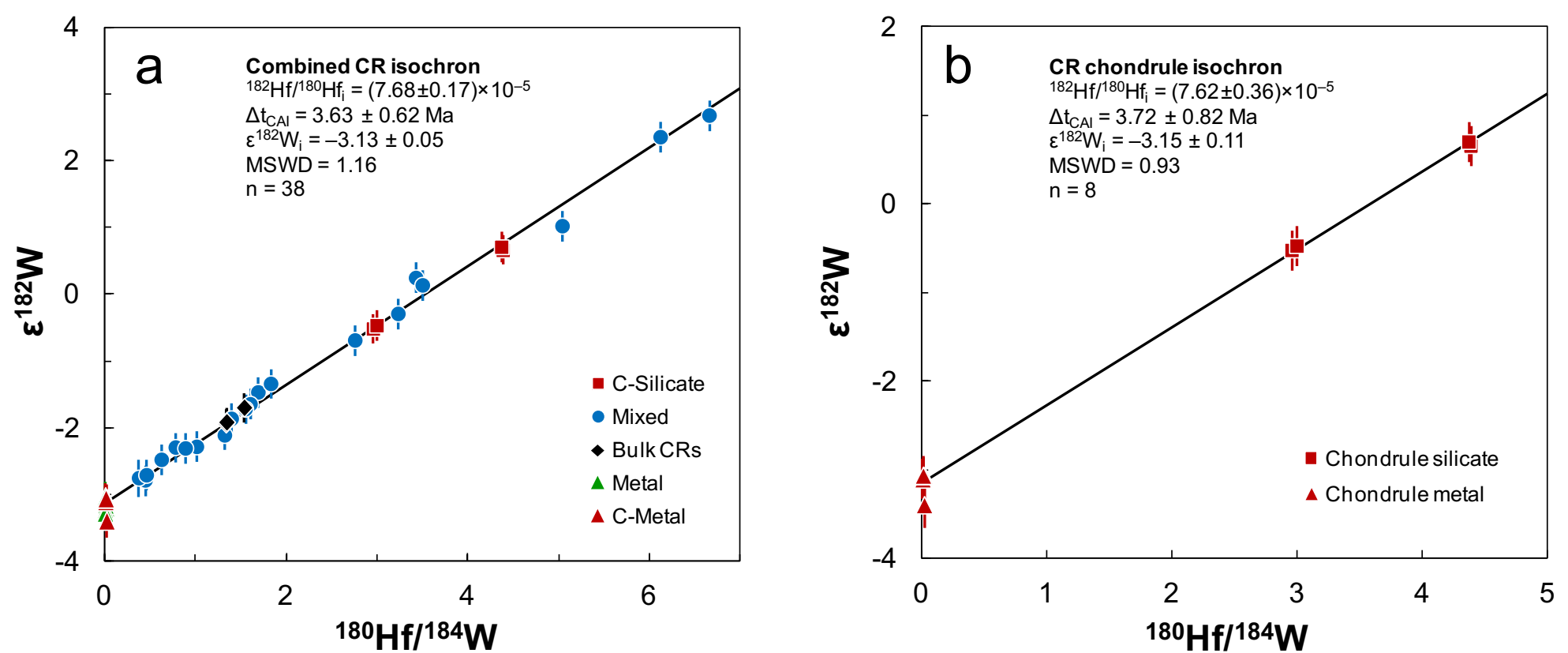
a
Combined CR isochron
$^{182}Hf/^{180}Hf_i = (7.68 \pm 0.17) \times 10^{-5}$
$\Delta t_{CAI} = 3.63 \pm 0.62$ Ma
$\varepsilon^{182}W_i = -3.13 \pm 0.05$
MSWD = 1.16
n = 38
C-Silicate
Mixed
Bulk CRs
Metal
C-Metal
$\varepsilon^{182}W$
$^{180}Hf/^{184}W$
b
CR chondrule isochron
$^{182}Hf/^{180}Hf_i = (7.62 \pm 0.36) \times 10^{-5}$
$\Delta t_{CAI} = 3.72 \pm 0.82$ Ma
$\varepsilon^{182}W_i = -3.15 \pm 0.11$
MSWD = 0.93
n = 8
Chondrule silicate
Chondrule metal
$\varepsilon^{182}W$
$^{180}Hf/^{184}W$

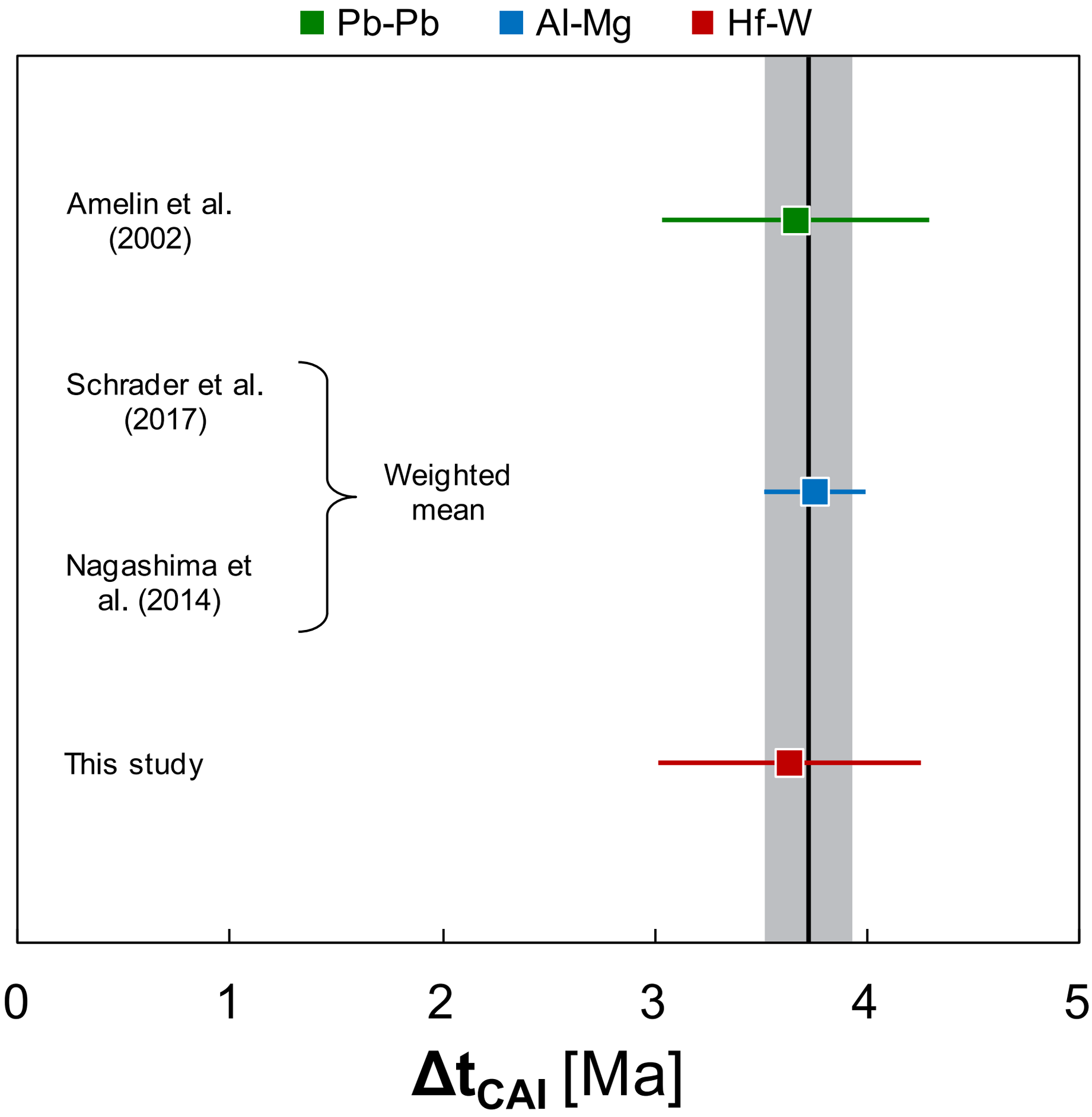
Pb-Pb
Al-Mg
Hf-W
Amelin et al. (2002)
Schrader et al. (2017)
Nagashima et al. (2014)
Weighted mean
This study
0
1
2
3
4
5
Δt_CAI [Ma]

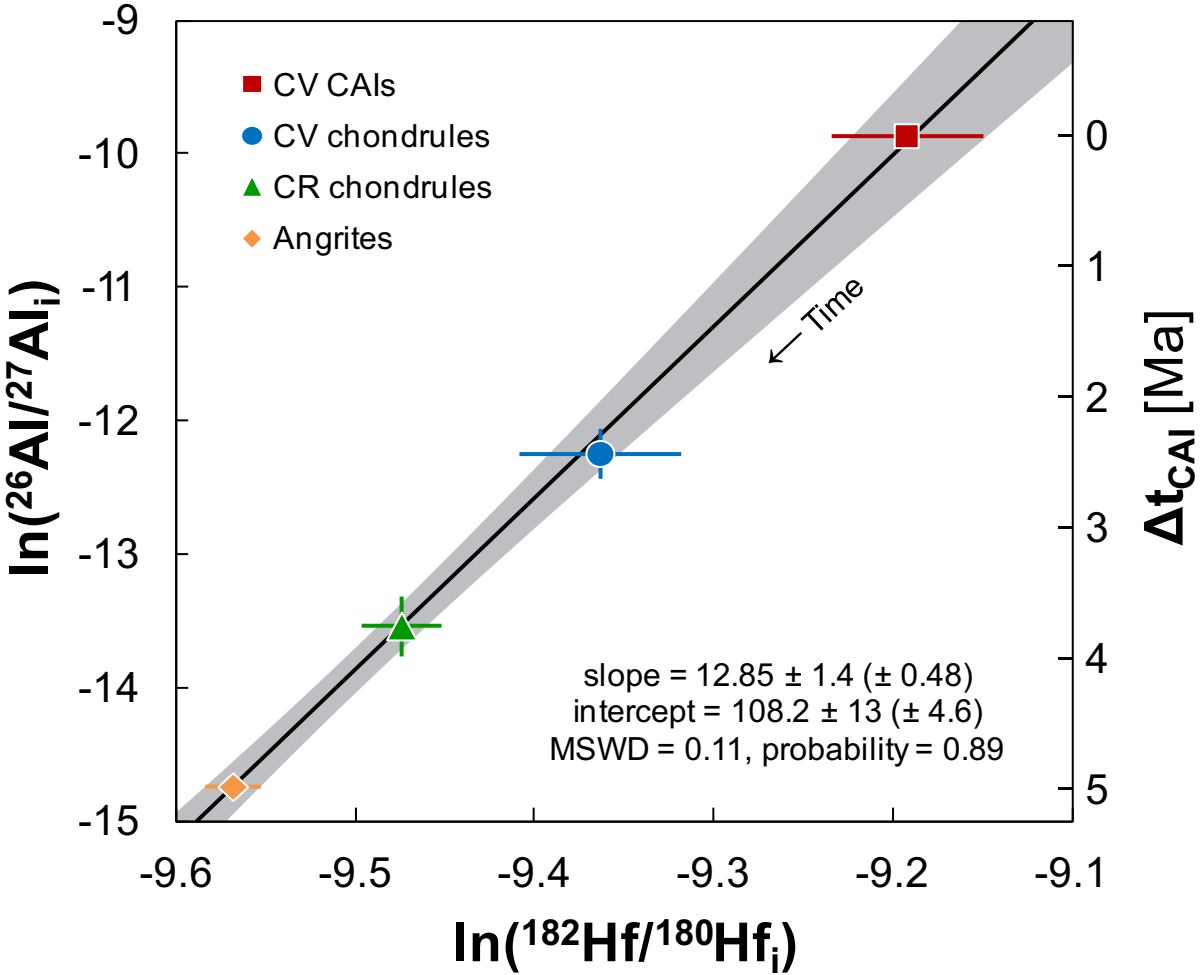
CV CAIs
CV chondrules
CR chondrules
Angrites
Time
slope = 12.85 ± 1.4 (± 0.48)
intercept = 108.2 ± 13 (± 4.6)
MSWD = 0.11, probability = 0.89
ln(26Al/27Ali)
ln(182Hf/180Hfi)
ΔtCAI [Ma]
-9
-10
-11
-12
-13
-14
-15
-9.6
-9.5
-9.4
-9.3
-9.2
-9.1
0
1
2
3
4
5

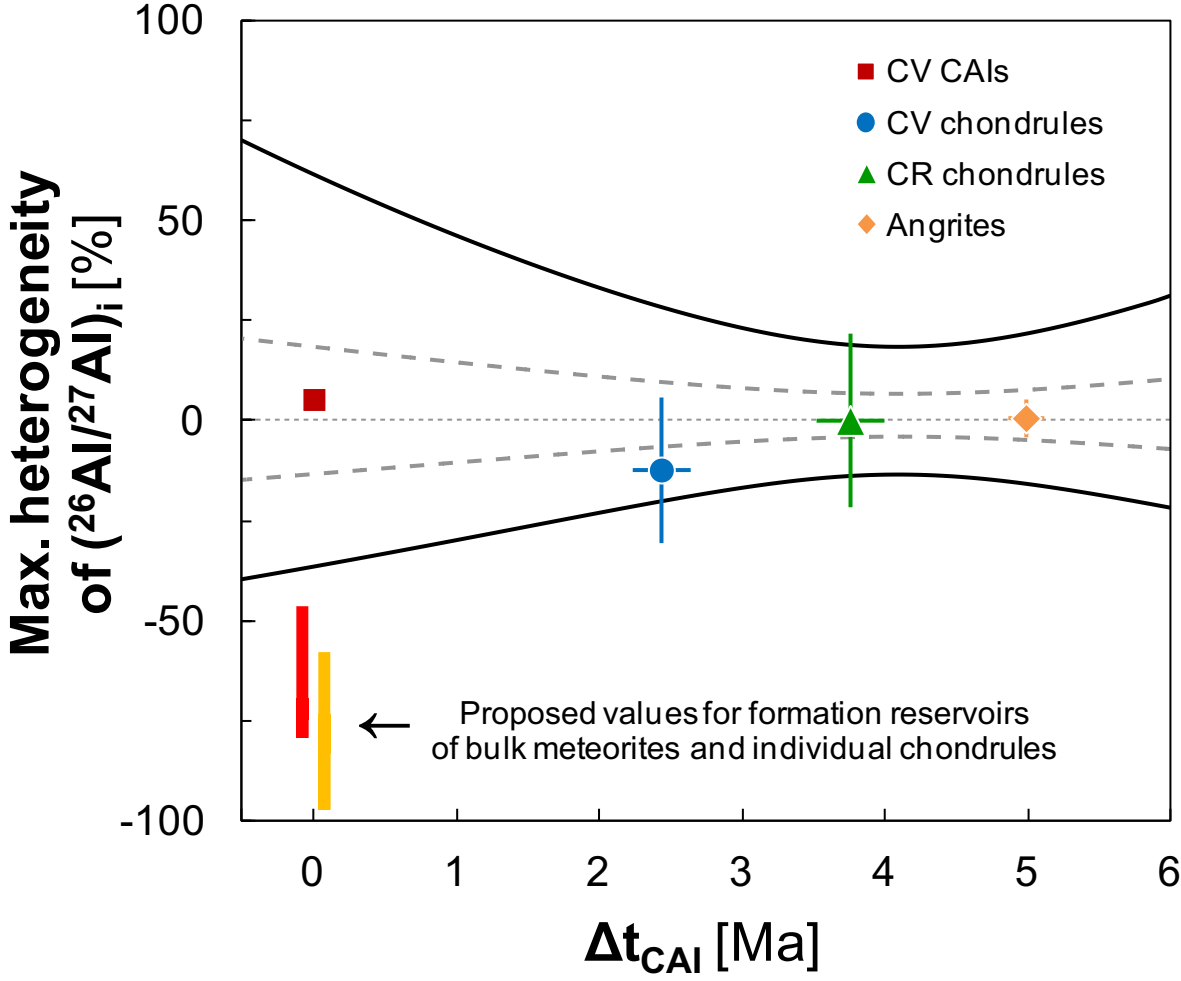
CV CAIs
CV chondrules
CR chondrules
Angrites
Proposed values for formation reservoirs
of bulk meteorites and individual chondrules
Max. heterogeneity
of $(^{26}Al/^{27}Al)_i$ [%]
Δt_{CAI} [Ma]
100
50
0
-50
-100
0
1
2
3
4
5
6

Supplementary Material

Hf-W chronology of CR chondrites: Implications for the timescales of chondrule formation and the distribution of ^{26}Al in the solar nebula

Gerrit Budde, Thomas S. Kruijer, Thorsten Kleine

S1 Chemical separation and isotope measurements of W

The chemical separation and isotope measurements of W followed the protocols described Budde et al. (2016b). After digestion and repeated dry-downs (Section 2.2), the samples were completely dissolved in 6 M HCl–0.06 M HF and small aliquots (~2–4%) were taken to determine Hf and W concentrations by isotope dilution (ID). The ID aliquots (equivalent to ~0.5–2 ng W and ~1–5 ng Hf; except for metal samples which had <30 pg Hf) were spiked with a mixed ^{180}Hf-^{183}W tracer that was calibrated against pure Hf and W metal standards (Kleine et al., 2002; Kleine et al., 2004). The chemical separation of Hf and W by anion exchange chromatography for ID analyses followed Kleine et al. (2004).

The separation of W from the unspiked aliquot for isotope composition analyses (IC) was performed using a two-stage anion exchange chromatography slightly modified from our previously established procedures (Kleine et al., 2012; Kruijer et al., 2012). The sample aliquots were loaded in 75 ml 0.5 M HCl–0.5 M HF onto columns filled with 4 ml of pre-cleaned Bio-Rad® AG1-X8 anion exchange resin (200–400 mesh). Most of the sample matrix was washed off the columns with the loading solution and additional 10 ml 0.5 M HCl–0.5 M HF, followed by elution of W in 15 ml 6 M HCl–1 M HF. After drying, the samples were dissolved in 6 ml 0.6 M HF–0.4% H_2O_2 and loaded onto clean-up columns containing 1 ml of pre-cleaned AG1-X8 resin. The columns were then rinsed with 10 ml 1 M HCl–2% H_2O_2, 9 ml 8 M HCl–0.01 M HF, and 0.5 ml 6 M HCl–1 M HF to quantitatively remove the HFSE (Ti, Zr, Hf, Ta), followed by elution of W with 8.5 ml 6 M HCl–1 M HF. The W cuts from both ion chromatography steps were evaporated at 200°C with added $HClO_4$ to destroy organic compounds. The W yield for this two-column procedure was typically ~70%. Depending on the digestion method,

total procedural blanks for the IC measurements ranged from 20 to 150 pg W and were negligible for all samples. Typical blanks for the Hf- and W-ID analyses were ~3 pg Hf and ~5 pg W, respectively. The blank corrections for the ID analyses were usually <1% and included in the uncertainty of the $^{180}Hf/^{184}W$ assuming an average uncertainty on the blank correction of 50%. Only the blank correction for the Hf-ID measurements of the metal samples were significant due to their very low Hf concentrations, resulting in large relative uncertainties on the $^{180}Hf/^{184}W$. Note, however, that the absolute uncertainties are very small and thus they do not compromise the chronological interpretation of the Hf-W data.

The W isotope measurements were performed on the Thermo Scientific® Neptune *Plus* MC-ICP-MS in the Institut für Planetologie at the University of Münster and followed the measurement protocol described in Kruijer et al. (2014a). The samples were introduced into the mass spectrometer using a Savillex® C-Flow PFA nebulizer connected to a Cetac® Aridus II desolvator. A combination of (Ni) Jet sampler and X skimmer cones was used and total ion beam intensities of ~1.7×10^{-10} A were obtained for a ~30 ppb W solution at a ~50 µl/min uptake rate. Each analysis consisted of 60 s baseline measurements (deflected beam) followed by 200 isotope ratio measurements of 4.2 s each and consumed ~25 ng of W. Instrumental mass bias was corrected by internal normalization to $^{186}W/^{184}W$ = 0.92767 (denoted '6/4') or $^{186}W/^{183}W$ = 1.98590 (denoted '6/3') using the exponential law. Possible isobaric interferences of Os on ^{184}W and ^{186}W were corrected by monitoring interference-free ^{188}Os and were negligible for all analyzed samples. The W isotope data are reported as ε-unit deviations (i.e., 0.01%) relative to the bracketing Alfa Aesar® solution standards (prepared from a pure W metal, batch no. 22312; Kleine et al., 2002; Kleine et al., 2004). For samples analyzed several times, the reported values represent the mean of pooled solution replicates.

The accuracy and precision of the W isotope measurements were assessed by repeated analyses of terrestrial rock (BHVO-2; ~0.5 g per digestion) and metal (NIST 129c; ~0.3 g per digestion) standards, several digestions of which were processed through the full analytical protocol and analyzed together with each set of samples. Both standards yield indistinguishable W isotope compositions (Tables S1 and S2), where the combined mean $\varepsilon^{182}W$ (6/4) of 0.00±0.14 (2 s.d., n=52) obtained during the course of this study is indistinguishable from the Alfa Aesar standard. We note that CR chondrites have low cosmic ray exposure ages of <25 Ma (Herzog and Caffee, 2014), making any neutron capture effects on $\varepsilon^{182}W$ in these meteorites negligible (Kruijer et al., 2012). As observed in previous high-precision W isotope studies (e.g., Budde et al., 2015; Budde et al., 2016b; Kruijer et al., 2014a; Kruijer et al., 2014b; Shirai and

Humayun, 2011; Willbold et al., 2011), normalizations involving ^{183}W show a small mass-independent effect (~0.1ε) for the terrestrial standard. This analytical artifact, which is most likely induced during incomplete dissolution of chemically purified W in Savillex® beakers, is consistent with the nuclear field shift effect and can be accurately corrected (Cook and Schönbächler, 2016). For the terrestrial standards (BHVO-2, NIST 129c), this effect was corrected as described in Kruijer et al. (2012), resulting in W isotope compositions that are indistinguishable from the Alfa Aesar standard—demonstrating that the W isotopic data are accurate—with an external reproducibility (2 s.d.) of ~0.1ε for all W isotope ratios (Tables S1 and S2). For the chondritic samples investigated here, all ε^{i}W values involving ^{183}W were corrected using the mean values obtained for the terrestrial standards (see Kruijer et al., 2014a), and the associated uncertainties induced through this correction were propagated into the final uncertainties reported for the W isotope data (Table 1). Of note, most nucleosynthetic W isotope anomalies (i.e., variations in ε^{183}W) observed in the present study are much larger than and thus clearly resolved from the small ^{183}W effects observed during mass spectrometric analyses. Moreover, after correction for the nuclear field shift effect and correction for nucleosynthetic isotope variations (Section 5.1), the ε^{182}W (6/4) and ε^{182}W (6/3) for each sample agree with each other to within 0.04ε (Fig. S2b).

S2 Chemical separation and isotope measurements of Mo

Chemical separation and isotope measurements of Mo followed the protocols described Budde et al. (2016a). Molybdenum was collected during the two-stage anion exchange chemistry used for the separation of W, where W is eluted in 6 M HCl–1 M HF, while Mo largely remained on the resin at this stage and was subsequently collected using 10 ml 3 M HNO_3. A small fraction (~15%) of the Mo is typically eluted together with W, and this Mo was collected at the end of the second W chemistry, again using (5 ml) 3 M HNO_3 for the Mo elution. The Mo cuts from both W separations were combined, and Mo concentrations for all samples were determined on small aliquots (equivalent to ~5 ng Mo) of the combined Mo cuts using a Thermo Scientific® XSeries 2 quadrupole ICP-MS in Münster. The subsequent purification of Mo for isotope composition analyses was performed using a two-stage ion exchange chromatography slightly modified after Burkhardt et al. (2011; 2014). The samples were loaded in 1 ml 1 M HCl onto columns filled with 1 ml pre-cleaned Eichrom® TRU Resin (100–150 µm) and, after rinsing with 6 ml 1 M HCl, Mo was eluted in 6 ml 0.1 M HCl. This chemistry was repeated once, but this time using 7 M HNO_3 and 0.1 M HNO_3

instead of 1 M HCl and 0.1 M HCl. The Mo cuts from all ion chromatography steps were evaporated with added HNO_3 and inverse aqua regia to destroy organic molecules. The Mo yield for the entire procedure was typically ~75%.

The Mo isotope measurements were performed on the Thermo Scientific® Neptune *Plus* MC-ICP-MS in the Institut für Planetologie at the University of Münster and followed the measurement protocol described in Budde et al. (2016a). The samples were introduced into the mass spectrometer using a Savillex® C-Flow PFA nebulizer connected to a Cetac® Aridus II desolvator. Standard Ni sample and (H) skimmer cones were used and total ion beam intensities of ~1.2×10^{-10} A were obtained for a ~100 ppb Mo solution at a ~50 µl/min uptake rate. Each measurement consumed ~80 ng of Mo and consisted of 40 baseline integrations (on-peak zeros) of 8.4 s each, followed by 100 Mo isotope ratio measurements of 8.4 s each. Instrumental mass bias was corrected by internal normalization to $^{98}Mo/^{96}Mo$ = 1.453173 (denoted '8/6') using the exponential law. This normalization is preferred because it results in large Mo isotope anomalies and distinctive isotope patterns (Burkhardt et al., 2011). Isobaric interferences of Zr and Ru on Mo masses were corrected by monitoring ^{91}Zr and ^{99}Ru. The final Mo cuts of the samples had Ru/Mo and Zr/Mo of $<1\times10^{-4}$, where the interference corrections for Ru (on $\varepsilon^{100}Mo$) and Zr (on $\varepsilon^{94}Mo$) were always <1ε and <2ε, respectively. Note that, as demonstrated in a previous study, Zr interference corrections of up to ~25ε (Zr/Mo ≈ 1.4×10^{-3}) and Ru interference corrections of >20ε (Ru/Mo ≈ 2.1×10^{-3}) are accurate to within analytical uncertainty (Budde et al., 2016a).

The Mo isotope data are reported as $\varepsilon^{i}Mo$ values relative to the mean of bracketing runs of the Alfa Aesar® solution standard, where $\varepsilon^{i}Mo = [(^{i}Mo/^{96}Mo)_{sample} / (^{i}Mo/^{96}Mo)_{standard} - 1] \times 10^{4}$ (i = 92, 94, 95, 97, 100). For samples analyzed several times, reported values represent the mean of pooled solution replicates. The accuracy and precision of the Mo isotope measurements were assessed by repeated analyses of the BHVO-2 and NIST 129c standards (Tables S3 and S4), several digestions of which were processed through the full analytical protocol and analyzed together with each set of samples. The $\varepsilon^{i}Mo$ values obtained for the terrestrial rock standard BHVO-2 are indistinguishable from the Alfa Aesar standard, demonstrating that the Mo isotopic data are accurate. However, repeated measurements of several digestions of the terrestrial metal standard NIST 129c clearly resolve small anomalies of about –0.3 for $\varepsilon^{92}Mo$ and –0.2 for $\varepsilon^{100}Mo$ relative to the Alfa Aesar standard. Note that such a negative offset was also observed in a previous study for this and another terrestrial metal standard (Burkhardt et al., 2011). The anomalies in $\varepsilon^{92}Mo$ and $\varepsilon^{100}Mo$ of NIST 129c are, therefore, most likely not due to an analytical problem, but are a genuine feature of this standard, which was probably induced during the industrial production process of this

high-sulfur steel. The external reproducibility of the Mo isotope measurements, as determined by repeated measurements of BHVO-2, ranges from 0.16 for ε^{97}Mo to 0.39 for ε^{92}Mo (2 s.d., n=24). Note that the external reproducibility of repeated measurements of NIST 129c is consistent with that of BHVO-2. Total procedural blanks were ~2–4 ng Mo and negligible for all samples.

S3 Effects of parent body processes on Hf-W systematics of GRA 06100

The CR2 chondrite Graves Nunataks (GRA 06100) has experienced substantial secondary alteration processes on the parent body, which distinguishes this sample from most other CR chondrites. Typically, CR chondrites escaped significant thermal metamorphism and underwent mild aqueous alteration at low temperatures, where metamorphic temperatures reached only ~200 °C (e.g., Briani et al., 2013). As is evident from a variety of mineralogical features, however, peak metamorphic temperatures for GRA 06100 might have exceeded 600 °C (Abreu and Bullock, 2013), which was attributed to shock-heating during an impact event. Petrographic observations also indicate that this samples experienced aqueous alteration at relatively high temperatures subsequent to shock-metamorphism (Abreu and Bullock, 2013; Briani et al., 2013). Based on its oxygen isotopic composition and petrographic properties, GRA 06100 was classified as petrologic type 2.5 (Harju et al., 2014; Schrader et al., 2011), demonstrating that this sample is substantially more altered than the other CR chondrites investigated in the present study. For a more detailed petrographic description of GRA 06100 see the aforementioned references.

Compared to the other (weakly altered) CR chondrites investigated in this study (NWA 801, Acfer 097, NWA 1180), the analyzed separates from GRA 06100 are characterized by anomalous chemical/elemental and isotopic signatures. For instance, the three metal fractions from GRA 06100, which are characterized by different grain sizes, have similar W concentrations of ~430 ppb. This is inconsistent with the observations for metal fractions of NWA 801 and data from Kong et al. (1999), which typically show an inverse correlation between grain size and concentration of siderophile elements in CR metal. Moreover, most fractions from GRA 06100 are characterized by significant deviations from the elemental Mo-W trend (Mo/W ≈ 8.6) defined by samples from the other CR chondrites (Fig. S1b). While the least-magnetic fractions (MS-4, MS-5) have sub-chondritic Mo/W of ~5, the metal (and metal-rich) fractions show highly elevated Mo/W of up to ~17 for the chondrule metal. These variations in Mo/W in samples from GRA 06100 are accompanied by anomalies in the

elemental abundances of Hf and W, which are most pronounced in the magnetic separates. For example, compared to the average concentration of similar fractions from the weakly altered CR chondrites, MS-2 has a (~18%) higher Hf concentration, whereas MS-4 and MS-5 have (~12%) lower Hf contents. Furthermore, MS-1 and MS-2 are depleted in W (~26%), while the less magnetic fractions, particularly MS-4, have significantly higher W concentrations (~24–74%). These variations combined result in very little variability in the ^{180}Hf/^{184}W of MS-2, MS-3, and MS-4, all of which have values similar to that of the bulk meteorite. Of note, MS-1 and MS-2 have ~50% higher ^{180}Hf/^{184}W, whereas MS-4 and MS-5 have ~50% lower ^{180}Hf/^{184}W than similar fractions from the other CR chondrites.

In addition to these elemental anomalies, samples from GRA 06100 are characterized by unusual W and Mo isotope signatures. For instance, the magnetic separates show highly variable ε^{183}W ranging between –0.3 and +1.1, while the magnetic separates from the weakly altered CR chondrites have indistinguishable ε^{183}W of ~0.6. The MS-3 fraction of GRA 06100 is the only analyzed sample that shows a deficit in ε^{183}W, which is consistent with its negative Mo isotope anomaly (ε^{92}Mo ≈ –2.1). In addition to the mixed fractions, other sample types from GRA 06100 also show significant deviations (larger excesses) in ε^{183}W (Fig. 1). For example, metal from the other CR chondrites has a uniform ε^{183}W of ~0.14; however, the metal and chondrule metal separates from GRA 06100 show much larger excesses of ~0.3 and ~0.5, respectively. Similarly, the silicate-dominated chondrule fraction has an ε^{183}W anomaly of ~1.1, which is much larger than those of the C-S fractions from the weakly altered CR chondrites (ε^{183}W ≈ 0.5).

These distinct features of GRA 06100 most likely result from parent body processes that affected this sample, where most of them can be attributed to the decomposition of the abundant Fe-Ni metal. With increasing degree of aqueous alteration Fe-Ni metal in CR chondrites is progressively replaced by oxides, particularly magnetite, and to a minor extent by other phases such as sulfides (e.g., Harju et al., 2014). This is consistent with the low amount of metal (2.1 wt.%) recovered for GRA 06100 compared to the weakly altered samples NWA 801 and Acfer 097 (~5–6 wt.%) (Section 2.1). Since the major fraction of W (and Mo) in CR chondrites is hosted in Fe-Ni metal, this alteration resulted in the liberation of significant amounts of W that was then incorporated in secondary phases. These phases have different magnetic properties and, therefore, hampered an efficient separation of high-Hf/W (silicate) and low-Hf/W (metal) phases using hand-magnets, resulting in the low variation in Hf/W among the different magnetic separates from GRA 06100. Apparently this process also resulted in a partial decoupling of W and Mo, as is evident from the large variations in Mo/W.

The unusual ε^{183}W (and ε^{i}Mo) signatures can potentially be explained by a by parent body processes as well. CR chondrites contain abundant (up to ~200 ppm) presolar grains, which are the carriers of nucleosynthetic anomalies. As discussed by Leitner et al. (2012; 2016), not only the total concentration of these grains, but also the presolar silicate/oxide and silicate/SiC ratios in CR chondrites decrease with increasing degree of aqueous alteration of the respective host meteorite, indicating that presolar silicates are preferentially destructed over oxides and SiC. The details of this process remain uncertain; however, a redistribution of isotopically anomalous W (and Mo) in GRA 06100 due to (selective) destruction of presolar phases during aqueous alteration seems a likely explanation for the unusual isotopic signatures.

Regardless of the exact origin, these findings show that GRA 06100 was affected by elemental redistribution due to secondary alteration processes on the parent body, which is not observed for the other investigated samples (NWA 801, Acfer 097, NWA 1180). However, these processes most likely had no effect on the values measured for the bulk meteorite, which is supported by the fact that the concentration and isotope composition data for bulk GRA 06100 is indistinguishable from the weakly altered CR chondrites. Moreover, we note that in spite of the anomalous elemental and isotopic signatures in the GRA 06100 samples, secondary effects did not significantly disturb the ^{182}Hf-^{182}W systematics of this sample. For instance, the analyzed fractions yield a well-defined isochron (MSWD = 1.05) corresponding to a Hf-W age of 2.9±1.0 Ma after CAIs, which is in good agreement with those obtained for the other CR chondrites (see Section 5.2 for further discussion).

At first glance, this seems contradictory, but these observations can be explained by the fact that no radiogenic ^{182}W was mobilized. This is because the remobilized W was hosted in Fe-Ni metal (which in case of GRA 06100 was largely decomposed during the aqueous alteration), and so was not radiogenic because of the very low Hf/W (<0.03) of the metal (i.e., there occurred virtually no radiogenic ingrowth of ^{182}W in the metal after its formation). In contrast, radiogenic ^{182}W is produced in silicates having high Hf/W (e.g., high-Ca pyroxene), which remained unaffected by the parent body processes. Therefore, the silicates did not exchange their (radiogenic) W with other phases and, hence, the Hf-W systematics remained essentially undisturbed although there occurred significant redistribution of (unradiogenic) W released from the metal. Note that a mobilization of radiogenic W would result in significant scatter on the isochron and an apparent age that is too young; however this is not observed. Hence, the Hf-W systematics even in GRA 06100, which underwent substantial thermal metamorphism and aqueous alteration, remained essentially undisturbed, demonstrating the high robustness of the ^{182}Hf-^{182}W system as a chronometer.

S4 Supplementary figures and data tables

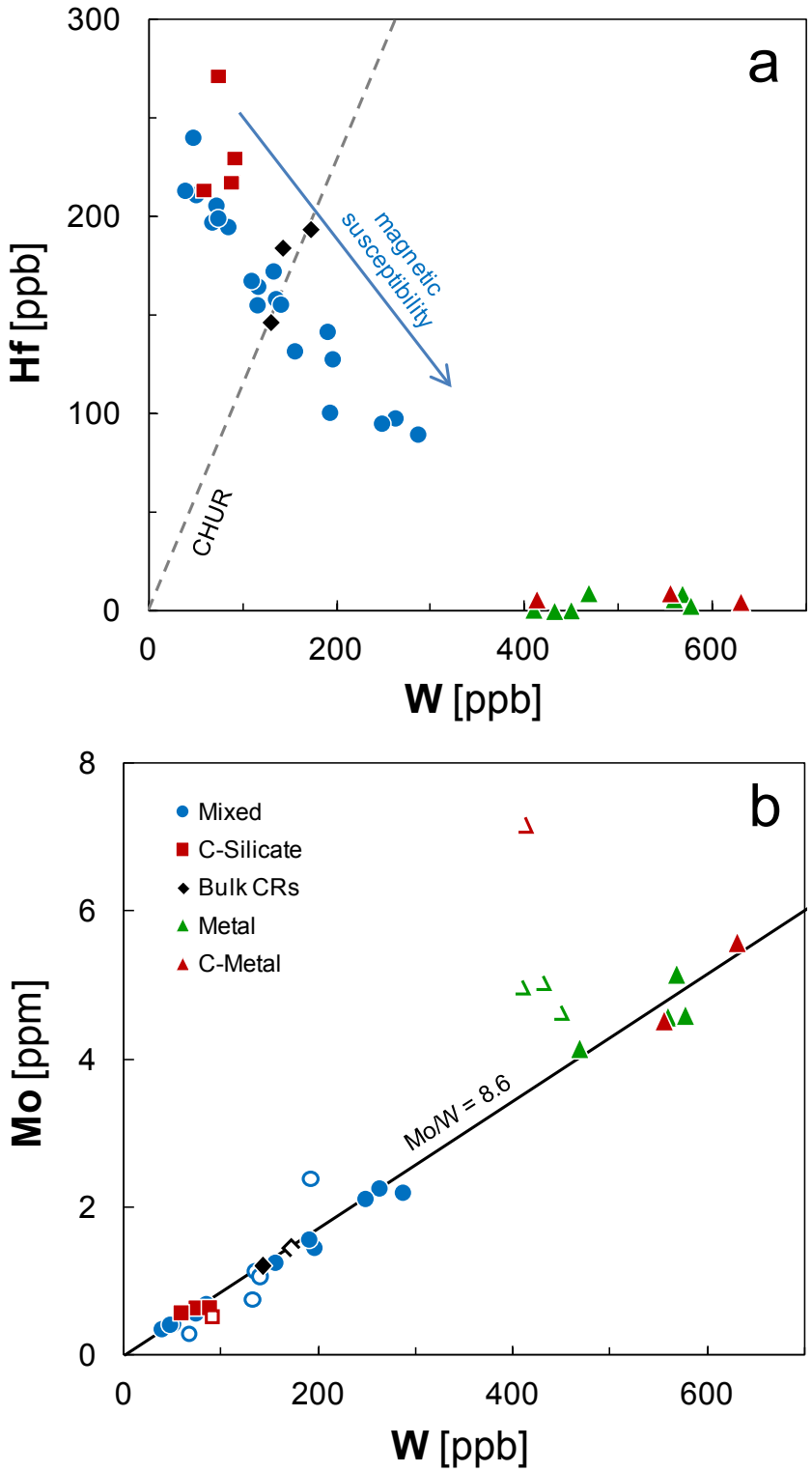

Fig. S1. Hf (a) and Mo (b) versus W concentration diagrams for the CR chondrite samples. Open symbols in (b) are GRA 06100 samples. Note that the data points for chondrule metal from NWA 801 (5.5 ppb Hf, 1109 ppb W, 10.1 ppm Mo) were omitted in these diagrams for clarity. Mixed: magnetic separates, C: chondrule (silicate/metal).

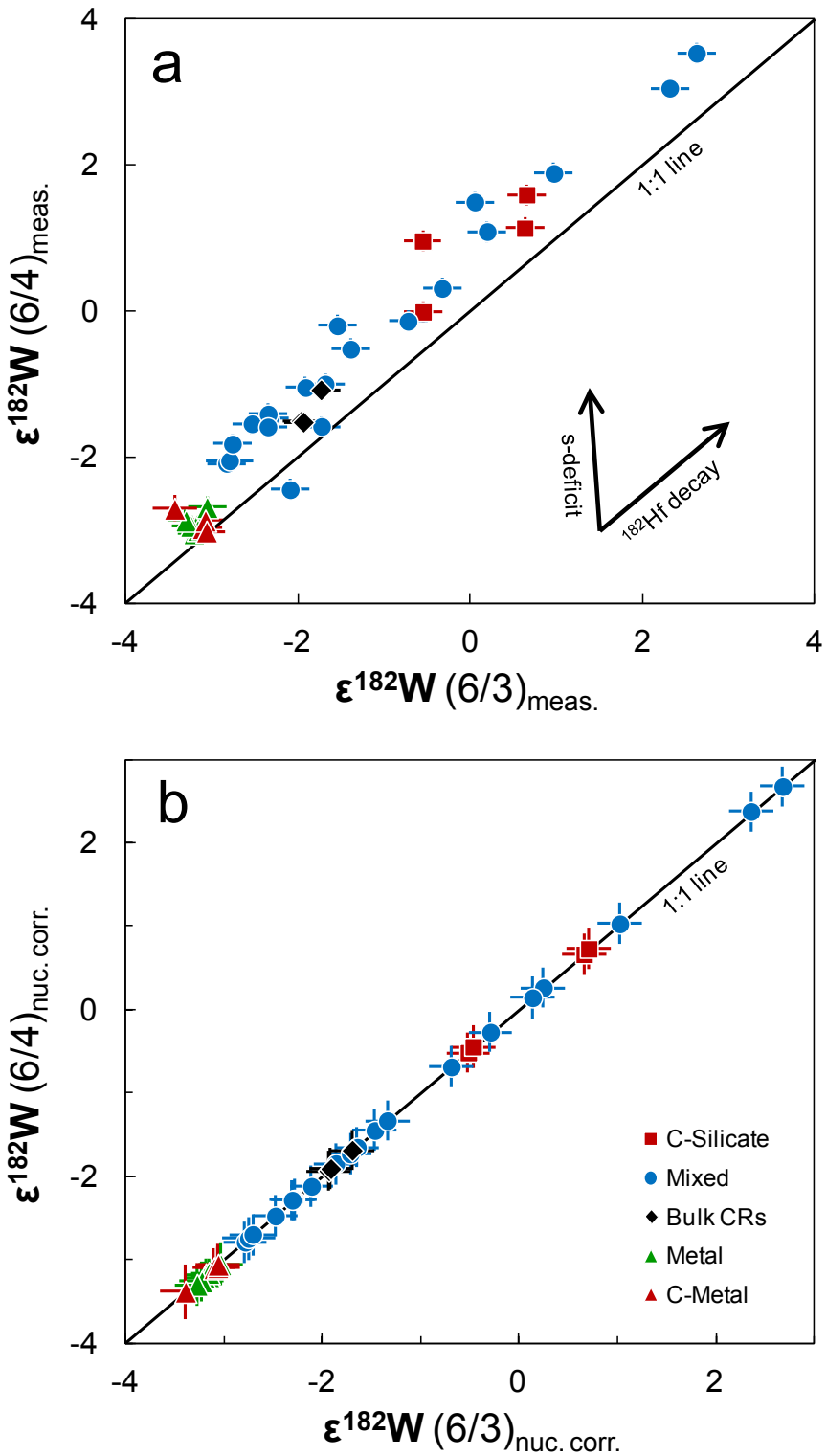

Fig. S2. The 6/3- and 6/4-normalizations yield distinct ε^{182}W values for the CR chondrite samples (a), where the difference between the two normalizations scales with the magnitude of the anomaly in ε^{183}W. After correction for nucleosynthetic W isotope anomalies (using ε^{182}W–ε^{183}W and ε^{182}W–ε^{184}W slopes of 1.25±0.06 and 0.12±0.07, respectively; Budde et al., 2016b), both normalizations yield consistent ε^{182}W (b). Note that the correction of the ^{186}W/^{183}W-normalized values is much smaller and, therefore, those values are preferred.

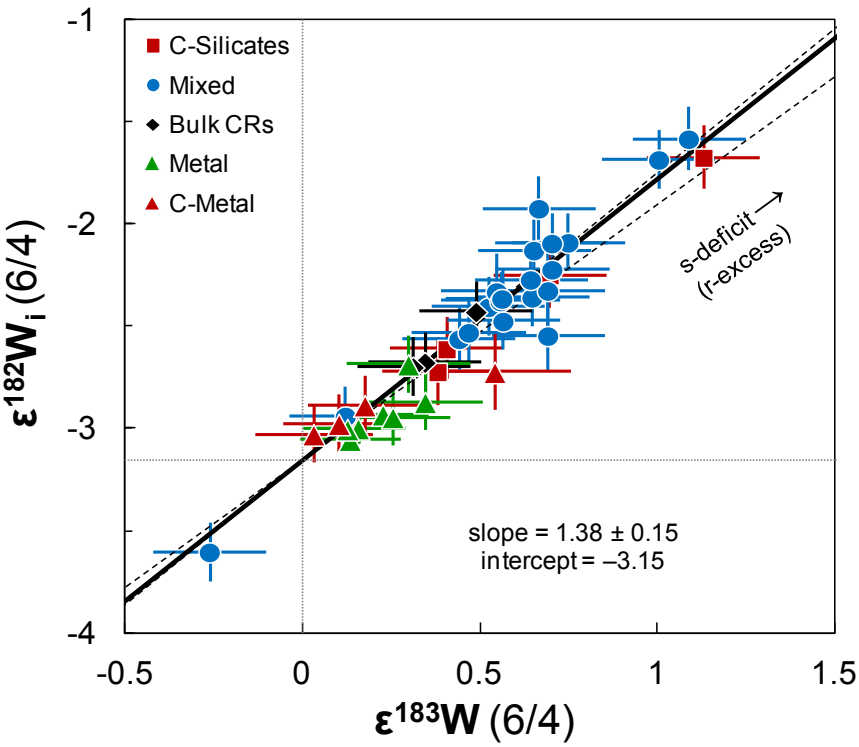

Fig. S3. In a diagram of (^{182}Hf decay-corrected) $\varepsilon^{182}W_i$ versus $\varepsilon^{183}W$ (normalized to $^{186}W/^{184}W$), the CR chondrite samples plot along a line with a slope that is consistent with the slopes (dashed lines) defined by data for CAIs and acid leachates (1.41±0.06; Burkhardt and Schönbächler, 2015; Kruijer et al., 2014a), as well as for Allende chondrule and matrix separates (1.25±0.06; Budde et al., 2016b). This demonstrates that the observed (non-radiogenic) W isotope variations are of nucleosynthetic origin, where almost all samples are characterized by variable *s*-deficits (or *r*-excesses). Note that the intercept ($\varepsilon^{182}W_i$) and the initial $^{182}Hf/^{180}Hf$ [(7.62±0.17)×10^{-5}] used for the ^{182}Hf decay correction of the $\varepsilon^{182}W$ (6/4) values (for this plot) were obtained by a combined isochron regression using the measured $\varepsilon^{182}W$ (6/3) values, for which the correction of nucleosynthetic W isotope anomalies is negligible (Section 4.1).

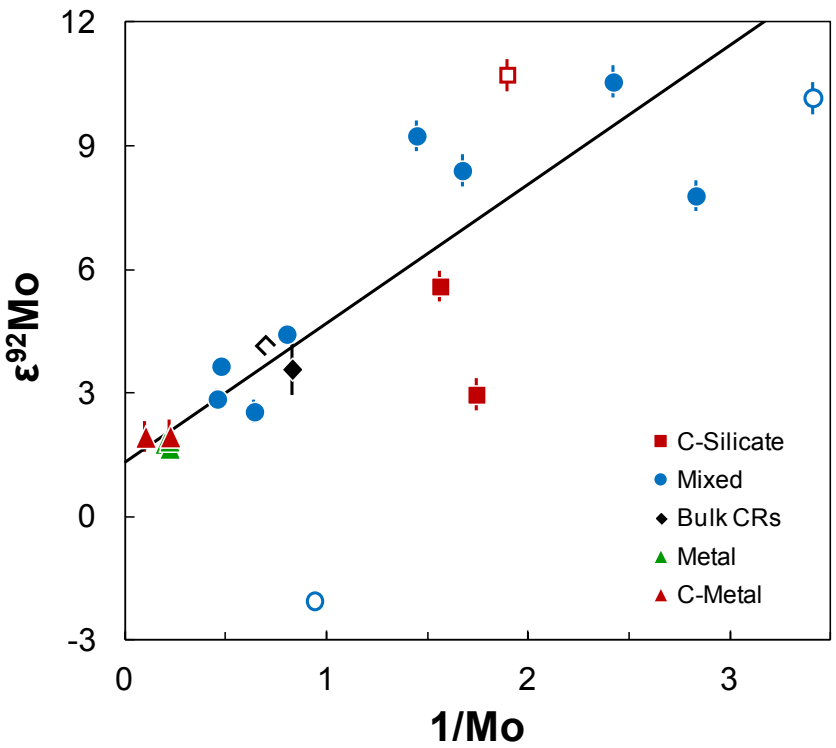

Fig. S4. Diagram of ε^{92}Mo versus 1/Mo [ppm^{-1}] for the CR chondrite samples, demonstrating that overall metal- and Mo-poor (silicate) samples have larger *s*-process deficits than bulk CR chondrites, which counterbalance the isotopic composition of the metal. Note that the different samples are not expected to plot on a single mixing line since the CR chondrites are not simple two-component mixtures (Section 5.1; Fig. S1a).

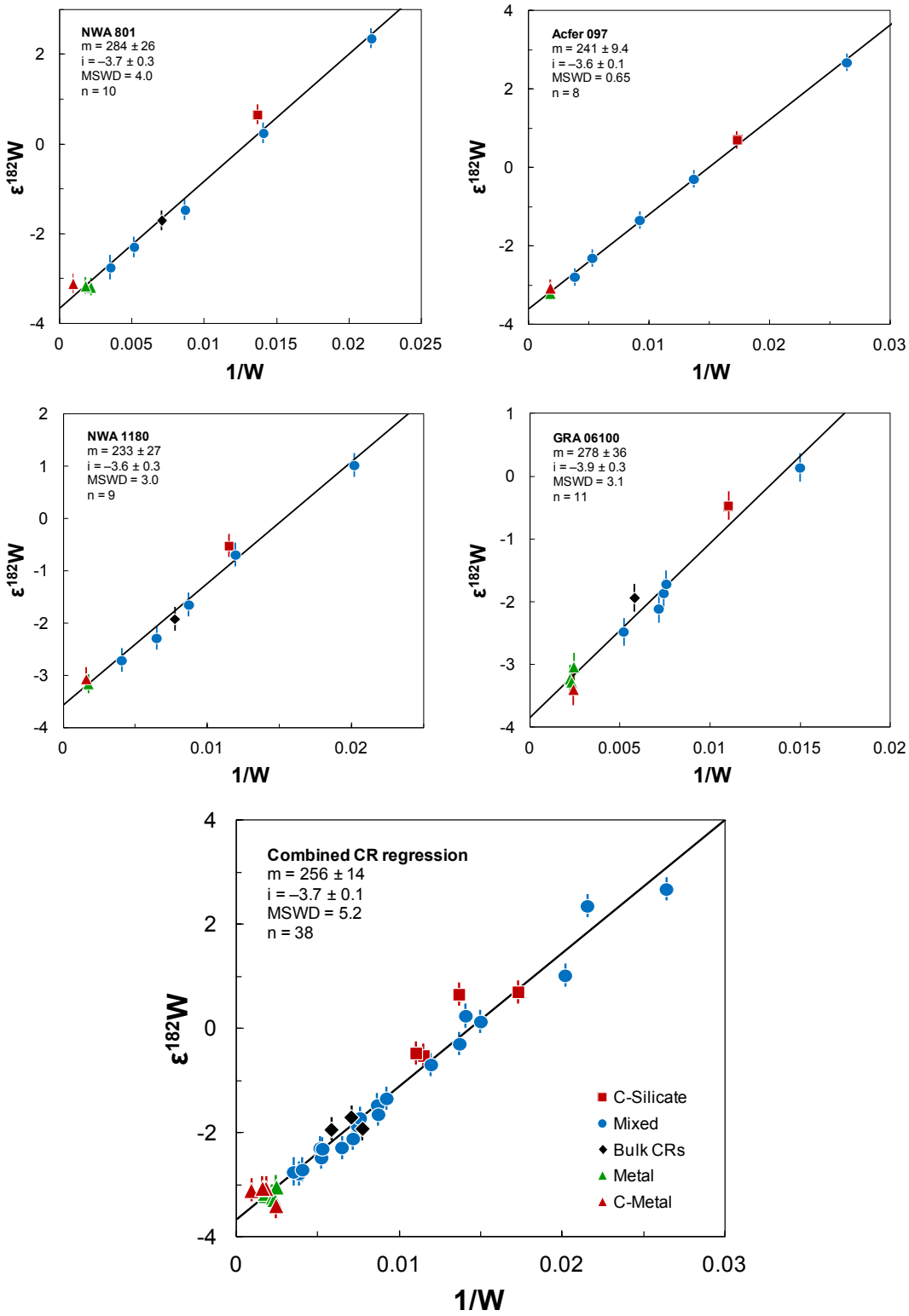

Fig. S5. Overall the ε^{182}W (6/3) and 1/W [ppb^{-1}] of the CR chondrite samples are positively correlated. However, the scatter (MSWD) in these plots is much larger than observed in the isochron diagrams (Figs. 6 and 7a), demonstrating that the isochrons are not mixing lines.

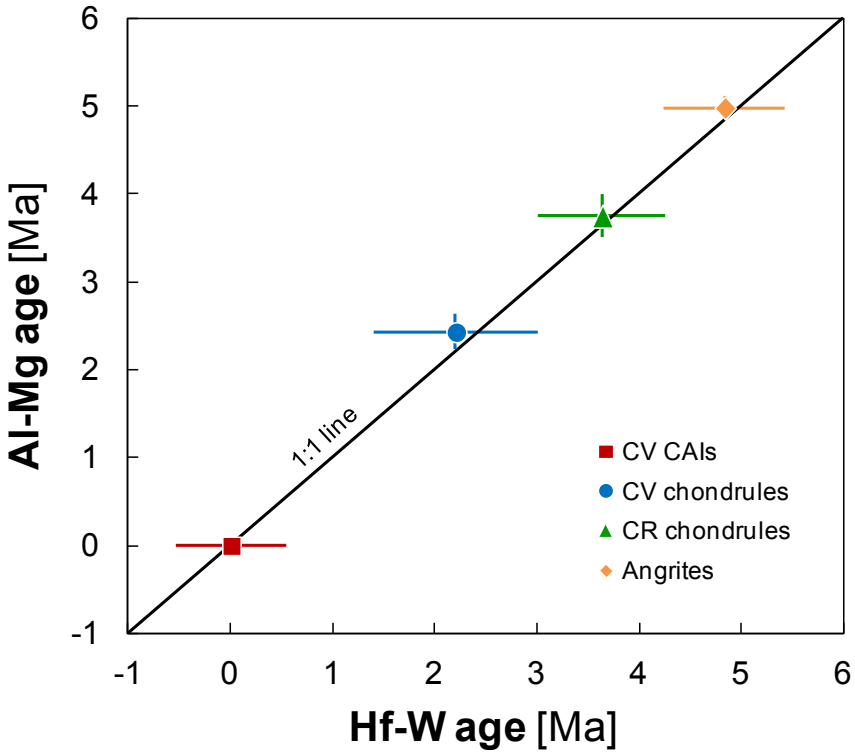

Fig. S6. Direct comparison of Al-Mg and Hf-W ages for CV CAIs, CV chondrules, CR chondrules, and angrites, which cover the entire effective lifetime of ^{26}Al. Ages are calculated relative to CV CAIs, assuming a homogeneous distribution of ^{26}Al and ^{182}Hf. Data sources and values are provided in Table 3.

Table S1. Hf-W isotope data for the terrestrial rock standard BHVO-2.

ID	Hf (ng/g)	W (ng/g)	$\varepsilon^{182}W_{meas.}$ (± 2 s.e.)	$\varepsilon^{183}W_{meas.}$ (± 2 s.e.)	$\varepsilon^{183}W_{corr.}$ [a] (± 2σ)	$\varepsilon^{182}W_{meas.}$ (± 2 s.e.)	$\varepsilon^{182}W_{corr.}$ [a] (± 2σ)	$\varepsilon^{184}W_{meas.}$ (± 2 s.e.)	$\varepsilon^{184}W_{corr.}$ [a] (± 2σ)
			normalized to $^{186}W/^{184}W$ = 0.92767			normalized to $^{186}W/^{183}W$ = 1.98590			
BHV13.1	4507	214	0.05 ± 0.09	-0.04 ± 0.08	0.03 ± 0.12	0.10 ± 0.09	0.04 ± 0.14	0.03 ± 0.05	-0.02 ± 0.11
BHV13.2	–	–	-0.03 ± 0.08	-0.04 ± 0.07	0.01 ± 0.09	0.07 ± 0.06	0.01 ± 0.11	0.03 ± 0.04	-0.01 ± 0.08
BHV13.3	–	–	-0.09 ± 0.09	-0.13 ± 0.08	-0.08 ± 0.13	0.07 ± 0.10	-0.11 ± 0.15	0.09 ± 0.06	0.05 ± 0.12
BHV14.1	–	–	-0.13 ± 0.08	-0.18 ± 0.08	-0.12 ± 0.12	0.09 ± 0.08	-0.16 ± 0.13	0.12 ± 0.05	0.08 ± 0.10
BHV14.2	–	–	0.06 ± 0.08	0.02 ± 0.08	0.06 ± 0.11	0.06 ± 0.07	0.09 ± 0.13	-0.01 ± 0.05	-0.04 ± 0.09
BHV14.3	–	–	0.11 ± 0.09	-0.14 ± 0.08	0.06 ± 0.12	0.27 ± 0.09	0.08 ± 0.14	0.09 ± 0.05	-0.04 ± 0.11
BHV14.4	–	–	-0.05 ± 0.10	-0.04 ± 0.08	-0.03 ± 0.13	0.02 ± 0.09	-0.04 ± 0.15	0.03 ± 0.06	0.02 ± 0.11
BHV15.1	4483	212	-0.11 ± 0.10	-0.19 ± 0.09	-0.10 ± 0.13	0.13 ± 0.09	-0.13 ± 0.15	0.13 ± 0.06	0.06 ± 0.11
BHV15.2	–	–	-0.05 ± 0.09	-0.12 ± 0.08	-0.06 ± 0.12	0.08 ± 0.09	-0.09 ± 0.14	0.08 ± 0.05	0.04 ± 0.11
BHV15.3	–	–	-0.06 ± 0.09	-0.28 ± 0.07	-0.07 ± 0.11	0.30 ± 0.08	-0.10 ± 0.13	0.19 ± 0.05	0.05 ± 0.10
BHV16.1	4397	214	-0.09 ± 0.09	-0.13 ± 0.08	-0.08 ± 0.12	0.07 ± 0.08	-0.10 ± 0.13	0.08 ± 0.05	0.05 ± 0.10
BHV16.2	–	–	0.06 ± 0.09	-0.13 ± 0.07	0.02 ± 0.11	0.22 ± 0.07	0.04 ± 0.13	0.09 ± 0.05	-0.02 ± 0.09
BHV16.3	–	–	-0.03 ± 0.09	-0.16 ± 0.08	-0.02 ± 0.11	0.21 ± 0.07	-0.02 ± 0.13	0.11 ± 0.05	0.01 ± 0.10
BHV17.1	–	–	-0.05 ± 0.09	-0.20 ± 0.08	-0.06 ± 0.12	0.20 ± 0.08	-0.08 ± 0.14	0.13 ± 0.05	0.04 ± 0.11
BHV17.2	–	–	-0.05 ± 0.08	-0.11 ± 0.08	-0.03 ± 0.12	0.12 ± 0.09	-0.04 ± 0.14	0.07 ± 0.05	0.02 ± 0.11
BHV17.3	–	–	-0.01 ± 0.08	-0.14 ± 0.08	-0.03 ± 0.11	0.17 ± 0.07	-0.03 ± 0.13	0.09 ± 0.05	0.02 ± 0.10
BHV18.1	–	–	-0.05 ± 0.08	-0.12 ± 0.07	-0.04 ± 0.11	0.11 ± 0.08	-0.05 ± 0.13	0.08 ± 0.05	0.03 ± 0.10
BHV18.2	–	–	-0.12 ± 0.08	-0.27 ± 0.07	-0.11 ± 0.10	0.24 ± 0.07	-0.14 ± 0.12	0.18 ± 0.05	0.07 ± 0.09
BHV18.3	–	–	0.03 ± 0.10	-0.18 ± 0.08	0.01 ± 0.12	0.27 ± 0.09	0.02 ± 0.14	0.12 ± 0.05	-0.01 ± 0.11
BHV19.1	4522	215	-0.06 ± 0.09	-0.17 ± 0.08	-0.05 ± 0.12	0.18 ± 0.08	-0.07 ± 0.13	0.12 ± 0.05	0.03 ± 0.10
BHV19.2	–	–	0.00 ± 0.08	-0.22 ± 0.07	-0.01 ± 0.12	0.30 ± 0.08	-0.01 ± 0.13	0.15 ± 0.05	0.01 ± 0.10
BHV19.3	–	–	-0.09 ± 0.10	-0.15 ± 0.08	-0.07 ± 0.13	0.13 ± 0.09	-0.09 ± 0.14	0.10 ± 0.05	0.04 ± 0.11
BHV20.1	4544	218	0.06 ± 0.11	-0.17 ± 0.09	0.05 ± 0.14	0.31 ± 0.09	0.08 ± 0.15	0.11 ± 0.06	-0.04 ± 0.12
BHV20.2	–	–	-0.08 ± 0.09	-0.20 ± 0.08	-0.06 ± 0.12	0.21 ± 0.09	-0.08 ± 0.14	0.13 ± 0.05	0.04 ± 0.11
BHV20.3	–	–	-0.04 ± 0.10	-0.13 ± 0.09	-0.03 ± 0.14	0.14 ± 0.09	-0.04 ± 0.16	0.09 ± 0.06	0.02 ± 0.12
BHV21.1	–	–	0.01 ± 0.11	-0.18 ± 0.10	0.01 ± 0.14	0.26 ± 0.09	0.01 ± 0.16	0.12 ± 0.06	-0.01 ± 0.12
BHV21.2	–	–	-0.08 ± 0.10	-0.25 ± 0.10	-0.09 ± 0.14	0.23 ± 0.09	-0.12 ± 0.16	0.17 ± 0.06	0.06 ± 0.12
N	5	5	27	27	27	27	27	27	27
Mean	4491	215	-0.03	-0.15	-0.03	0.17	-0.04	0.10	0.02
2 s.d.	114	4.9	0.13	0.14	0.10	0.17	0.14	0.09	0.07
95% CI	71	3.0	0.03	0.03	0.02	0.03	0.03	0.02	0.01

Different numbers (13–21) denote separate digestions of ~0.5 g standard material that were processed through the full chemical separation procedure and analyzed with each set of samples. A single analysis consumed ~25 ng of W (run at ~30 ppb).

[a] Corrected for a small mass-independent effect on ^{183}W after Kruijer et al. (2012) (Section S1).

Table S2. Hf-W isotope data for the terrestrial metal standard NIST 129c.

ID	Hf (ng/g)	W (ng/g)	$\varepsilon^{182}W_{meas.}$ (± 2 s.e.)	$\varepsilon^{183}W_{meas.}$ (± 2 s.e.)	$\varepsilon^{183}W_{corr.}$ [a] (± 2σ)	$\varepsilon^{182}W_{meas.}$ (± 2 s.e.)	$\varepsilon^{182}W_{corr.}$ [a] (± 2σ)	$\varepsilon^{184}W_{meas.}$ (± 2 s.e.)	$\varepsilon^{184}W_{corr.}$ [a] (± 2σ)
			normalized to $^{186}W/^{184}W$ = 0.92767			normalized to $^{186}W/^{183}W$ = 1.98590			
N9C01.1	–	–	-0.11 ± 0.08	-0.16 ± 0.07	-0.10 ± 0.10	0.09 ± 0.07	-0.14 ± 0.12	0.11 ± 0.05	0.07 ± 0.09
N9C01.2	–	–	0.09 ± 0.08	-0.17 ± 0.06	0.02 ± 0.09	0.27 ± 0.06	0.04 ± 0.11	0.11 ± 0.04	-0.02 ± 0.08
N9C01.3	–	–	-0.03 ± 0.08	-0.16 ± 0.06	-0.02 ± 0.10	0.20 ± 0.07	-0.03 ± 0.11	0.11 ± 0.04	0.02 ± 0.09
N9C01.4	–	–	0.03 ± 0.09	-0.12 ± 0.07	0.01 ± 0.11	0.19 ± 0.07	0.02 ± 0.12	0.08 ± 0.05	-0.01 ± 0.09
N9C01.5	–	–	-0.04 ± 0.08	-0.15 ± 0.08	-0.04 ± 0.12	0.15 ± 0.08	-0.05 ± 0.13	0.10 ± 0.05	0.03 ± 0.10
N9C02.1	0	725	0.00 ± 0.08	-0.12 ± 0.07	-0.01 ± 0.11	0.16 ± 0.07	-0.02 ± 0.13	0.08 ± 0.05	0.01 ± 0.09
N9C02.2	–	–	0.06 ± 0.08	-0.09 ± 0.07	0.02 ± 0.10	0.16 ± 0.07	0.03 ± 0.12	0.06 ± 0.04	-0.02 ± 0.09
N9C02.3	–	–	0.08 ± 0.07	-0.06 ± 0.07	0.00 ± 0.11	0.09 ± 0.08	0.00 ± 0.12	0.04 ± 0.05	0.00 ± 0.10
N9C02.4	–	–	0.07 ± 0.08	-0.09 ± 0.07	0.05 ± 0.11	0.19 ± 0.08	0.07 ± 0.13	0.06 ± 0.05	-0.03 ± 0.10
N9C02.5	–	–	0.06 ± 0.09	-0.16 ± 0.08	0.04 ± 0.12	0.29 ± 0.08	0.06 ± 0.14	0.11 ± 0.05	-0.03 ± 0.11
N9C03.1	–	–	0.06 ± 0.09	-0.11 ± 0.08	0.04 ± 0.12	0.22 ± 0.08	0.07 ± 0.13	0.07 ± 0.05	-0.03 ± 0.10
N9C03.2	–	–	-0.02 ± 0.09	-0.18 ± 0.08	-0.03 ± 0.12	0.21 ± 0.08	-0.04 ± 0.14	0.12 ± 0.05	0.02 ± 0.11
N9C03.3	–	–	0.05 ± 0.08	-0.17 ± 0.08	0.02 ± 0.13	0.28 ± 0.09	0.04 ± 0.14	0.12 ± 0.05	-0.02 ± 0.11
N9C03.4	–	–	0.10 ± 0.09	-0.18 ± 0.08	0.06 ± 0.12	0.34 ± 0.08	0.09 ± 0.13	0.12 ± 0.05	-0.04 ± 0.10
N9C03.5	–	–	0.08 ± 0.09	-0.22 ± 0.07	0.04 ± 0.11	0.37 ± 0.08	0.07 ± 0.13	0.14 ± 0.05	-0.03 ± 0.10
N9C04.1	0	771	0.06 ± 0.11	-0.09 ± 0.10	0.05 ± 0.15	0.19 ± 0.10	0.07 ± 0.17	0.06 ± 0.06	-0.03 ± 0.13
N9C04.2	–	–	-0.01 ± 0.11	-0.16 ± 0.09	-0.02 ± 0.14	0.20 ± 0.10	-0.02 ± 0.16	0.11 ± 0.06	0.01 ± 0.12
N9C04.3	–	–	0.15 ± 0.11	-0.06 ± 0.09	0.10 ± 0.15	0.22 ± 0.10	0.15 ± 0.17	0.04 ± 0.06	-0.07 ± 0.13
N9C04.4	–	–	0.09 ± 0.11	-0.12 ± 0.09	0.04 ± 0.14	0.23 ± 0.10	0.07 ± 0.16	0.08 ± 0.06	-0.03 ± 0.12
N9C04.5	–	–	0.01 ± 0.11	-0.08 ± 0.09	0.01 ± 0.14	0.13 ± 0.09	0.02 ± 0.16	0.05 ± 0.06	-0.01 ± 0.12
N9C05.1	–	–	-0.01 ± 0.09	-0.15 ± 0.09	-0.02 ± 0.13	0.18 ± 0.09	-0.02 ± 0.15	0.10 ± 0.06	0.01 ± 0.11
N9C05.2	–	–	0.10 ± 0.10	-0.16 ± 0.09	0.07 ± 0.13	0.33 ± 0.09	0.11 ± 0.15	0.11 ± 0.06	-0.05 ± 0.11
N9C05.3	–	–	-0.08 ± 0.10	-0.24 ± 0.09	-0.07 ± 0.13	0.25 ± 0.09	-0.09 ± 0.15	0.16 ± 0.06	0.04 ± 0.12
N9C05.4	–	–	0.05 ± 0.10	-0.12 ± 0.08	0.01 ± 0.13	0.19 ± 0.09	0.02 ± 0.15	0.08 ± 0.06	-0.01 ± 0.11
N9C05.5	–	–	0.03 ± 0.09	-0.21 ± 0.08	0.01 ± 0.13	0.31 ± 0.09	0.02 ± 0.15	0.14 ± 0.06	-0.01 ± 0.12
N	2	2	25	25	25	25	25	25	25
Mean	0	748	0.04	-0.14	0.01	0.22	0.02	0.09	-0.01
2 s.d.	–	–	0.12	0.10	0.09	0.15	0.13	0.06	0.06
95% CI	–	–	0.02	0.02	0.02	0.03	0.03	0.01	0.01

Different numbers (01–05) denote separate digestions of ~0.3 g standard material that were processed through the full chemical separation procedure and analyzed with each set of samples. A single analysis consumed ~25 ng of W (run at ~30 ppb).

[a] Corrected for a small mass-independent effect on ^{183}W after Kruijer et al. (2012) (Section S1).

Table S3. Mo isotope data for the terrestrial rock standard BHVO-2.

ID	Mo [a] (ng/g)	ε^{92}Mo (± 2 s.e.)	ε^{94}Mo (± 2 s.e.)	ε^{95}Mo (± 2 s.e.)	ε^{97}Mo (± 2 s.e.)	ε^{100}Mo (± 2 s.e.)
BHV13.1	–	0.34 ± 0.19	0.19 ± 0.14	0.16 ± 0.11	0.11 ± 0.08	-0.20 ± 0.11
BHV13.2	–	-0.15 ± 0.18	-0.03 ± 0.12	0.10 ± 0.09	-0.01 ± 0.06	-0.15 ± 0.11
BHV13.3	–	-0.16 ± 0.16	0.07 ± 0.12	-0.03 ± 0.07	-0.04 ± 0.06	-0.02 ± 0.10
BHV13.4	–	-0.18 ± 0.15	0.09 ± 0.11	-0.02 ± 0.08	0.02 ± 0.07	-0.05 ± 0.10
BHV13.5	–	0.24 ± 0.22	0.13 ± 0.16	0.10 ± 0.11	0.17 ± 0.08	0.08 ± 0.13
BHV13.7	–	0.19 ± 0.21	0.04 ± 0.14	0.13 ± 0.10	0.09 ± 0.08	-0.14 ± 0.14
BHV13.8	–	-0.17 ± 0.22	-0.05 ± 0.14	0.00 ± 0.11	-0.12 ± 0.09	-0.06 ± 0.14
BHV13.9	–	0.24 ± 0.23	0.21 ± 0.17	0.08 ± 0.13	-0.04 ± 0.11	-0.08 ± 0.14
BHV14	3746	–	–	–	–	–
BHV15	4223	–	–	–	–	–
BHV16.1	3734	-0.02 ± 0.23	-0.14 ± 0.16	0.02 ± 0.11	0.03 ± 0.08	0.01 ± 0.12
BHV16.2	–	-0.02 ± 0.25	0.14 ± 0.17	-0.05 ± 0.12	-0.11 ± 0.09	-0.12 ± 0.17
BHV16.3	–	0.17 ± 0.24	0.08 ± 0.16	0.11 ± 0.11	0.06 ± 0.08	-0.13 ± 0.14
BHV16.4	–	-0.14 ± 0.22	-0.06 ± 0.16	-0.12 ± 0.11	0.11 ± 0.10	0.10 ± 0.14
BHV16.5	–	0.20 ± 0.18	0.06 ± 0.13	0.22 ± 0.10	-0.10 ± 0.07	-0.13 ± 0.13
BHV16.6	–	-0.16 ± 0.23	-0.18 ± 0.16	0.02 ± 0.12	0.05 ± 0.09	-0.02 ± 0.15
BHV16.7	–	-0.09 ± 0.21	-0.09 ± 0.14	0.04 ± 0.11	-0.06 ± 0.08	-0.08 ± 0.13
BHV16.8	–	-0.20 ± 0.24	0.09 ± 0.18	0.02 ± 0.12	-0.05 ± 0.09	-0.02 ± 0.14
BHV18	3442	–	–	–	–	–
BHV19.1	3443	0.10 ± 0.19	0.06 ± 0.14	0.04 ± 0.09	-0.11 ± 0.07	-0.35 ± 0.12
BHV19.2	–	0.23 ± 0.21	0.19 ± 0.13	0.06 ± 0.12	-0.06 ± 0.10	-0.12 ± 0.12
BHV19.3	–	-0.37 ± 0.23	-0.21 ± 0.17	0.00 ± 0.11	-0.05 ± 0.09	0.21 ± 0.15
BHV19.4	–	-0.27 ± 0.23	-0.17 ± 0.16	-0.11 ± 0.12	0.03 ± 0.09	0.10 ± 0.14
BHV19.5	–	0.18 ± 0.22	0.12 ± 0.17	0.03 ± 0.10	0.10 ± 0.09	-0.11 ± 0.13
BHV19.6	–	0.12 ± 0.20	-0.02 ± 0.15	0.02 ± 0.10	0.06 ± 0.10	-0.17 ± 0.15
BHV19.8	–	-0.06 ± 0.26	0.02 ± 0.18	-0.02 ± 0.12	0.02 ± 0.10	0.16 ± 0.16
BHV19.9	–	0.00 ± 0.22	-0.13 ± 0.17	-0.03 ± 0.10	0.08 ± 0.09	-0.16 ± 0.13
BHV20	3295	–	–	–	–	–
N	6	24	24	24	24	24
Mean	3647	0.00	0.02	0.03	0.01	-0.06
2 s.d.	667	0.39	0.25	0.16	0.16	0.25
95% CI	350	0.08	0.05	0.03	0.03	0.05

Mo isotope ratios are normalized to ^{98}Mo/^{96}Mo = 1.453173. Different numbers (13–20) denote separate digestions of ~0.5 g standard material that were processed through the full chemical separation procedure and analyzed with each set of samples. A single analysis consumed ~80 ng of Mo (run at ~100 ppb).

[a] Mo concentrations as determined by quadrupole ICP-MS (Section S2).

Table S4. Mo isotope data for the terrestrial metal standard NIST 129c.

ID	Mo [a] (ng/g)	ε^{92}Mo (± 2 s.e.)	ε^{94}Mo (± 2 s.e.)	ε^{95}Mo (± 2 s.e.)	ε^{97}Mo (± 2 s.e.)	ε^{100}Mo (± 2 s.e.)
N9C02.1	7319	-0.20 ± 0.16	0.03 ± 0.12	0.03 ± 0.09	-0.08 ± 0.06	-0.38 ± 0.10
N9C02.2	–	-0.15 ± 0.21	-0.09 ± 0.12	0.08 ± 0.10	0.12 ± 0.08	-0.03 ± 0.12
N9C02.3	–	-0.18 ± 0.17	0.00 ± 0.12	0.02 ± 0.09	0.15 ± 0.07	-0.12 ± 0.11
N9C02.4	–	-0.40 ± 0.19	-0.03 ± 0.13	-0.07 ± 0.11	-0.01 ± 0.08	-0.04 ± 0.12
N9C02.6	–	-0.63 ± 0.21	-0.17 ± 0.15	-0.03 ± 0.11	0.01 ± 0.08	-0.30 ± 0.13
N9C02.7	–	-0.20 ± 0.20	0.01 ± 0.15	0.10 ± 0.11	0.05 ± 0.09	-0.23 ± 0.13
N9C02.8	–	-0.46 ± 0.19	-0.16 ± 0.14	-0.07 ± 0.11	-0.07 ± 0.09	-0.15 ± 0.13
N9C02.10	–	-0.23 ± 0.21	0.08 ± 0.14	0.03 ± 0.11	0.09 ± 0.08	-0.27 ± 0.14
N9C02.11	–	-0.38 ± 0.19	-0.05 ± 0.13	0.00 ± 0.09	0.10 ± 0.08	-0.22 ± 0.12
N9C02.12	–	0.15 ± 0.18	0.11 ± 0.14	0.19 ± 0.09	0.03 ± 0.07	-0.27 ± 0.10
N9C02.13	–	-0.61 ± 0.19	-0.32 ± 0.13	-0.05 ± 0.09	-0.06 ± 0.07	-0.16 ± 0.12
N9C02.14	–	-0.71 ± 0.19	-0.23 ± 0.13	-0.03 ± 0.09	0.06 ± 0.08	-0.25 ± 0.13
N9C02.15	–	-0.13 ± 0.24	-0.08 ± 0.15	-0.02 ± 0.11	-0.15 ± 0.10	-0.20 ± 0.14
N9C02.16	–	-0.44 ± 0.22	-0.15 ± 0.14	-0.13 ± 0.11	-0.02 ± 0.10	-0.01 ± 0.14
N9C03.1	7525	-0.16 ± 0.20	0.03 ± 0.16	0.12 ± 0.11	-0.03 ± 0.10	-0.01 ± 0.12
N9C03.2	–	-0.36 ± 0.20	-0.07 ± 0.15	0.05 ± 0.11	0.01 ± 0.07	-0.26 ± 0.14
N9C03.3	–	0.07 ± 0.21	0.02 ± 0.15	-0.01 ± 0.10	0.01 ± 0.07	-0.03 ± 0.13
N9C03.4	–	-0.11 ± 0.22	-0.06 ± 0.13	0.11 ± 0.10	0.03 ± 0.08	-0.29 ± 0.13
N9C03.5	–	-0.15 ± 0.20	-0.11 ± 0.12	0.02 ± 0.09	0.10 ± 0.08	-0.21 ± 0.12
N9C03.6	–	-0.35 ± 0.19	-0.12 ± 0.15	0.07 ± 0.09	0.11 ± 0.08	-0.12 ± 0.12
N9C03.7	–	-0.02 ± 0.23	-0.07 ± 0.17	0.06 ± 0.12	-0.03 ± 0.08	-0.13 ± 0.15
N9C03.9	–	-0.13 ± 0.18	0.11 ± 0.15	0.02 ± 0.10	0.01 ± 0.10	-0.32 ± 0.13
N9C03.10	–	-0.49 ± 0.19	-0.25 ± 0.15	-0.09 ± 0.11	-0.19 ± 0.09	-0.29 ± 0.12
N9C03.11	–	-0.25 ± 0.20	0.01 ± 0.15	-0.06 ± 0.10	0.07 ± 0.09	-0.13 ± 0.14
N9C03.12	–	-0.45 ± 0.20	-0.11 ± 0.12	-0.12 ± 0.09	0.06 ± 0.09	0.00 ± 0.13
N9C03.13	–	-0.28 ± 0.22	0.03 ± 0.14	-0.08 ± 0.12	0.16 ± 0.10	-0.17 ± 0.14
N9C03.15	–	-0.09 ± 0.23	0.05 ± 0.18	0.00 ± 0.10	0.07 ± 0.09	-0.18 ± 0.15
N9C04.1	7419	-0.60 ± 0.23	-0.26 ± 0.15	-0.16 ± 0.12	0.07 ± 0.09	0.03 ± 0.15
N9C04.2	–	-0.46 ± 0.21	-0.17 ± 0.14	-0.14 ± 0.12	0.14 ± 0.08	0.12 ± 0.13
N9C04.3	–	-0.56 ± 0.22	-0.30 ± 0.17	-0.08 ± 0.10	-0.01 ± 0.09	-0.01 ± 0.13
N9C04.4	–	-0.56 ± 0.20	-0.19 ± 0.13	-0.08 ± 0.11	0.07 ± 0.08	-0.15 ± 0.14
N9C04.5	–	-0.30 ± 0.22	-0.19 ± 0.14	0.08 ± 0.12	-0.05 ± 0.09	-0.33 ± 0.12
N9C04.6	–	-0.24 ± 0.20	-0.02 ± 0.14	0.00 ± 0.10	0.04 ± 0.08	-0.22 ± 0.15
N9C04.7	–	-0.13 ± 0.22	-0.01 ± 0.16	0.04 ± 0.13	0.03 ± 0.09	-0.20 ± 0.13
N9C04.8	–	-0.10 ± 0.24	-0.06 ± 0.17	0.06 ± 0.11	0.09 ± 0.08	-0.24 ± 0.15
N	3	35	35	35	35	35
Mean	7421	-0.29	-0.08	0.00	0.03	-0.16
2 s.d.	206	0.42	0.23	0.16	0.16	0.24
95% CI	256	0.07	0.04	0.03	0.03	0.04

Mo isotope ratios are normalized to ^{98}Mo/^{96}Mo = 1.453173. Different numbers (02–04) denote separate digestions of ~0.3 g standard material that were processed through the full chemical separation procedure and analyzed with each set of samples. A single analysis consumed ~80 ng of Mo (run at ~100 ppb).

[a] Mo concentrations as determined by quadrupole ICP-MS (Section S2).

References in Supplementary Material

Abreu, N.M., Bullock, E.S., 2013. Opaque assemblages in CR2 Graves Nunataks (GRA) 06100 as indicators of shock-driven hydrothermal alteration in the CR chondrite parent body. Meteorit. Planet. Sci. 48, 2406-2429.

Briani, G., Quirico, E., Gounelle, M., Paulhiac-Pison, M., Montagnac, G., Beck, P., Orthous-Daunay, F.R., Bonal, L., Jacquet, E., Kearsley, A., Russell, S.S., 2013. Short duration thermal metamorphism in CR chondrites. Geochim. Cosmochim. Acta 122, 267-279.

Budde, G., Kruijer, T.S., Fischer-Gödde, M., Kleine, T., 2015. Planetesimal differentiation revealed by the Hf–W systematics of ureilites. Earth Planet. Sci. Lett. 430, 316-325.

Budde, G., Burkhardt, C., Brennecka, G.A., Fischer-Gödde, M., Kruijer, T.S., Kleine, T., 2016a. Molybdenum isotopic evidence for the origin of chondrules and a distinct genetic heritage of carbonaceous and non-carbonaceous meteorites. Earth Planet. Sci. Lett. 454, 293-303.

Budde, G., Kleine, T., Kruijer, T.S., Burkhardt, C., Metzler, K., 2016b. Tungsten isotopic constraints on the age and origin of chondrules. Proc. Natl. Acad. Sci. USA 113, 2886-2891.

Burkhardt, C., Kleine, T., Oberli, F., Pack, A., Bourdon, B., Wieler, R., 2011. Molybdenum isotope anomalies in meteorites: Constraints on solar nebula evolution and origin of the Earth. Earth Planet. Sci. Lett. 312, 390-400.

Burkhardt, C., Hin, R.C., Kleine, T., Bourdon, B., 2014. Evidence for Mo isotope fractionation in the solar nebula and during planetary differentiation. Earth Planet. Sci. Lett. 391, 201-211.

Burkhardt, C., Schönbächler, M., 2015. Intrinsic W nucleosynthetic isotope variations in carbonaceous chondrites: Implications for W nucleosynthesis and nebular vs. parent body processing of presolar materials. Geochim. Cosmochim. Acta 165, 361-375.

Cook, D.L., Schönbächler, M., 2016. High-precision measurement of W isotopes in Fe–Ni alloy and the effects from the nuclear field shift. J. Anal. at. Spectrom. 31, 1400-1405.

Harju, E.R., Rubin, A.E., Ahn, I., Choi, B.G., Ziegler, K., Wasson, J.T., 2014. Progressive aqueous alteration of CR carbonaceous chondrites. Geochim. Cosmochim. Acta 139, 267-292.

Herzog, G.F., Caffee, M.W., 2014. Cosmic-Ray Exposure Ages of Meteorites, In: Holland, H.D., Turekian, K.K. (Eds.), Treatise on Geochemistry (Second Edition). Elsevier, Oxford, pp. 419-454.

Kleine, T., Münker, C., Mezger, K., Palme, H., 2002. Rapid accretion and early core formation on asteroids and the terrestrial planets from Hf–W chronometry. Nature 418, 952-955.

Kleine, T., Mezger, K., Münker, C., Palme, H., Bischoff, A., 2004. 182Hf-182W isotope systematics of chondrites, eucrites, and martian meteorites: Chronology of core formation and early mantle differentiation in Vesta and Mars. Geochim. Cosmochim. Acta 68, 2935-2946.

Kleine, T., Hans, U., Irving, A.J., Bourdon, B., 2012. Chronology of the angrite parent body and implications for core formation in protoplanets. Geochim. Cosmochim. Acta 84, 186-203.

Kong, P., Ebihara, M., Palme, H., 1999. Distribution of siderophile elements in CR chondrites: Evidence for evaporation and recondensation during chondrule formation. Geochim. Cosmochim. Acta 63, 2637-2652.

Kruijer, T.S., Sprung, P., Kleine, T., Leya, I., Burkhardt, C., Wieler, R., 2012. Hf–W chronometry of core formation in planetesimals inferred from weakly irradiated iron meteorites. Geochim. Cosmochim. Acta 99, 287-304.

Kruijer, T.S., Kleine, T., Fischer-Gödde, M., Burkhardt, C., Wieler, R., 2014a. Nucleosynthetic W isotope anomalies and the Hf–W chronometry of Ca–Al-rich inclusions. Earth Planet. Sci. Lett. 403, 317-327.

Kruijer, T.S., Touboul, M., Fischer-Gödde, M., Bermingham, K.R., Walker, R.J., Kleine, T., 2014b. Protracted core formation and rapid accretion of protoplanets. Science 344, 1150-1154.

Leitner, J., Vollmer, C., Hoppe, P., Zipfel, J., 2012. Characterization of presolar material in the CR chondrite Northwest Africa 852. Astrophys. J. 745, 38.

Leitner, J., Vollmer, C., Floss, C., Zipfel, J., Hoppe, P., 2016. Ancient stardust in fine-grained chondrule dust rims from carbonaceous chondrites. Earth Planet. Sci. Lett. 434, 117-128.

Schrader, D.L., Franchi, I.A., Connolly, H.C.,Jr., Greenwood, R.C., Lauretta, D.S., Gibson, J.M., 2011. The formation and alteration of the Renazzo-like carbonaceous chondrites I: Implications of bulk-oxygen isotopic composition. Geochim. Cosmochim. Acta 75, 308-325.

Shirai, N., Humayun, M., 2011. Mass independent bias in W isotopes in MC-ICP-MS instruments. J. Anal. at. Spectrom. 26, 1414-1420.

Willbold, M., Elliott, T., Moorbath, S., 2011. The tungsten isotopic composition of the Earth's mantle before the terminal bombardment. Nature 477, 195-198.